

**IMPROVED TARGET DETECTION THROUGH  
EXTENDED-DWELL, MULTICHANNEL RADAR**

A Dissertation  
Presented to  
The Academic Faculty

by

Audrey S. Paulus

In Partial Fulfillment  
of the Requirements for the Degree  
Doctor of Philosophy in the  
School of Electrical and Computer Engineering

Georgia Institute of Technology  
December 2014

**Copyright © Audrey S. Paulus 2014**

# **IMPROVED TARGET DETECTION THROUGH EXTENDED-DWELL, MULTICHANNEL RADAR**

Approved by:

Dr. Douglas B. Williams, Advisor  
School of ECE  
*Georgia Institute of Technology*

Dr. Mark A. Richards  
School of ECE  
*Georgia Institute of Technology*

Dr. Christopher F. Barnes  
School of ECE  
*Georgia Institute of Technology*

Dr. William L. Melvin, Advisor  
Georgia Tech Research Institute  
*Georgia Institute of Technology*

Dr. Aaron D. Lanterman  
School of ECE  
*Georgia Institute of Technology*

Dr. Laurence J. Jacobs  
School of CEE  
*Georgia Institute of Technology*

Date Approved: September 19, 2014

For my husband, Rick,  
and our children, Caroline, Rebecca, John, Anna, and David,  
whose encouragement and sacrifices have made this possible.

## ACKNOWLEDGEMENTS

I wish to thank my mother for always believing in me and for being an incredibly supportive and loving mother. My father, a WWII veteran, has been gone for over twenty years, but I still miss him every day. I am forever appreciative of his courage, patriotism, and independent spirit. My parents were both immigrants who worked tirelessly to provide opportunities for their three daughters. I greatly appreciate my sisters, Elizabeth and Jennifer, for being models of strength, diligence, and compassion for their little sister.

I am grateful for the unwavering support and love given to me by my husband, Rick, whose constant encouragement and personal sacrifices have made this possible. I wish to thank my five amazing children, Caroline, Rebecca, John, Anna, and David, for blessing my life and for inspiring me to be the best Mom I can be.

I want to thank the faculty and administration of the Electrical and Computer Engineering (ECE) Department at Georgia Tech for granting me readmission into the PhD program after a seventeen year absence. I would also like to express my gratitude to my PhD committee for taking the time to read my dissertation and critique my research.

I wish to express my appreciation to John Wilcher for his friendship; it was a true blessing having a good friend on this journey with me.

I want to thank my faculty advisor, Professor Doug Williams, and my research advisor, Dr. Bill Melvin, for sharing their passion for radar signal processing with me, for guiding my research, and for believing in me. I am especially grateful to Dr. Melvin and the Georgia Tech Research Institute for funding my graduate research work.

And lastly, I wish to thank God for a truly blessed life. If I had to do it all again, I wouldn't change a thing.

# TABLE OF CONTENTS

	Page
ACKNOWLEDGEMENTS	iv
LIST OF TABLES	viii
LIST OF FIGURES	ix
SUMMARY	xii
<u>CHAPTER</u>	
1 Introduction	1
2 Background	5
2.1 MTI Radar	5
2.2 Target Detection Theory	8
2.3 Receiver Operating Characteristic Curves	10
2.4 Maximizing SINR Output	11
2.5 Performance Metrics	14
2.5.1 SINR Loss	14
2.5.1.1 Clairvoyant SINR Loss	15
2.5.1.2 Adaptive SINR Loss	15
2.5.1.3 Reduced Dimension SINR Loss	16
2.5.1.4 Modeling Loss	16
2.5.2 Minimum Detectable Velocity	17
2.6 Target Motion Assumptions	18
2.6.1 Straight Line Assumption	18
2.6.2 Maximum Acceleration Assumption	18
3 Signal Models	20
3.1 Target Signal	20

3.1.1	Conventional Temporal and Spatial Signal Models	22
3.1.1.1	Linear-Phase Temporal Signal Model	22
3.1.1.2	Fixed-Angle Spatial Signal Model	23
3.1.1.3	Target Steering Vector	24
3.1.2	True Temporal and Spatial Signals	25
3.1.2.1	True Temporal Phase	25
3.1.2.2	True Spatial Phase	27
3.2	SINR Loss from Target Signal Approximations	28
3.2.1	Linear-Phase Modeling Loss	28
3.2.2	Loss as a Function of Target Motion	31
3.2.3	Spatial Phase Decorrelation	32
3.3	Clutter Model	36
3.4	Noise Model	41
3.5	Target Doppler Spread	41
4	A Multistage Algorithm for Single-Channel Extended Dwell Target Detection	44
4.1	Nonlinear Phase Analysis	45
4.2	Multistage, Dictionary-Based Matching Algorithm	47
4.2.1	Algorithm Development	47
4.2.2	SNR Limitations	53
4.2.3	Algorithm Limitations in the Presence of Clutter	53
4.2.4	Clutter Mitigation	54
4.3	Performance Characterization	55
4.3.1	Noise-Limited Environment, 500 ms Dwell Time	55
4.3.2	Clutter-Limited Environment	56
4.3.3	Noise-Limited Environment, Dwell Times Exceeding 500 ms	59

4.4 Error Analysis and Modeling Losses	60
4.5 Summary	63
5 Multichannel Algorithm for Extended-Dwell Target Detection	65
5.1 Pre-Doppler Stage	66
5.1.1 Clutter Mitigation and Spatial Integration	66
5.1.2 Evaluation of Temporal Weighting Options	68
5.2 Temporal Processing Stage	73
5.2.1 Temporal Signal Analysis	73
5.2.2 Extended-Dwell Temporal Processing Algorithm	77
5.2.2.1 Detection Decision	79
5.2.2.2 Flow Diagram	83
5.3 Performance Characterization	84
5.3.1 EDTP Algorithm, Endo-Clutter Targets	85
5.3.2 Extended-Dwell Limited Search (EDLS) Algorithm, Endo-Clutter Targets	87
5.3.3 Comparison of EDTP and EDLS Algorithms, Endo-Clutter Targets	88
5.3.4 EDTP Algorithm, Exo-Clutter Targets	88
5.4 Doppler Processing Comparison	91
5.5 Summary	92
6 Conclusions and Future Work	94
6.1 Conclusions	94
6.2 Future Work	97
APPENDIX A: Calculation of Linear Prediction Weights	100
REFERENCES	103
VITA	109

## LIST OF TABLES

	Page
Table 3.1: Nonlinear phase expressions.	26
Table 3.2: Radar and target parameters for phase analysis.	29
Table 3.3: Instantaneous frequency of nonlinear phase components.	41
Table 3.4: Maximum Doppler spread for dwell times of one and two seconds.	42
Table 4.1: Radar and target parameters for algorithm development.	46
Table 4.2: Typical dwell times at which nonlinear phase effects appear (target parameter dependent).	47
Table 4.3: General case: dominant dwell intervals and corresponding number of samples in each interval.	48
Table 4.4: Typical case: dominant dwell intervals and corresponding number of samples in each interval.	48
Table 4.5: Typical maximum shift from true signal due to phase contribution from next higher phase component.	52
Table 4.6: Percent of correctly chosen linear-phase waveforms in 1000 trials for various SNRs.	53
Table 4.7: Minimum detectable initial radial velocity for various target types in strong clutter.	57
Table 4.8: Dictionary limits and resolutions.	63
Table 5.1: Radar and target parameters for multichannel algorithm.	69
Table 5.2: Original dominant frequencies and algorithm-corrected target Dopplers.	79



## LIST OF FIGURES

	Page
Figure 2.1: Radar data cube.	7
Figure 2.2: Receiver operating characteristic (ROC) curves.	10
Figure 3.1: Geometry of platform and ground target at elevation angle, $\theta$ , and azimuth angle, $\phi$ .	23
Figure 3.2: Array geometry.	24
Figure 3.3: Slow-time phase: (a) actual and (b) without linear component.	29
Figure 3.4: SNR as a function of dwell time for the clairvoyant model and the linear-phase model.	30
Figure 3.5: SNR loss as a function of (a) tangential velocity and (b) radial acceleration.	31
Figure 3.6: Phases shown on unit circle (left to right) for $M = 3$ , $M = 4$ , and $M = 5$ that completely decorrelate the spatial signal.	34
Figure 3.7: Top view of radar geometry showing extent of angle at beginning and end of dwell that causes decorrelation with fixed-angle signal model.	35
Figure 3.8: Angle-Doppler clutter structure.	39
Figure 3.9: Spread of target signal energy into clutter region.	43
Figure 4.1: Output SNR for linear-phase model, linear-plus-second-order-phase model, and clairvoyant model.	45
Figure 4.2: Doppler showing true linear phase component of target signal and Doppler of target signal when quadratic-phase contribution is included over a 100 ms dwell.	49
Figure 4.3: Flow diagram of multistage algorithm.	51
Figure 4.4: Output SNR for the clairvoyant signal model, the multistage algorithm model, and the linear-phase model as a function of pulse number over a 500 ms dwell.	55
Figure 4.5: Output SINR loss in relation to optimal SNR as a function of initial radial velocity for a single-sample SNR of $-8$ dB, a single-sample SCR of $-20$ dB, and dwells of (a) 500 ms and (b) 1.0 s.	56

Figure 4.6: Output SINR for the clairvoyant signal model, the multistage algorithm model, and the linear-phase model as a function of pulse number for an exo-clutter target with single-sample SCR of $-20$ dB.	58
Figure 4.7: Output SNR for dwell times up to four seconds for the multistage algorithm model and the clairvoyant model.	59
Figure 5.1: Pre-Doppler STAP concept.	67
Figure 5.2: Three combined channels of clutter, noise, and signal power input to pre-Doppler processing.	70
Figure 5.3: Frequency responses of normalized binomial weights for lengths of 3, 5, 7, and 9.	71
Figure 5.4: Frequency responses of three-sample linear prediction weight vector and three-sample binomial weight vector.	71
Figure 5.5: Twenty averaged pre-Doppler SINR outputs for binomial and linear prediction temporal weights of length three and a target radial velocity of $1.5$ m/s.	72
Figure 5.6: Doppler spread of target signal with maximum parameters over a one-second dwell.	74
Figure 5.7: Overlaid frequency spectrums of the ten $100$ ms sub-CPIs for maximum target parameters.	76
Figure 5.8: Pdfs for $p_{x H_0}(x H_0)$ and $p_{x H_1}(x H_1)$ for detection decision based on output magnitude for a pre-processing single-sample SNR of $-6$ dB.	80
Figure 5.9: Examples with line proximity for detection decision for (a) $H_1$ and (b) $H_0$ hypotheses.	81
Figure 5.10: Pdfs for $p_{x H_0}(x H_0)$ and $p_{x H_1}(x H_1)$ for detection decision based on line proximity for pre-processing single-sample SNRs of (a) $-6$ dB and (b) $-12$ dB.	82
Figure 5.11: EDTP algorithm flow diagram.	84
Figure 5.12: ROC curves for the EDTP algorithm showing $P_D$ as a function of initial radial velocity for an accelerating target with various single-sample SNRs.	86
Figure 5.13: ROC curves for the EDLS algorithm showing $P_D$ as a function of initial radial velocity for an accelerating target with various pre-processing single-sample SNRs.	87

Figure 5.14: ROC curves for EDLS and EDTP algorithms showing  $P_D$  as a function of initial radial velocity for an accelerating target with single-sample SNRs of  $-6$  dB and  $-8$  dB. 88

Figure 5.15: Pdf of  $p_{x|H_0}(x|H_0)$  used to establish line proximity for  $P_{FAS}$  of 0.001 and 0.01. 89

Figure 5.16: ROC curves for the EDTP algorithm for an exo-clutter target showing  $P_D$  as a function of single-sample input SNR for  $P_{FAS}$  of 0.001 and 0.01. 90

## SUMMARY

Target detection is one of the primary applications of airborne radar. Improving the detection of weak, ground-moving targets that are masked by both receiver noise and ground clutter requires signal processing methods that boost the target signal energy above the noise and suppress the interference. Current radar systems often operate on small platforms that are power and aperture size limited; thus an increase in signal energy must come through processing techniques that combine target echoes from multiple transmitted pulses rather than from increasing transmitted power or aperture size. The number of target samples necessary for detection depends on the signal-to-noise ratio (SNR) of a single pulse return. Very weak targets require coherent integration of many target samples for the SNR to reach reliable detection levels. For a given pulse transmission rate, or pulse repetition frequency (PRF), this required increase in integrated target samples corresponds to an increase in the data collection time, known as the coherent processing interval (CPI) or dwell time.

Conventional ground moving target indication (GMTI) radar approximates unknown target motion with a single dominant component, radial velocity, and assumes a fixed angle between the platform and the target over the CPI. Over a sufficiently short dwell time, these assumptions allow the signal to be modeled with a linear phase for Fourier-based processing methods to efficiently yield accurate target information. As dwell time increases, nonlinear phase components in the slow-time signal and the change in angle between the platform and the target create phase mismatches between the true target signal and the slow-time and spatial models. These phase mismatches between the conventional

model and the true target signal limit coherent integration of signal energy and reduce output SNR as dwell time is extended.

Increasing the time over which target samples are coherently integrated requires signal processing methods that account for the multiple nonlinear phase components of the extended dwell temporal signal. Consideration of the change in angle between the platform and the target over an extended dwell is also essential. Single-channel and multichannel algorithms are presented that integrate temporal and spatial signal energy collected over an extended dwell time and mitigate clutter to improve detection of weak targets.

The single-channel algorithm provides an estimate of the optimal detector that maximizes output SINR for the extended dwell time signal. Rather than searching for the optimal detector in an intractably large filter bank that contains all combinations of phase components, the single-channel algorithm projects dictionary entries against the data to estimate the signal's linear and nonlinear phase components sequentially with small, phase-specific dictionaries in a multistage process. When used as the detector, the signal model formed from the estimated phase components yields near optimal performance for a wide range of target parameters for dwell times up to four seconds. In comparison, conventional radar processing methods are limited to a coherent integration time of approximately 100 milliseconds (ms) for typical radar and target parameters. Output SINR over a 500 ms dwell is generally adequate for detection of weak targets. Output SINR for dwell times exceeding 500 ms may be sufficient for other radar applications such as tracking, identification, and imaging.

The multichannel solution is based on element-space pre-Doppler space-time-adaptive processing (STAP) with a modification of the final temporal processing stage

from Doppler processing to a temporal processing algorithm suitable for the extended-dwell-time signal. The extended-dwell temporal processing algorithm used in conjunction with pre-Doppler clutter mitigation detects lower radial velocity targets than the single-channel, multistage algorithm presented herein and also detects weak, low radial velocity targets better than conventional methods. For a target with a single-sample SNR of  $-6$  dB and an initial radial velocity of  $1.0$  m/s in a strong clutter environment, the probability of detection ( $P_D$ ) with the extended-dwell temporal processing algorithm is approximately  $0.8$  for a probability of false alarm ( $P_{FA}$ ) of  $0.001$ .

The extended-dwell temporal processing algorithm applied to the pre-Doppler temporal output signal significantly outperforms Doppler processing in detecting targets with low single-sample SNR, especially at low radial velocities. For typical GMTI radar parameters and for a target with an initial radial velocity of  $1.6$  m/s, a single-sample SNR of approximately  $5$  dB is required for Doppler processing to achieve the same  $P_D$  as the extended-dwell temporal processing achieves for a single-sample SNR of  $-6$  dB in  $500$  trials with a  $P_{FA}$  of  $0.001$ . This decrease of  $11$  dB in required single-sample SNR for equivalent detection almost doubles the range at which a weak, slow-moving target can be detected. This increased range of detection allows for a more stealthy system and lowers the risk of electronic attack.

# **CHAPTER 1**

## **INTRODUCTION**

Detection of ground moving targets is a primary function of airborne radar. Improving the detection of weak targets requires an increase in the signal-to-interference-plus-noise ratio (SINR) achieved by suppressing interference from stationary ground clutter and by increasing the signal-to-noise ratio (SNR). Boosting SNR by increasing power or antenna size is not an option for many of today's radar systems that have limited power and small aperture requirements and are often used on unmanned aerial vehicles (UAVs) [1, 2]. Instead, increases in SNR must come from extending the time interval over which target samples are coherently integrated.

Conventional multichannel radar typically utilizes space-time adaptive processing (STAP) [3–6] methods to determine target location and radial velocity from the received spatial and temporal data. STAP assumes a linear-phase temporal signal model and a fixed angle between the target and the platform over the dwell. These assumptions are valid over a sufficiently short dwell time for which Fourier-based processing of the space-time signal yields accurate target information. As dwell time increases, nonlinear phase components in the target signal create a temporal phase mismatch between the conventional model and the true target signal that causes destructive interference and reduces output SINR. In addition, the angle between the platform and the target changes over an extended dwell as the platform moves past the area of interest on the ground. This change in angle creates a spatial phase mismatch with the conventional fixed-angle model that also reduces output SINR over long dwells. The short-dwell requirement for Fourier-based processing methods

limits the number of target samples that can be coherently combined to increase output SINR. Detection of weak targets that are masked by clutter and noise requires integration of target samples collected over a longer dwell time, which necessitates an alternative to conventional signal processing methods.

Prior research in moving target detection over a long dwell, or coherent processing interval (CPI), assumes either single-channel data or a preprocessing step that collapses the multichannel data to a single temporal signal suitable for single-channel processing. These single-channel methods include parameter estimation techniques that approximate the unknown target parameters of the extended-dwell, slow-time signal [7–10] or focusing methods that concentrate smeared signal energy in a synthetic aperture radar (SAR) image [11, 12]. The parameter estimation techniques yield both linear and quadratic phase information, which improves the signal model over the conventional linear-phase model. However, these methods, which include the Wigner-Ville transform [13, 14] and the chirp transform [15, 16], rely on signal energy to exceed noise levels for accurate parameter estimation. In addition, the ideal, extended-dwell signal model generally requires higher order phase components than are provided through parameter estimation. The techniques described by Fienup in [11] and Perry, Dipietro, and Fante in [12] focus smeared target signal energy in a SAR image caused by a moving target with unknown motion parameters. These processing methods require single-sample signal power to be roughly equal to or greater than the noise power and are not effective at focusing weak target signals whose single-sample power is considerably below the noise power; Fienup discusses the "blurred image of the moving target" and describes techniques to cancel the effects of unknown phase components in an image "as long as the target-to-background-energy is large." Perry,



Dipietro, and Fante develop and apply the Keystone transform to focus signal energy that spreads into multiple range bins. Although focusing of signal energy spread across multiple range bins is of interest in SAR imaging and in mitigating range migration, the Keystone transform does not address the spread of signal energy across multiple frequency bins which is a more typical detection challenge over a long CPI.

Other research considers the benefits of long dwell to enhance clutter mitigation [17–19] but does not directly address development of an improved extended-dwell signal model. In these cases, target parameters are assumed to be limited to a single radial velocity component for which the linear-phase model is sufficient, or target parameter information is determined through previously discussed methods such as parameter estimation.

In contrast, the research presented in this dissertation improves detection of weak targets whose low signal energy and multiple temporal phase components make traditional parameter estimation techniques ineffective and whose single-sample SNR is below what is required for traditional SAR focusing methods. Targets of interest are not detectable on a sub-CPI basis.

Two approaches in developing algorithms that improve detection of weak targets from a small radar platform are presented in this dissertation. In the first approach, analysis of the temporal signal’s linear and nonlinear phase components forms the basis for an algorithm that generates an accurate multiphase signal model over an extended dwell time. The signal model is developed in a multistage process that uses inner products to identify the best-matched signal components from phase-specific dictionaries. The second approach to the detection challenge employs multiple spatial channels to improve clutter mitigation and provide essential target location information. This approach mitigates

clutter and integrates spatial samples based on pre-Doppler STAP methods [3, 4] and then integrates temporal samples with an algorithm that sub-divides the temporal signal into smaller sub-CPIs for Fourier-based processing. The multichannel solution is unique in addressing both the spatial and temporal challenges presented in the extended dwell time signal and in providing a complete signal processing solution beginning with the received multichannel data and ending with the detection decision.

All analysis uses MATLAB-generated data. A broadside collection geometry is assumed, though concepts presented in this dissertation can be applied to various data collection scenarios. The range resolution confines signal energy to a single range cell in most cases; for dwells in which target movement exceeds range resolution, efforts must be made to mitigate range migration.

## **CHAPTER 2**

### **BACKGROUND**

Radar is an electromagnetic sensing system used to gather information about an object or a scene by transmitting energy toward the area of interest and measuring the magnitude and phase of the reflected energy. Objects of interest include aircraft, ships, automobiles, military vehicles, landforms, weather systems, and people. Primary applications of radar include detection, imaging, tracking, and identification. Moving target indication (MTI) radar [20] is used to detect the presence of moving targets in the air and on the ground.

#### **2.1 MTI Radar**

Single-channel MTI methods such as pulse Doppler radar [21] are typically used to detect fast-moving targets. Detection of slower moving ground targets requires multiple antenna channels mounted on an aircraft to provide more precise clutter mitigation based on the angle-Doppler characteristics of stationary ground clutter. Conventional multichannel, ground moving target indication (GMTI) radar provides information on the azimuth location of a target as well as its range and radial velocity.

GMTI radar transmits electromagnetic energy from an airborne platform toward an area of interest on the ground through a series of pulses at a rate called the pulse repetition frequency (PRF). The time between pulses is the pulse repetition interval (PRI), which is equal to  $1/\text{PRF}$ . The duration of the CPI is equal to the total number of transmitted pulses multiplied by the PRI. Each transmitted pulse is a waveform given by

$$p(t) = a_t \exp(j(2\pi f_c t + \psi + \theta(t))), \quad (2.1)$$

where  $f_c$  is the carrier frequency,  $a_t$  is the signal amplitude,  $\psi$  is an initial phase, and  $\theta(t)$  is the phase or frequency modulation of the carrier. Typical carrier frequencies for detection are in the X-band of radio frequencies between 8 and 12 GHz. Radar frequencies in this band provide an ideal combination of high antenna gain, narrow beamwidth, and minimal atmospheric loss at distances typical of GMTI radar [22, 23]. A common carrier modulation is the linear frequency modulated (LFM) signal [24],

$$\exp(j\theta_{\text{LFM}}(t)) = \exp(j\pi \frac{\beta}{\tau} t^2), \quad (2.2)$$

whose instantaneous frequency changes linearly by the signal bandwidth,  $\beta$ , over the duration,  $\tau$ , of the transmitted pulse. The carrier frequency is also referred to as the center frequency for an LFM signal.

Range resolution is the ability of a radar to distinguish between targets that are close in range. When measured as the minimum distance in range between separable targets, range resolution is inversely proportional to the transmitted waveform bandwidth. MTI radar typically uses narrowband waveforms to minimize range migration, the spread of signal energy from a single target into multiple range bins as the target moves during the CPI. The received signal from each transmitted pulse includes reflections from all objects on the ground illuminated by the antenna. The reflected signal is sampled at a rate,  $F_s$ , greater than or equal to the bandwidth of the waveform; the received signal is sorted into range cells with spacing  $\Delta r = c/2F_s$  [25].

Airborne GMTI radar systems receive and process reflected signals from all of the stationary clutter and moving targets in a ground scene as the aircraft moves past the scene of interest. The received signal energy consists of fast-time data, the single-pulse return

from each range cell illuminated by the antenna; slow-time data, the received signal from successive pulses; and spatial data, the received signal at each of the channels. It can be helpful to visualize the received fast-time, slow-time, and spatial data collected over a single CPI in a data cube [26, 27] as shown in Figure 2.1.

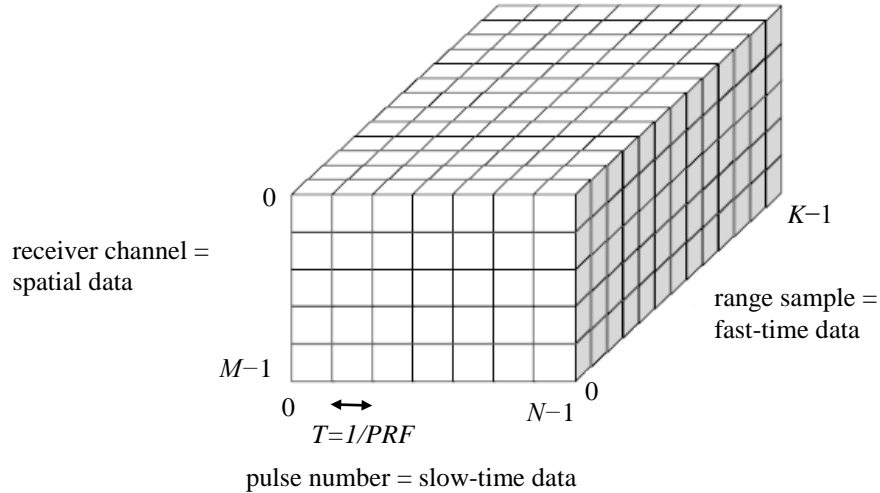


Figure 2.1. Radar data cube.

To test for the presence of a target at a particular range, single-channel methods process the slow-time data, while multichannel methods operate on both the spatial and the slow-time data. The change in the slow-time phase over the CPI provides information on target motion parameters, while the change in spatial phase across the array provides information about the azimuth position of the target. Optimal processing gains are achieved by utilizing phase information to coherently integrate the slow-time and spatial signal energy collected over the entire CPI.

MTI radar often uses Fourier-based methods to coherently process the slow-time data and sort the frequency components of the data into Doppler bins. The width, or

resolution, of these bins in hertz is inversely proportional to the number of pulses in the CPI. The Doppler frequency attributed to an object depends on the radial velocity of the object in relation to the radar platform. The Doppler frequency associated with a stationary object on the ground can change during the CPI because of changes in relative radial velocity as the platform moves past the object. The Doppler frequency associated with a moving target can also change over time, primarily as a result of changes in target radial velocity over the CPI.

## 2.2 Target Detection Theory

Reflections from all objects in the path of the transmitted signal contribute to the data received by the radar system. GMTI radar receives unwanted reflections from ground clutter in addition to possible echoes from a moving target. The reflections from clutter, considered interference, and thermal receiver noise affect the accuracy of the decision between two possible scenarios: target presence or target absence. Target presence, considered the  $H_1$  hypothesis, indicates a target is present in addition to noise and interference; target absence, considered the  $H_0$  hypothesis, indicates only noise and interference are present in the received signal [28, 29]:

1.  $H_0$ :  $x = \text{noise} + \text{interference}$
2.  $H_1$ :  $x = \text{target} + \text{noise} + \text{interference}$

The probability of detection,  $P_D$ , is the probability that  $H_1$  is chosen when a target is present. The probability of false alarm,  $P_{FA}$ , is the probability that  $H_1$  is chosen when a target is not present. The received data is processed with the goal of achieving the most accurate decision possible.

Detection decisions are based on a measured value called the “observation”. The set of observations for which the  $H_0$  hypothesis is chosen is denoted the decision region  $\mathcal{R}_0$ , while the set of observations for which the  $H_1$  hypothesis is chosen is denoted the decision region  $\mathcal{R}_1$ . The most accurate decision requires maximum separation of  $\mathcal{R}_0$  and  $\mathcal{R}_1$ . The regions are chosen according to Bayes decision criteria [30, 31], which minimizes the cost associated with an incorrect decision. Because the observed data is statistical in nature, the decision rule based on the minimization of the Bayes cost function depends on two conditional probability density functions (pdfs) of the observed data  $x$ : (1)  $p_{x|H_0}(x|H_0)$ , the pdf of  $x$  given that  $H_0$  is true and (2)  $p_{x|H_1}(x|H_1)$ , the pdf of  $x$  given that  $H_1$  is true. Minimizing the Bayes cost function leads to the decision rule known as the likelihood ratio test (LRT) [32], which can be written

$$\frac{p_{x|H_1}(x|H_1)}{p_{x|H_0}(x|H_0)} \underset{H_0}{\overset{H_1}{>}} \eta, \quad (2.3)$$

for a threshold  $\eta$ . The simplest scalar quantity essential to hypothesis testing that best represents the data is known as the sufficient statistic. The sufficient statistic can be a measured processing output or the result of any positive monotonic operation on that output.

A typical approach to hypothesis testing is the Neyman-Pearson criteria [28, 33], which seeks to optimize  $P_D$  for a given  $P_{FA}$ . The threshold for the detection decision is set based on the desired  $P_{FA}$ . Formulas for computing thresholds exist for signals with known pdfs. In some instances, the sufficient statistic under  $H_0$  has an unknown pdf and the threshold must be established for a particular  $P_{FA}$  through a Monte Carlo approach. The  $P_D$

in the case of unknown pdfs is based on the percentage of outcomes under hypothesis  $H_1$  in which the sufficient statistic exceeds the established threshold.

### 2.3 Receiver Operating Characteristic Curves

Receiver operating characteristic (ROC) curves display  $P_D$  as a function of  $P_{FA}$ , often for multiple output SNRs. Figure 2.2 shows an example of ROC curves.

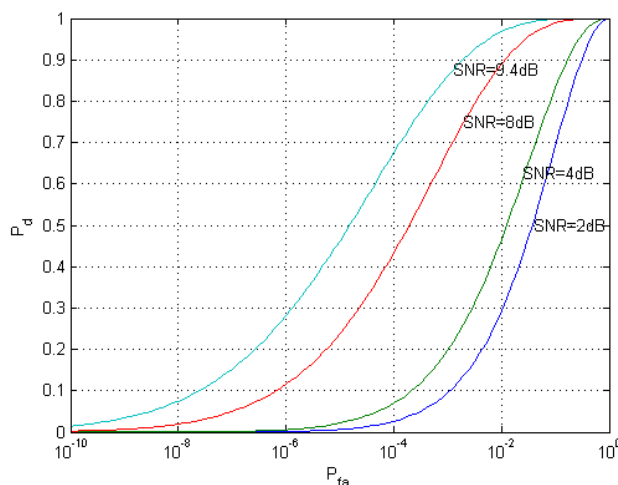


Figure 2.2. Receiver operating characteristic (ROC) curves ([34], © mathworks.com).

As shown in Figure 2.2, detection is challenging for any SNR as the  $P_{FA}$  approaches zero. Similarly, detection is likely for a wide range of SNRs as the  $P_{FA}$  approaches one. In the region between these two extremes, the  $P_{FA}$  has a greater effect on  $P_D$  for a given SNR, and the SNR has a greater effect on  $P_D$  for a given  $P_{FA}$ . The steep slope of the  $P_D$  versus  $P_{FA}$  curve for each SNR in this middle region means that for a given SNR, a small increase in  $P_{FA}$  causes a large increase in  $P_D$ . In this same region, for a given  $P_{FA}$ , a small increase in SNR causes a significant increase in  $P_D$ . In general, for a given  $P_{FA}$ , an increase in output SNR corresponds to an increase in  $P_D$  [35]. Thus, the detection of weak targets can be improved through an increase in output SNR.



## 2.4 Maximizing Output SINR

Detection decisions are made after the received data are processed. Prior to processing, the received data form an  $M$  by  $N$  matrix,  $\mathbf{X}_k$ , that represents the spatial and slow-time slice of the data cube at the  $k^{th}$  range [3]:

$$\mathbf{X}_k = \begin{bmatrix} x_{k,0,0} & x_{k,0,1} & x_{k,0,2} & \cdots & x_{k,0,N-1} \\ x_{k,1,0} & x_{k,1,1} & x_{k,1,2} & \cdots & x_{k,1,N-1} \\ \vdots & \vdots & \vdots & & \vdots \\ x_{k,M-1,0} & x_{k,M-1,1} & x_{k,M-1,2} & \cdots & x_{k,M-1,N-1} \end{bmatrix}, \quad (2.4)$$

where  $M$  is the number of spatial channels or elements and  $N$  is the number of pulses in the CPI. Stacking the columns of data, with the first entry of each column following the last entry of the previous column, yields the space-time snapshot for the  $k^{th}$  range,  $\mathbf{x}_k$ , a vector of length  $MN$  consisting of an interference-plus-noise signal,  $\mathbf{x}_{I/k}$ , and a possible target signal,  $\mathbf{s}_k$ :

$$\mathbf{x}_k = \mathbf{x}_{I/k} + \mathbf{s}_k. \quad (2.5)$$

The goal in processing the received data is to apply weighting to the space-time snapshot to maximize the output SINR. The optimal weight vector or processor maximizes the signal gain while minimizing the interference. The output of the space-time processor is a scalar,  $z$ , determined through an inner-product operation that weights and sums the channel and slow-time data:

$$z_k = \mathbf{w}_k^H \mathbf{x}_k, \quad (2.6)$$

where  $\mathbf{w}_k$  is the space-time processor or weight vector. A function of the output is compared to a threshold to determine if a target is present. Substituting (2.5) into (2.6) and dropping the subscript  $k$  for simplicity yields

$$z = \mathbf{w}^H \mathbf{x}_I + \mathbf{w}^H \mathbf{s} = z_I + z_s, \quad (2.7)$$

where  $z_I$  is the interference-plus-noise component and  $z_s$  is the target signal component of the output [3, 4]. The output SINR is given as

$$SINR = \frac{E[|z_s|^2]}{E[|z_I|^2]} = \frac{E[\mathbf{w}^H \mathbf{s} \mathbf{s}^H \mathbf{w}]}{E[\mathbf{w}^H \mathbf{x}_I \mathbf{x}_I^H \mathbf{w}]} = \frac{|\mathbf{w}^H \mathbf{s}|^2}{\mathbf{w}^H \mathbf{R}_I \mathbf{w}}, \quad (2.8)$$

where  $E[\cdot]$  represents expectation [38] and  $\mathbf{R}_I$ , the  $MN \times MN$  interference covariance matrix, is equal to  $E[\mathbf{x}_I \mathbf{x}_I^H]$ .

The optimal processor requires clairvoyance as maximum integration gain is achieved with an optimal weight vector that can only be determined when the target parameters and interference data statistics are known a priori. The optimal weight vector that maximizes the SINR for multichannel radar is

$$\mathbf{w}_{opt} = \kappa \mathbf{R}_I^{-1} \mathbf{s}, \quad (2.9)$$

for an arbitrary scalar  $\kappa$  that does not affect SINR [6]. Application of the optimal weight vector to the space-time snapshot yields optimal SINR [4]:

$$SINR_{opt} = \frac{|\mathbf{w}_{opt}^H \mathbf{s}|^2}{\mathbf{w}_{opt}^H \mathbf{R}_I \mathbf{w}_{opt}} = \mathbf{s}^H \mathbf{R}_I^{-1} \mathbf{s}. \quad (2.10)$$

In practice, the interference statistics are unknown and must be estimated from the data. Space-time adaptive processing (STAP) is the name given to the practical implementation of optimal space-time processing that adaptively estimates interference from multiple snapshots of the data that presumably contain no target.

The target signal vector  $\mathbf{s}$  from (2.5) can be written as the product of a magnitude and a phase factor,  $\mathbf{s}_\phi$ . The optimal weight vector is matched to  $\mathbf{s}_\phi$ ; thus, the expression for optimal SINR can be written

$$SINR_{opt} = \frac{\sigma_s^2 |\mathbf{w}_{opt}^H \mathbf{s}_\phi|^2}{\mathbf{w}_{opt}^H \mathbf{R}_I \mathbf{w}_{opt}} = \sigma_s^2 \mathbf{s}_\phi^H \mathbf{R}_I^{-1} \mathbf{s}_\phi, \quad (2.11)$$

where  $\sigma_s^2$  is the single-sample target signal power.

Though clutter degrades performance in comparison to the noise-limited case, it is instructive to examine the noise-limited case to evaluate factors that affect radar performance. In the noise-limited case,  $\mathbf{R}_I = \sigma_n^2 \mathbf{I}_{MN}$ , where  $\sigma_n^2$  is the noise power and  $\mathbf{I}_{MN}$  is the  $MN \times MN$  identity matrix, and the optimal weight vector is proportional to  $\mathbf{s}_\phi$ . Optimal processing coherently integrates  $MN$  target samples. In the noise-limited case, the expression for optimal SINR in (2.11) becomes an expression for optimal SNR:

$$SNR_{opt} = \frac{\sigma_s^2}{\sigma_n^2} MN. \quad (2.12)$$

Single-sample SNR is equal to the single-sample signal power,  $\sigma_s^2$ , divided by the noise power,  $\sigma_n^2$ :

$$SNR_{single} = \frac{\sigma_s^2}{\sigma_n^2}. \quad (2.13)$$

For a target at range  $r$  with radar cross section (RCS)  $\sigma_t$  [37],  $SNR_{single}$  is approximated as

$$SNR_{single}(\theta, \varphi) = \left( \frac{P_t G_t(\theta, \varphi) \sigma_t A_e / M}{(4\pi)^2 r^4 N_{in} F_n L_s} \right), \quad (2.14)$$

where  $P_t$  is the transmit power,  $G_t(\phi, \theta)$  is the antenna gain for direction  $(\phi, \theta)$ ,  $A_e$  is the effective aperture area of the  $M$ -channel array,  $N_{in}$  is the noise input power,  $F_n$  is the receiver noise figure, and  $L_s$  is the system loss [38]. Substituting (2.14) and (2.13) into (2.12) yields

$$SNR_{opt}(\theta, \phi) = \left( \frac{P_t G_t(\theta, \phi) \sigma_t A_e}{(4\pi)^2 r^4 N_{in} F_n L_s} \right) N. \quad (2.15)$$

Equation (2.15) represents optimal SNR for a given transmitted power, antenna size, and CPI length, which is achieved when all  $M$  spatial samples and all  $N$  temporal samples in the CPI are coherently integrated. SNR increases can come from increasing the power-aperture product,  $P_t A_e$ , or through temporal integration by increasing the number of target samples that are coherently combined. Increasing gains through coherent integration of additional target samples allows for operation on a small power-limited platform and prevents increases in received clutter power that would result from a larger power-aperture product.

## 2.5 Performance Metrics

### 2.5.1 SINR Loss

Improvements in detection require an increase in output SINR. An understanding of system performance can be gained by analyzing the effects of signal modeling and clutter mitigation on SINR loss.

Output SINR is upper bounded by optimal SNR, the clairvoyant case with noise-only interference. Output SINR can be expressed as the product of optimal SNR and various loss factors:

$$SINR = SINR_{opt} \prod_{i=1}^I L_i, \quad (2.16)$$

where  $L_i$  is the  $i^{th}$  SINR loss term and  $0 \leq L_i \leq 1$  [39]. Four loss factors are considered: (1) clairvoyant SINR loss,  $L_1$ ; (2) adaptive SINR loss,  $L_2$ ; (3) reduced-dimension SINR loss,  $L_3$ ; and (4) signal modeling SINR loss,  $L_4$ . Hence, the goal of maximizing output SINR becomes an objective to minimize losses from clutter mitigation techniques and signal modeling estimates.

#### 2.5.1.1 Clairvoyant SINR Loss

Optimal SINR is the clairvoyant case of known target and interference signals and is always less than or equal to optimal SNR, the clairvoyant case in the absence of interference. The ratio of optimal SINR to optimal SNR is known as clairvoyant SINR loss and is given as

$$L_1 = \frac{SINR_{opt}}{SNR_{opt}} = \mathbf{s}^H \mathbf{R}_I^{-1} \mathbf{s} / \left( \frac{\sigma_s^2}{\sigma_n^2} NM \right) = \frac{\sigma_n^2 \mathbf{s}^H \mathbf{R}_I^{-1} \mathbf{s}}{\sigma_s^2 NM}. \quad (2.17)$$

The interference assumed in this dissertation is from clutter only; thus  $L_1$  is the loss that results from including the known clutter signal in the data. Optimal SINR provides an upper bound for performance in a clutter-limited environment.

#### 2.5.1.2 Adaptive SINR Loss

Adaptive SINR loss is the ratio of output SINR for the filter,  $\hat{\mathbf{w}} = \hat{\mathbf{R}}_I \mathbf{s}$ , generated with estimated interference to optimal SINR, where interference is known a priori:

$$L_2 = \frac{SINR_{adapt}}{SINR_{opt}} = \frac{|\hat{\mathbf{w}}^H \mathbf{s}|^2}{(\hat{\mathbf{w}}^H \hat{\mathbf{R}}_I \hat{\mathbf{w}})(\mathbf{s}^H \mathbf{R}_I^{-1} \mathbf{s})}. \quad (2.18)$$

Practical clutter mitigation techniques require estimation of the interference from surrounding range bins that presumably contain no target. Since the data is simulated in this research and the interference is known, the clairvoyant covariance matrix is used for algorithm evaluation to provide an upper bound for SINR. This clairvoyant case offers insight into best-case algorithm performance, which must be acceptable for known interference before the more practical case of estimating interference from the data is considered. Because known interference statistics are used to mitigate clutter, the adaptive SINR loss factor,  $L_2$ , is equal to one.

#### 2.5.1.3 Reduced Dimension SINR Loss

Since the loss factor  $L_2$  is equal to one, the SINR loss associated with a reduced dimension clutter mitigation method as opposed to clutter mitigation with the full  $MN \times MN$  covariance matrix is the ratio of reduced dimension SINR to optimal SINR:

$$L_3 = \frac{SINR_{rd}}{SINR_{opt}} = \frac{|\mathbf{w}_{rd}^H \mathbf{s}|^2}{(\mathbf{w}_{rd}^H \mathbf{R}_{l,rd} \mathbf{w}_{rd})(\mathbf{s}^H \mathbf{R}_I^{-1} \mathbf{s})}. \quad (2.19)$$

#### 2.5.1.4 Modeling Loss

SINR loss results when a suboptimal signal model,  $\mathbf{s}_{sub}$ , used in the weight vector,  $\mathbf{w}_{sub} = \mathbf{R}_I^{-1} \mathbf{s}_{sub}$ , is not an exact match to the true signal. When a reduced-dimension clutter mitigation method is used, the loss in SINR due to a phase mismatch between  $\mathbf{s}_{sub}$  and the true signal,  $\mathbf{s}$ , is given by

$$L_4 = \frac{SINR_{sub}}{SINR_{rd}} = \left( \frac{|\mathbf{w}_{sub}^H \mathbf{s}|^2}{\mathbf{w}_{sub}^H \mathbf{R}_{l,rd} \mathbf{w}_{sub}} \right) \bigg/ \left( \frac{|\mathbf{w}_{rd}^H \mathbf{s}|^2}{\mathbf{w}_{rd}^H \mathbf{R}_{l,rd} \mathbf{w}_{rd}} \right). \quad (2.20)$$

When clutter mitigation methods use the full covariance matrix, the reduced dimension loss equals one, and  $L_4$  is given as

$$L_4 = \frac{SINR_{sub}}{SINR_{opt}} = \frac{|\mathbf{w}_{sub}^H \mathbf{s}|^2}{(\mathbf{w}_{sub}^H \mathbf{R}_I \mathbf{w}_{sub})(\mathbf{s}^H \mathbf{R}_I^{-1} \mathbf{s})}. \quad (2.21)$$

If the phase component of the spatial and slow-time signal is expressed as  $\mathbf{s}_\phi = \exp(j\phi)$ , where  $\phi$  includes both the spatial and temporal phases, loss in output SINR results when  $\mathbf{w}$  includes a phase error,  $\epsilon$ , that is mismatched in spatial and/or temporal phase from  $\mathbf{s}_\phi$ :  $\mathbf{w} = \exp(j(\phi + \epsilon))$ . In a noise-limited environment, the modeling loss,  $L_4$ , is

$$L_4 = \frac{SINR_{sub}}{SINR_{opt}} = \frac{|(\exp(j(\phi + \epsilon)))^H \exp(j\phi)|^2}{N^2 M^2} = \frac{\left| \sum_0^{MN-1} \exp(-j\epsilon_{n,m}) \right|^2}{N^2 M^2}, \quad (2.22)$$

where  $\epsilon$  represents the phase error in vector form and  $\epsilon_{n,m}$  represents the phase error as a function of pulse number and spatial channel.

### 2.5.2 Minimum Detectable Velocity

Minimum detectable velocity (MDV) is a performance metric that shows the loss in output SINR as a function of target radial velocity for a particular processing method in relation to optimal SNR. MDV shows the effects of clutter mitigation, which suppresses signal energy in the Doppler region associated with stationary clutter, on target detection. For the broadside collection geometry assumed in this research, the clutter is clustered in the low Doppler region, and the MDV metric shows the effects of clutter mitigation on low radial velocity targets.

## **2.6 Target Motion Assumptions**

### **2.6.1 Straight Line Assumption**

Targets in this research are ground vehicles whose movements over the dwell are assumed to be straight line motion components of velocity, acceleration, and jerk in directions tangential and radial to platform motion. This model assumes the target is traveling on a straight road with minimal back-and-forth weaving within a single lane. Experiments described by Soliday in [40] show that vehicle positions within a single traffic lane are distributed normally with a standard deviation of 13 cm from the driver's chosen position. The average time for a vehicle traveling at 25 m/s to weave more than one standard deviation within a single lane is 13 seconds. For the GMTI data collection times used for algorithm development and evaluation in this dissertation, weaving by 13 cm over a 13-second time interval can be considered approximately straight. The algorithm concepts presented herein may possibly be applied to target motion on curved roadways or for vehicles making turns for a limited dwell time over which vehicle motion appears approximately straight.

### **2.6.2 Maximum Acceleration Assumption**

A maximum target acceleration of  $1.0 \text{ m/s}^2$  is used in this research for algorithm development and evaluation. Target radial acceleration is the strongest contributor to the quadratic phase component. Thus, radial acceleration establishes the dwell time over which the target can be accurately modeled with a linear phase. As radial acceleration increases, the time at which the linear-phase model and the true target signal become decorrelated decreases. With a maximum radial acceleration of  $1.0 \text{ m/s}^2$ , the slow-time signal for the two algorithms presented herein can be modeled with a linear phase for a dwell time of



approximately 100 ms for typical GMTI radar parameters [41]. Radial acceleration greater than  $1.0 \text{ m/s}^2$  would degrade algorithm performance for the single-sample input SNR values evaluated, or equivalently, would require an increase in single-sample input SNR to achieve comparable algorithm results.

In [42], Long establishes maximum and typical initial acceleration values for a variety of vehicles with different weight to horsepower ratios. Acceleration information is provided for a vehicle with a weight to horsepower ratio of 35 lb/hp, which is typical for a likely target of interest, the multipurpose military vehicle [43]. Typical target acceleration was measured to be approximately 60% of maximum acceleration. On average, vehicles with a higher weight to horsepower ratio have lower rates of acceleration. Experimental data in [42] gives a maximum initial acceleration of  $2.16 \text{ m/s}^2$  and typical initial acceleration of  $1.30 \text{ m/s}^2$  for the 35 lb/hp vehicle.

For straight line motion, acceleration typically decreases linearly with time as the driver approaches desired speed [42]. Thus, initial acceleration from a rest position likely represents the highest vehicle acceleration rates. In the worst-case scenario of a vehicle accelerating from rest with the entire component of acceleration in the radial direction, a slight decrease in algorithm performance is expected as previously mentioned.

Since acceleration decreases approximately linearly with speed, most values for typical radial acceleration are within the upper bound of  $1.0 \text{ m/s}^2$  used in this research. The linear decrease in acceleration over the time in which a vehicle is accelerating justifies a constant component of jerk assumed in this research.

## CHAPTER 3

### SIGNAL MODELS

#### 3.1 Target Signal

Pulsed radar is assumed with the return signal equal to a delayed and scaled version of the transmitted signal. The multichannel signal model is developed as the generic model and can be extended to the single-channel model by setting  $M$ , the number of spatial channels, to one.

The expression for the received target signal can be derived from the transmitted waveform. Assuming the waveform is a series of coherent pulses, the expression for the transmitted waveform is:

$$s(t) = a_t u(t) \exp(\psi) \exp(j(2\pi f_c t + \pi \frac{\beta}{\tau} t^2)) \quad (3.1)$$

where  $a_t$  is the transmitted signal amplitude,  $u(t) = \sum_{n=0}^{N-1} u_p(t - nT)$  is the signal's complex envelope with  $u_p(t)$  equal to the complex envelope of a single pulse of duration  $\tau$ ,  $\psi$  is a random phase uniformly distributed on  $[0, 2\pi)$ ,  $n$  is the pulse number,  $T$  is the PRI,  $f_c$  is the center frequency, and  $\beta$  is the bandwidth of the LFM signal.

The target is modeled as a point source, or nonfluctuating target, whose RCS is assumed constant over the dwell time. The echo received by the  $m^{th}$  channel from a single pulse is given by

$$s_m(t) = \alpha_r u(t - \tau_m) \exp(j2\pi f_c (t - \tau_m)) \exp(j\psi) \exp(j\pi \frac{\beta}{\tau} (t - \tau_m)^2), \quad (3.2)$$

where  $\alpha_r$  is a complex amplitude term whose magnitude is proportional to the square root of the target RCS and  $\tau_m$  is the time delay to the  $m^{th}$  channel. The delay to the  $m^{th}$  channel can be written as the combined round trip time delay,  $t_d$ , to the target and back to the array reference point and the relative delay,  $t_m$ , from the array reference point to the  $m^{th}$  channel:

$$\tau_m = t_d + t_m. \quad (3.3)$$

The relative delay to the  $m^{th}$  channel is insignificant within the complex envelope so that the received echo can be written

$$s_m(t) = \alpha_r u(t - t_d) \exp(j2\pi f_c(t - \tau_m)) \exp(j\psi) \exp(\pi \frac{\beta}{\tau} (t - \tau_m)^2). \quad (3.4)$$

After down-conversion to baseband, the received signal is

$$s_m(t) = a_r u(t - t_d) \exp(-j2\pi f_c(t_d + t_m)) \exp(j\pi \frac{\beta}{\tau} (t - (t_d + t_m))^2), \quad (3.5)$$

for  $a_r = \alpha_r \exp(j\psi)$ . The received fast-time signal at each channel is processed with a matched filter [44] that compresses the LFM pulse waveform and maximizes the single-sample SNR of the signal at a particular range. After matched filtering and sampling with an A/D converter, the expression for the received signal at the  $m^{th}$  channel and  $n^{th}$  pulse is given as [4]:

$$s(m, nT) = a_r \exp(-j2\pi f_c t_d(nT)) \exp(-j2\pi f_c t_m(nT)). \quad (3.6)$$

The conventional space-time processing model simplifies the expressions for the time delays,  $t_d(nT)$  and  $t_m(nT)$ . The approximations are accurate for a short dwell but create a phase mismatch between the conventional signal model and the true signal that limits processing gains as dwell time is extended.

### 3.1.1 Conventional Temporal and Spatial Signal Models

#### 3.1.1.1 Linear-Phase Temporal Signal Model

The time delay,  $t_d(nT)$ , between signal transmission and reception depends on the range between the array reference point and the target, which changes from pulse to pulse. This time delay is equal to twice the slow-time range expression,  $R(nT)$ , divided by the propagation speed,  $c$  [26]:

$$t_d(nT) = 2R(nT) / c. \quad (3.7)$$

Substituting (3.7) into (3.6) and letting  $f_c = c / \lambda_c$ , the temporal phase factor,  $\exp(-j2\pi f_c t_d(nT))$ , can be written as  $\exp(-j4\pi R(nT) / \lambda_c)$ .

The range between the target and the platform can be expressed as

$$R(nT) = r_0 + \Delta r(nT), \quad (3.8)$$

where  $r_0$  is the initial range between the target and the array reference point, and  $\Delta r(nT)$  is the slow-time change in range [3]. The change in phase over the dwell time, not the absolute phase, is exploited for target information; thus the constant,  $r_0$ , can be disregarded for signal processing purposes. Conventional space-time processing approximates the slow-time change in range as a linear function of target radial velocity,  $V_y$ :

$$\Delta r(nT) \cong V_y nT. \quad (3.9)$$

The temporal phase factor is simplified to  $\exp(j2\pi f_D nT)$  by substituting  $V_y nT$  for  $R(nT)$  and replacing  $-2V_y / \lambda_c$  with  $f_D$ , the Doppler frequency [27]. This linear phase factor, written as a vector for  $n$  from 0 to  $N-1$ , is called the temporal steering vector [3, 4]:

$$\mathbf{s}_t(f_D) = [1 \quad \exp(j2\pi f_D T) \quad \cdots \quad \exp(j2\pi f_D (N-1)T)]'. \quad (3.10)$$

### 3.1.1.2 Fixed-Angle Spatial Signal Model

The typical range between the antenna array and the area of interest on the ground is such that a far field plane wave can be assumed for the received signal at the array. For a signal arriving from elevation angle,  $\theta$ , and azimuth angle,  $\varphi$ , the relative time delay between the array reference and the  $m^{th}$  channel is:

$$t_m = \frac{\hat{k}(\theta, \varphi) \cdot \hat{d}_m}{c}, \quad (3.11)$$

where  $\hat{k}(\theta, \varphi)$  is the unit vector from the platform to the target as shown in Figure 3.1, and  $\hat{d}_m$  is a vector representing channel position [4].

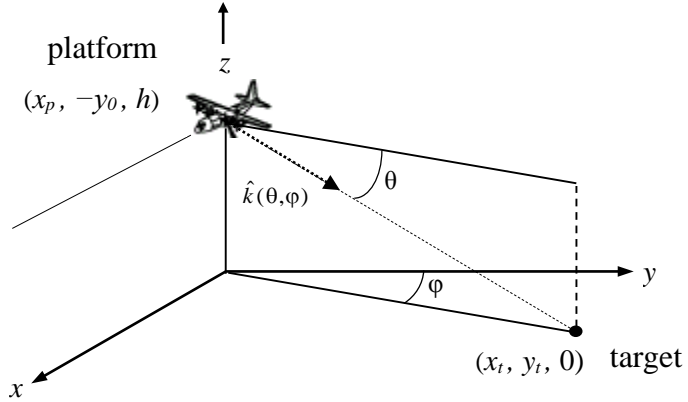


Figure 3.1. Geometry of platform and ground target at elevation angle,  $\theta$ , and azimuth angle,  $\varphi$ .

Figure 3.2 shows the top view of a signal from angle  $\varphi$  impinging on a uniform linear array (ULA) [45] with channel spacing  $d$  to illustrate the relationship between the angle of arrival (AOA),  $\varphi$ , and the relative distance between channels.

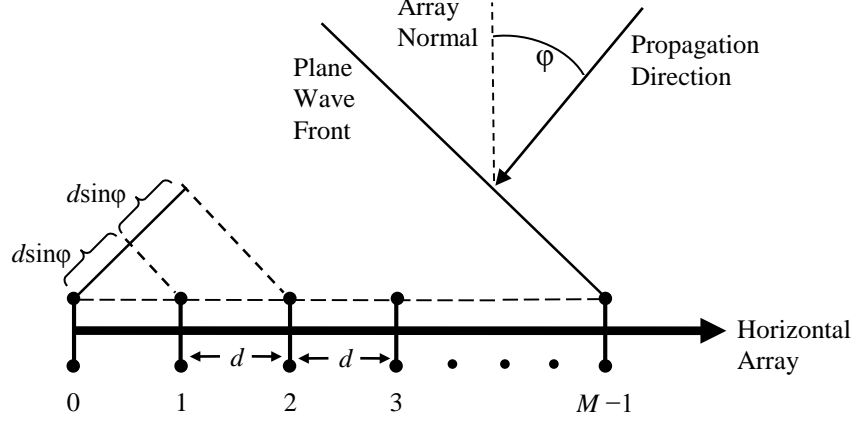


Figure 3.2. Array geometry.

For a ULA with channel spacing  $d$ , (3.11) simplifies to

$$t_m = - \frac{md \cos \theta \sin \phi}{c}. \quad (3.12)$$

Conventional space-time processing assumes a fixed AOA over the dwell. Defining spatial frequency as  $\vartheta = d \cos \theta \sin \phi / \lambda_c$ , the spatial factor,  $\exp(-j2\pi f_c t_m)$ , from (3.6) simplifies to a fixed-angle spatial phase factor,  $\exp(j2\pi m \vartheta)$ . This spatial phase factor, written as a vector for  $m$  from 0 to  $M-1$ , is called the spatial steering vector [3, 4]:

$$\mathbf{s}_s(\vartheta) = [1 \quad \exp(j2\pi \vartheta) \cdots \exp(j2\pi(M-1)\vartheta)]'. \quad (3.13)$$

### 3.1.1.3 Target Steering Vector

The target steering vector,  $\mathbf{s}_{s,t}(\vartheta, f_D)$ , used as the space-time signal model in conventional processing is formed from the Kronecker product [46] of the temporal and spatial steering vectors:  $\mathbf{s}_{s,t}(\vartheta, f_D) = \mathbf{s}_t(f_D) \otimes \mathbf{s}_s(\vartheta)$ . This linear-phase, fixed-angle model is a simplified approximation of the target signal. The phase mismatch between this simplified conventional signal model and the true space-time target signal reduces output SINR as dwell time increases.

### 3.1.2 True Temporal and Spatial Signals

#### 3.1.2.1 True Temporal Phase

As dwell time increases, the slow-time range approximation from (3.9) becomes an inaccurate representation of the actual change in range over the CPI. The aircraft and target positions change over the dwell and create a range expression that is a complex function of platform velocity and target motion. A platform with height  $h$  and ground range offset  $y_0$  from scene center, traveling in the  $x$  direction at velocity  $V_p$  from starting point  $-V_p(N/2)T$  to ending point  $V_p(N/2)T$  is at a position over the dwell given by

$$P_p = (-V_p(N/2)T + V_p nT, -y_0, h). \quad (3.14)$$

A moving target at initial coordinates  $(x_1, y_1, 0)$  measured from scene center  $(0, 0, 0)$ , with initial velocity vector  $V_x \cdot \vec{x} + V_y \cdot \vec{y}$ , acceleration vector  $A_x \cdot \vec{x} + A_y \cdot \vec{y}$ , and jerk vector  $J_x \cdot \vec{x} + J_y \cdot \vec{y}$  is at a position over the dwell given by

$$P_t = (x_1 + V_x nT + 1/2 A_x (nT)^2 + 1/6 J_x (nT)^3, y_1 + V_y nT + 1/2 A_y (nT)^2 + 1/6 J_y (nT)^3, 0). \quad (3.15)$$

Assuming negligible intrapulse motion, the range between the platform and the target as a function of slow-time is given as:

$$R(nT) = \sqrt{(x_1 + V_x nT + 1/2 A_x (nT)^2 + 1/6 J_x (nT)^3 + V_p(N/2)T - V_p nT)^2 + (y_1 + V_y nT + 1/2 A_y (nT)^2 + 1/6 J_y (nT)^3 + y_0)^2 + h^2}. \quad (3.16)$$

Expanding (3.16) by grouping like terms, letting  $r^2 = y_0^2 + h^2$ , and taking the first two terms of the Taylor series expansion for the square root operation gives the slow-time range approximation [41],

$$\begin{aligned}
R(nT) \cong & r + \frac{V_x(x_1 + V_p(N/2)T) - V_p(x_1 + V_p(N/2)T) + V_y(y_1 + y_0)}{r} nT \\
& + \frac{A_x(x_1 + V_p(N/2)T) + A_y(y_1 + y_0) + V_x^2 + V_p^2 + V_y^2 - 2V_x V_p}{2r} (nT)^2 \\
& + \frac{3A_x(V_x - V_p) + 3A_y V_y + J_x(x_1 + V_p(N/2)T) + J_y(y_1 + y_0)}{6r} (nT)^3 \\
& + \frac{3A_x^2 + 3A_y^2 + 4J_x(V_x - V_p) + 4J_y V_y}{24r} (nT)^4 + \frac{J_x A_x + J_y A_y}{12r} (nT)^5 + \frac{J_x^2 + J_y^2}{72r} (nT)^6.
\end{aligned} \tag{3.17}$$

The phase as a function of slow time is determined by multiplying the range expression in (3.17) by  $-4\pi/\lambda_c$ :

$$\psi(nT) = \left( \frac{-4\pi}{\lambda_c} \right) R(nT). \tag{3.18}$$

The true slow-time target signal contains quadratic and higher-order phase terms in addition to the linear-phase term assumed in Fourier-based processing. The nonlinear phase components are listed in Table 3.1 by phase order [41].

Table 3.1. Nonlinear phase expressions.

<i>Phase Order</i>	<i>Phase Component</i>
$2^{nd*}$	$\psi_2(nT) \cong \left( \frac{-2\pi}{\lambda_c r} \right) (A_x(x_1 + V_p(N/2)T) + A_y(y_1 + y_0) + V_x^2 + V_p^2 - 2V_x V_p)(nT)^2$
$3^{rd}$	$\psi_3(nT) \cong \left( \frac{-2\pi}{3\lambda_c r} \right) (3A_x(V_x - V_p) + 3A_y V_y + J_x(x_1 + V_p(N/2)T) + J_y(y_1 + y_0))(nT)^3$
$4^{th}$	$\psi_4(nT) \cong \left( \frac{-\pi}{6\lambda_c r} \right) (3A_x^2 + 3A_y^2 + 4J_x(V_x - V_p) + 4J_y V_y)(nT)^4$
$5^{th}$	$\psi_5(nT) \cong \left( \frac{-\pi}{3\lambda_c r} \right) (J_x A_x + J_y A_y)(nT)^5$
$6^{th}$	$\psi_6(nT) \cong \left( \frac{-\pi}{18\lambda_c r} \right) (J_x^2 + J_y^2)(nT)^6$

\*Quadratic term from platform motion cancelled



Note that the ground range offset,  $y_0$ , between the platform and scene center is approximately equal to the slant range,  $r$ , at low grazing angle; thus, the quadratic and cubic phase terms,  $(-2\pi A_y y_0 / \lambda_0 r)(nT)^2$  and  $(-2\pi J_y y_0 / 3\lambda_0 r)(nT)^3$ , that include  $y_0$  are the most substantial of these nonlinear components.

Maximizing output SINR requires an improved signal model that considers the effects of the nonlinear phase components in the extended-dwell temporal signal.

### 3.1.2.2 True Spatial Phase

The relative delay term,  $t_m(nT)$ , for the received signal at the  $m^{\text{th}}$  channel of an  $M$ -channel array changes in slow-time as the platform moves past the area of interest on the ground. This relative time delay is given as

$$t_m(nT) = - \frac{md \cos \theta(nT) \sin \phi(nT)}{c}, \quad (3.19)$$

where  $\phi(nT)$  is the slow-time expression for the azimuth angle between the platform and the target measured from broadside and  $\theta(nT)$  is the slow-time expression for the elevation angle between the platform and the target.

The  $\cos\theta(nT)$  factor in (3.19) is equal to the ground range from platform to target divided by the slant range from platform to target. Even over an extended dwell time, the change in  $\cos\theta(nT)$  can be assumed to be negligible because the height of the platform,  $h$ , remains constant over the dwell and  $y_0 \gg h$ .

The  $\sin\phi(nT)$  factor in (3.19) is equal to the difference in  $x$ -coordinate positions given in (3.14) and (3.15) between the target and the platform reference point divided by the ground range:

$$\sin \phi(nT) = (P_{tx} - P_{px}) / \sqrt{(y_0^2 + (P_{tx} - P_{px})^2)}. \quad (3.20)$$

Substituting the terms from (3.14) and (3.15) that most significantly change the azimuth angle over the dwell yields the approximation,

$$\sin \varphi(nT) \cong \frac{V_p (N/2)T - V_p nT}{y_0}. \quad (3.21)$$

Maximizing output SINR requires considering the effects of the change in  $\varphi$  on integration of the extended dwell time spatial signal.

### 3.2 SINR Loss from Target Signal Approximations

The target steering vector,  $\mathbf{s}_{s-t}(\vartheta, f_D)$ , is the space-time target signal model based on approximations when target parameters are unknown. Approximating the signal as  $\mathbf{s}_{s-t}(\vartheta, f_D)$  causes a loss in output SINR due to the modeling loss factor,  $L_4$ , as described in chapter 2. The losses in output SINR from assuming a linear-phase temporal signal model are detailed in the next two sections, while the potential loss from assuming a fixed spatial angle over the dwell is detailed in section 3.2.3.

#### 3.2.1 Linear-Phase Modeling Loss

The linear-phase signal model used in Fourier-based processing is a simplified approximation of the slow-time target signal [47]. The slow-time signal model in (3.10),  $\mathbf{s}_t(f_D) = [1 \ \exp(j2\pi f_D T) \cdots \exp(j2\pi f_D (N-1)T)]'$ , is a vector of linear-phase terms, whereas the true target signal model contains linear-phase and nonlinear-phase terms:

$$\mathbf{s}_{true}(f_D) = [1 \ \exp(j2\pi f_D T) \exp(j\gamma_1) \cdots \exp(j2\pi f_D (N-1)T) \exp(j\gamma_{(N-1)})]'. \quad (3.22)$$

The nonlinear phase terms,  $\gamma_1, \dots, \gamma_{(N-1)}$  create a phase mismatch between the true signal and the model that reduces SINR as dwell time increases.

The true slow-time signal phase is shown over a one-second dwell time in Figure 3.3 with and without the linear component for the radar and target parameters given in Table 3.2.

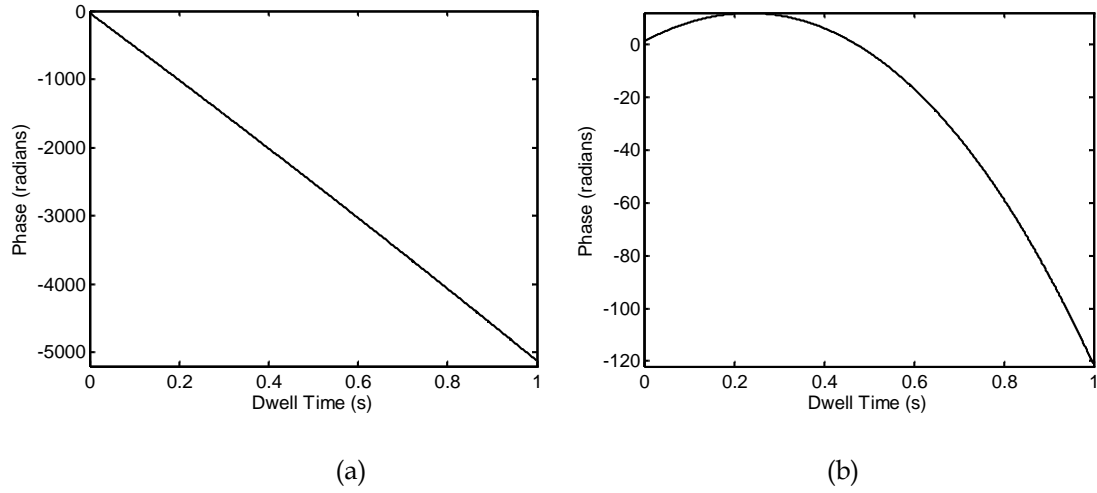


Figure 3.3. Slow-time phase: (a) actual and (b) without linear component [47].

Table 3.2. Radar and target parameters for phase analysis.

<i>Parameter</i>	<i>Magnitude</i>
Center frequency, $f_c$	10 GHz
Platform velocity, $V_p$	100 m/s
Platform height, $h$	3 km
Slant range, $r$	20 km
Target radial and tangential velocity, $V_y$ and $V_x$	15.0 m/s
Target radial and tangential acceleration, $A_y$ and $A_x$	1.0 m/s <sup>2</sup>
Target radial and tangential jerk, $J_y$ and $J_x$	0.5 m/s <sup>3</sup>

Over a sufficiently short dwell time, the nonlinear phase components are insignificant, and the linear-phase model used in Fourier-based processing is a close match to the actual target signal. The resulting output SINR is close to optimal. The linear-phase model becomes less accurate with increased dwell time as the nonlinear components begin

to contribute more substantially to the target signal phase as shown in Figure 3.3(b). The temporal phase mismatch between the true target signal and the linear-phase model creates destructive interference that reduces the output SINR as dwell time increases.

Output SNR for Fourier-based processing, assuming a linear-phase signal model, is compared to output SNR for optimal processing with the clairvoyant model in Figure 3.4 for a dwell time of 500 ms. Target parameters are listed in Table 3.2. A noise-limited environment is assumed with a single-sample input SNR of  $-10$  dB.

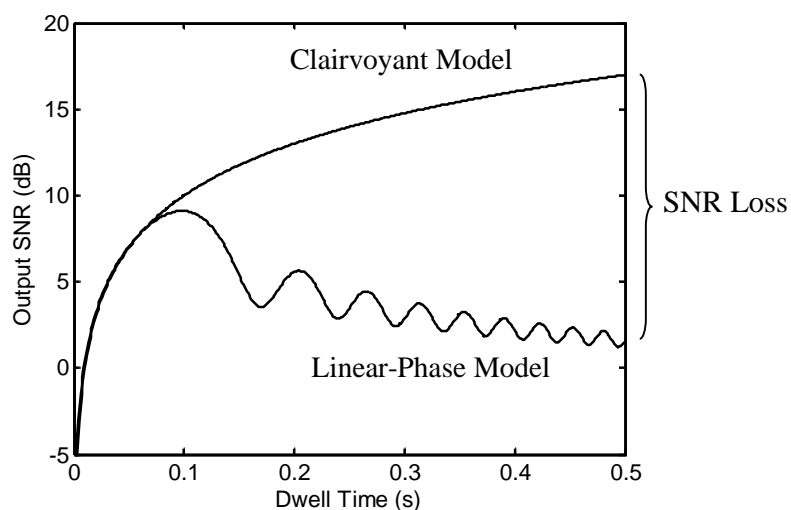


Figure 3.4. SNR as a function of dwell time for the clairvoyant model and the linear-phase model.

The coherent integration time in Figure 3.4 for the linear-phase model is approximately 100 ms. For typical radar and target parameters, increasing the dwell time beyond 100 ms reduces output SNR. Detection of very weak targets requires more samples for detection, which necessitates an alternative to the conventional linear-phase temporal signal model.

### 3.2.2 Loss as a Function of Target Motion

The quadratic phase component of the target signal is dominated by the target motion parameters of radial acceleration and tangential velocity. If these parameters are not considered in the slow-time signal model, the mismatch creates a loss in SNR that increases with dwell time, velocity, and acceleration as shown in Figure 3.5 [47]. The SNR loss in comparison to optimal SNR is shown as a function of tangential velocity for dwell times of 200 and 400 milliseconds. SNR loss is shown as a function of radial acceleration for dwell times of 100, 200, and 400 milliseconds.

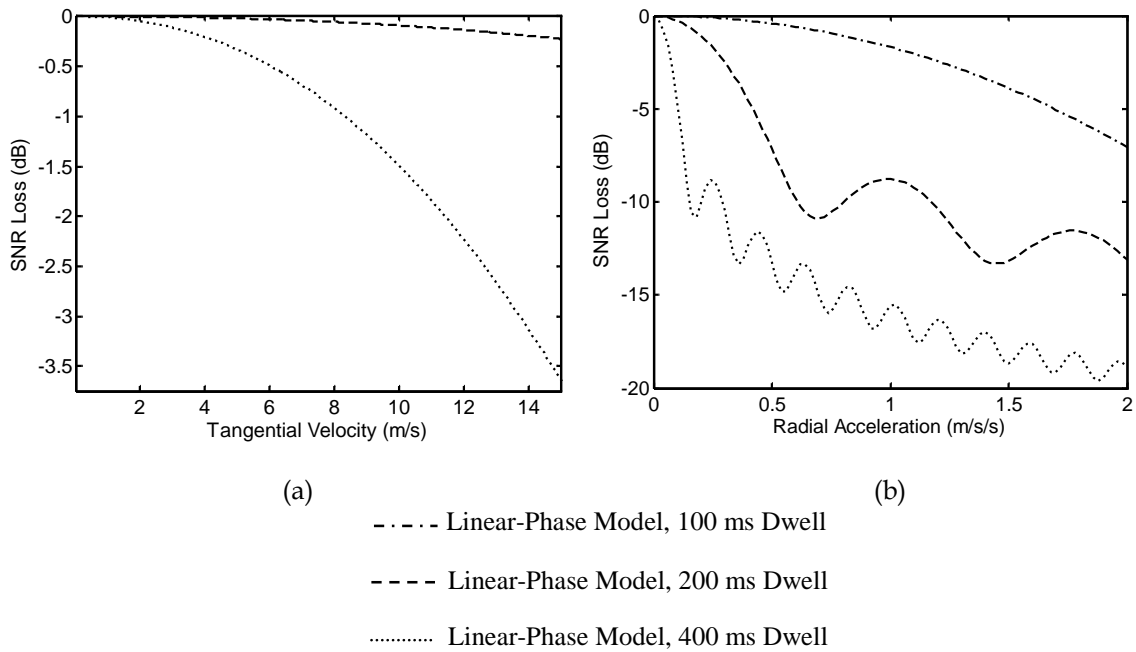


Figure 3.5. SNR loss as a function of (a) tangential velocity and (b) radial acceleration [47].

A comparison of Figures 3.5(a) and (b) shows that, in general, target radial acceleration causes greater SNR loss than tangential velocity over the same dwell time.

### 3.2.3 Spatial Phase Decorrelation

The angle between the platform and the target changes over the dwell as the platform moves past the area of interest on the ground. The change in AOA of the target signal affects the coherent integration of spatial samples. As dwell time increases, the change in AOA causes a mismatch between the true spatial phase and the fixed-angle model corresponding to a particular look angle. Since target motion is unknown a priori, efforts to predict this change in angle complicate the detection problem. Operation within the time that the AOA can be considered approximately constant is desirable. We will consider the AOA approximately constant over the time period that integration of spatial data contributes positively to output SNR.

The true spatial phase and the fixed-angle spatial model can be written as vectors for channels 0 through  $M-1$ . The inner product of the fixed-angle model and the received spatial signal integrates signal energy from a particular AOA for a limited time. At the point of complete decorrelation, the inner product of these vectors is equal to zero. Extending the dwell time beyond this point decreases output SNR. To estimate the point of complete spatial decorrelation, we begin with the specific case of a three-channel ULA with a center channel as the reference point and a single channel at each end, and then we extend the concept to the general case of the  $M$ -channel array.

The received signal at the array reference point has no relative delay; spatial weighting for this channel is equal to  $\exp(j0) = 1$ . Substituting the relative delay,  $t_m = -md \cos \theta \sin \phi / c$ , into the spatial phase factor,  $\exp(-j2\pi f_c t_m (nT))$  from (3.6), with  $m = \pm 1$  for the channels at each end, the fixed-angle spatial weight vector from (3.13) that integrates target samples from azimuth angle  $\phi$  with respect to the center of the aperture is

$$\mathbf{s}_{s, \text{fixed}} = \begin{bmatrix} \exp(j \frac{2\pi}{\lambda_c} d \cos \theta \sin \varphi) & 1 & \exp(-j \frac{2\pi}{\lambda_c} d \cos \theta \sin \varphi) \end{bmatrix}'. \quad (3.23)$$

The true spatial phase vector for a target at azimuth angle  $\varphi$  measured with respect to the center of the aperture is

$$\mathbf{s}_s = \begin{bmatrix} \exp(j \frac{2\pi}{\lambda_c} d \cos \theta \sin(\varphi + \Delta\varphi(nT))) & 1 & \exp(-j \frac{2\pi}{\lambda_c} d \cos \theta \sin(\varphi + \Delta\varphi(nT))) \end{bmatrix}', \quad (3.24)$$

where  $\Delta\varphi(nT)$  represents the difference between the true AOA and the fixed angle,  $\varphi$ , as a function of dwell time. Using the small angle approximation for sine and assuming  $\theta$  is approximately zero, the inner product of (3.23) and (3.24) is given as

$$\mathbf{s}_{s, \text{fixed}}^H \mathbf{s}_s \cong \exp(j \frac{2\pi}{\lambda_c} d \Delta\varphi(nT)) + 1 + \exp(-j \frac{2\pi}{\lambda_c} d \Delta\varphi(nT)). \quad (3.25)$$

Setting the right side of (3.25) to zero for complete decorrelation, we solve the equation,

$$\exp(j \frac{2\pi}{\lambda_c} d \Delta\varphi(nT)) + \exp(-j \frac{2\pi}{\lambda_c} d \Delta\varphi(nT)) = -1, \quad (3.26)$$

to determine the change in angle that causes complete decorrelation. Dividing both sides of (3.26) by two allows the equation to be written as

$$\cos(2\pi d \Delta\varphi(nT) / \lambda_c) = -1/2. \quad (3.27)$$

Taking  $\cos^{-1}$  of both sides of (3.27) gives the equation,

$$(2\pi d \Delta\varphi(nT) / \lambda_c) = 2\pi/3. \quad (3.28)$$

Rearranging (3.28), we solve for the change in angle that causes complete decorrelation,

$$\Delta\varphi(nT) = \lambda_c / 3d. \quad (3.29)$$

Eqn. (3.29) gives the expression for the angle change over the dwell that completely decorrelates the signal for the three-channel array. The general expression for spatial

decorrelation between the fixed-angle model and the true spatial phase for an  $M$ -channel ULA can be derived starting with the expression in (3.24) for the approximate phase mismatch between the fixed-angle model and the true spatial phase at the  $m^{th}$  channel,

$$\exp(j \frac{2\pi}{\lambda_c} m d \Delta\phi(nT)). \quad (3.30)$$

The phase mismatch begins to reduce output SINR at the point of complete decorrelation, which occurs when the inner product of the true spatial phase vector and the fixed-angle model equals zero, or equivalently when

$$\sum_m \exp(j \frac{2\pi}{\lambda_c} m d \Delta\phi(nT)) = 0. \quad (3.31)$$

To determine the point of decorrelation, the spatial phases in (3.31) can be positioned around a unit circle such that their sum is zero. For a ULA with evenly spaced channels, the phases are equally spaced around the unit circle, with the array reference at 0 radians. For the general case, we can either assume an array reference point at the end of the array and sum from 0 to  $M-1$  or assume the array reference point is in the center and sum from  $-(M-1)/2$  to  $(M-1)/2$  for  $M$  odd. Phases for the  $m$  channels are spaced  $2\pi/M$  apart on the unit circle and are located at the points  $2\pi m/M$  as shown in Figure 3.6 for  $M = 3, 4$ , and 5.

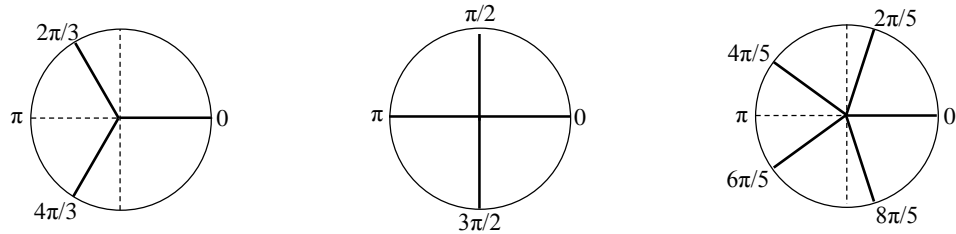


Figure 3.6. Phases shown on unit circle (left to right) for  $M = 3$ ,  $M = 4$ , and  $M = 5$  that completely decorrelate the spatial signal.



The spatial phase at the  $m^{th}$  channel that contributes to spatial decorrelation is

$$2\pi m d \Delta\phi(nT) / \lambda_c = 2\pi m / M. \quad (3.32)$$

Solving (3.32) for the change in angle yields:

$$\Delta\phi(nT) = \lambda_c / M d, \quad (3.33)$$

which is a generalized version of (3.29) for an  $M$ -channel array.

For an AOA defined with respect to array broadside at the center of the aperture, the azimuth distance of the platform from the aperture center at the beginning and end of the dwell is the primary limiting factor in spatial coherence. A top view of the radar geometry in Figure 3.7 shows the points of decorrelation at the beginning and end of the dwell due to the platform distance from the center of the aperture. Only platform motion is considered for simplicity.

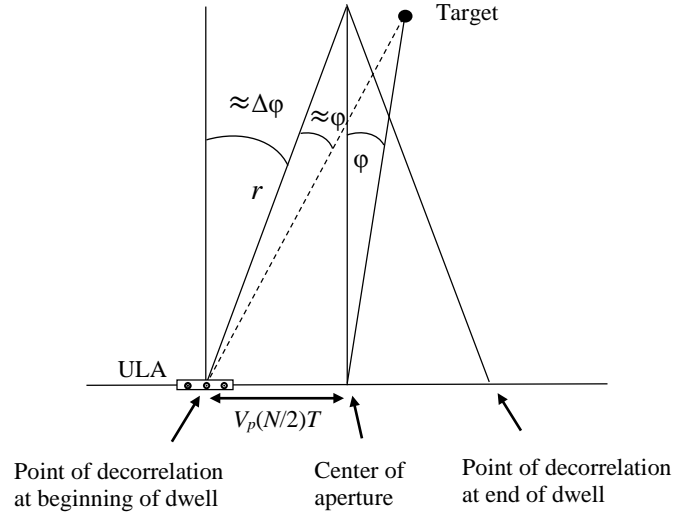


Figure 3.7. Top view of radar geometry showing extent of angle at beginning and end of dwell that causes decorrelation with fixed-angle signal model.

From the geometry shown in Figure 3.7, the expression for the maximum angle extent is approximated as

$$\Delta\phi(nT) \cong \frac{V_p (N/2)T}{r}. \quad (3.34)$$

Equating (3.33) and (3.34) and rearranging the equation gives an expression for the dwell time required for complete decorrelation:

$$NT \cong 2r\lambda_c / MV_p d. \quad (3.35)$$

The component of target velocity,  $V_t$ , tangent to platform velocity can also affect decorrelation time. However, for  $V_p \gg V_t$ , (3.35) is an accurate estimate for spatial decorrelation time for an  $M$ -channel array.

### 3.3 Clutter Model

Reflections from stationary objects or clutter on the ground interfere with the detection of a moving target. All of the individual objects, or scatterers, located an equal distance from the radar platform contribute to the clutter signal in a particular range cell. Each range cell is divided into azimuth bins or patches whose reflected energy contains the combined contributions of the scatterers in the patch.

The subscript,  $c$ , used with frequency and wavelength is consistent throughout this dissertation in representing center frequency and associated wavelength, while  $c$  by itself represents propagation speed. In this section, the subscript,  $c$ , on a signal indicates clutter.

The clutter is assumed to be homogeneous [48] and comprised of a large number of independent scatterers with Gaussian distributed amplitudes. For simplicity, no intrinsic clutter motion is assumed, and the clutter is modeled as unambiguous in range. The RCS

of the clutter in the  $q^{th}$  patch,  $\sigma_q$ , depends on the patch area, which is bounded by range and azimuth resolution:

$$\sigma_q = \sigma^0 (\text{patch area}), \quad (3.36)$$

where  $\sigma^0$  is the clutter reflectivity of the patch assuming the constant Gamma model:

$$\sigma^0 = \gamma \sin \psi_q. \quad (3.37)$$

In (3.37),  $\gamma$  is a terrain-dependent parameter and  $\psi_q$  is the grazing angle to the  $q^{th}$  clutter patch [49]. In this simulation, the parameter,  $\gamma$ , represents heavy land clutter.

The received space-time signal from the  $q^{th}$  clutter patch at a particular range after pulse compression, down conversion, and sampling is

$$x_{c,q}(m, nT) = \alpha_q \exp(-j2\pi f_c t_{m,q}(m)) \exp(-j2\pi f_c t_{d,q}(nT)), \quad (3.38)$$

where  $\alpha_q$  is a complex amplitude term proportional to the square root of the clutter RCS in the  $q^{th}$  patch [50]. The clutter-to-noise ratio (CNR) in the  $q^{th}$  patch is given by

$$\xi_q = \left( \frac{P_t G^2 \lambda_c^2 \sigma_q}{(4\pi)^3 r^4 L_s \sigma_n^2} \right), \quad (3.39)$$

where  $P_t$  is the transmitted power,  $G$  is the antenna gain,  $r$  is the range to the patch,  $L_s$  is the system loss, and  $\sigma_n^2$  is the noise power. The clutter power in the  $q^{th}$  patch can be expressed as

$$E[|\alpha_q|^2] = \left( \frac{P_t G^2 \lambda_c^2 \sigma_q}{(4\pi)^3 r^4 L_s} \right) = \sigma_n^2 \xi_q. \quad (3.40)$$

For a ULA with channel spacing  $d$ , the relative delay at the  $m^{th}$  channel of the received signal from the  $q^{th}$  clutter patch is given by

$$t_{m,q} = - \frac{md \cos \theta_q(nT) \sin \phi_q(nT)}{c}, \quad (3.41)$$

where  $\theta_q$  is the elevation angle and  $\phi_q$  is the azimuth angle to the  $q^{th}$  clutter patch.

The time delay between signal transmission and reception of the echo from the  $q^{th}$  clutter patch is

$$t_{d,q}(nT) = 2R_q(nT) / c, \quad (3.42)$$

where  $R_q(nT)$  is the slow-time range expression between the platform and the  $q^{th}$  clutter patch. Substituting (3.41) and (3.42) into (3.38) and summing over all  $Q$  clutter patches, gives an expression for the received clutter signal as a function of channel and pulse number at a particular range from the platform:

$$x_c(m, nT) = \sum_{q=1}^Q \alpha_q \exp(j2\pi md \cos \theta_q(nT) \sin \phi_q(nT) / \lambda_c) \exp(-j4\pi R_q(nT) / \lambda_c). \quad (3.43)$$

The range between the radar platform and the  $q^{th}$  clutter patch at  $(x_q, y_q, 0)$  is given by

$$R_q(nT) = \sqrt{(x_q + V_p(N/2)T - V_p nT)^2 + (y_q + y_0)^2 + h^2}. \quad (3.44)$$

Taking the first two terms of the series expansion of the square root expression, multiplying by  $-4\pi / \lambda_c$ , letting  $r^2 = y_0^2 + h^2$ , and removing constant phase and platform dependent terms gives the slow-time phase approximation for the clutter signal from the  $q^{th}$  patch,

$$\psi_q(nT) \cong \frac{4\pi}{r\lambda_c} (x_q V_p nT). \quad (3.45)$$

The time derivative of the phase divided by  $2\pi$  is equal to the Doppler frequency associated with each clutter patch,

$$f_{D_q} = 2x_q V_p / r\lambda_c. \quad (3.46)$$

The combined returns from all  $Q$  clutter patches spread energy among multiple Doppler

frequency bands. The azimuth position of the  $q^{th}$  clutter patch in relation to the platform varies slightly over an extended dwell as the platform moves past the area of interest on the ground; thus, each clutter patch is actually associated with a time-varying Doppler frequency,

$$f_{D_q} = 2x_q(nT)V_p / r\lambda_c, \quad (3.47)$$

that depends on its azimuth location or position,  $x_q(nT)$ . The time-varying Doppler frequency can be expressed as a function of the patch location in elevation and azimuth angles as defined in Figure 3.1. Substituting the expression,

$$x_q(nT) / r = \cos \theta_q(nT) \sin \varphi_q(nT), \quad (3.48)$$

into (3.47) yields an expression for the Doppler frequency associated with the clutter patch at elevation angle  $\theta_q(nT)$  and azimuth angle  $\varphi_q(nT)$ :

$$f_{D_q}(nT) \cong 2V_p \cos \theta_q(nT) \sin \varphi_q(nT) / \lambda_c. \quad (3.49)$$

This relationship between Doppler and AOA positions the clutter energy from all  $Q$  clutter patches along a ridge on an angle-Doppler map as shown in Figure 3.8.

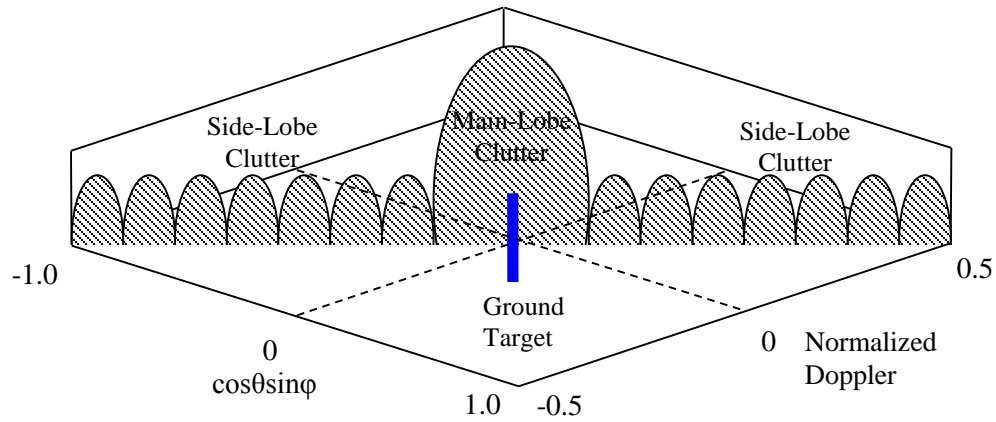


Figure 3.8. Angle-Doppler clutter structure.

The slope of the angle-Doppler clutter ridge is calculated from (3.49) as  $2V_p / \lambda_c$ .

In terms of normalized Doppler, the slope of the ridge is equal to  $2V_p T / \lambda_c$ .

A target moving with velocity in the radial direction either towards or away from the platform occupies a different position on the angle-Doppler map than the clutter. In side-looking, multichannel airborne radar, simultaneous spatial filtering in AOA and temporal filtering in Doppler suppresses the clutter signal along the narrow ridge, which improves detection of low-radial velocity targets over single-channel methods that filter only in Doppler.

The received signal in (3.43) from all  $Q$  clutter patches can be organized into a data matrix,

$$\mathbf{X}_c = \begin{bmatrix} x_{c_{0,0}} & x_{c_{0,1}} & x_{c_{0,2}} & \cdots & x_{c_{0,N-1}} \\ x_{c_{1,0}} & x_{c_{1,1}} & x_{c_{1,2}} & \cdots & x_{c_{1,N-1}} \\ \vdots & \vdots & \vdots & & \vdots \\ x_{c_{M-1,0}} & x_{c_{M-1,1}} & x_{c_{M-1,2}} & \cdots & x_{c_{M-1,N-1}} \end{bmatrix}, \quad (3.50)$$

where each entry is equal to the combined signal from all  $Q$  clutter patches for a particular channel and pulse. The columns represent the received clutter signal at each of the  $M$  spatial channels for a particular pulse return, and the rows represent the received slow-time clutter signal for a particular channel. Stacking the columns of data yields the space-time clutter vector,  $\mathbf{x}_c$ .

The clutter covariance matrix for a particular range is defined as

$$\mathbf{R}_c = E[\mathbf{x}_c \mathbf{x}_c^H] = \sigma_n^2 \sum_{q=1}^Q \xi_q \mathbf{x}_q \mathbf{x}_q^H, \quad (3.51)$$

where  $\mathbf{x}_q$  is the  $MN$ -sample phase portion of the clutter signal from the  $q^{\text{th}}$  patch.

### 3.4 Noise Model

A potential target competes with noise in addition to ground clutter. The noise is assumed to be internally generated white Gaussian receiver noise with zero mean and noise power,  $\sigma_n^2$ . The noise covariance matrix for a particular range is defined as

$$\mathbf{R}_n = E[\mathbf{x}_n \mathbf{x}_n^H] = \sigma_n^2 \mathbf{I}_{MN}, \quad (3.52)$$

where  $\mathbf{x}_n$  is the noise component of the data and  $\mathbf{I}_{MN}$  is the  $MN \times MN$  identity matrix [4].

### 3.5 Target Doppler Spread

The nonlinear phase terms in the temporal signal spread energy into different Doppler bins as dwell time is extended. The instantaneous frequency in hertz attributable to the various components as a function of time is equal to the time derivative of the nonlinear phase components from Table 3.1 divided by  $2\pi$ . These expressions for time-varying instantaneous frequency are given in Table 3.3.

Table 3.3. Instantaneous frequency of nonlinear phase components.

<i>Phase Order</i>	<i>Instantaneous Frequency</i>
$2^{nd}$	$f_2(nT) \cong \left( \frac{-2}{\lambda_c r} \right) (A_x(x_1 + V_p(N/2)T) + A_y(y_1 + y_0) + V_x^2 + V_y^2 - 2V_x V_p)(nT)$
$3^{rd}$	$f_3(nT) \cong \left( \frac{-1}{\lambda_c r} \right) (3A_x(V_x - V_p) + 3A_y V_y + J_x(x_1 + V_p(N/2)T) + J_y(y_1 + y_0))(nT)^2$
$4^{th}$	$f_4(nT) \cong \left( \frac{-1}{3\lambda_c r} \right) (3A_x^2 + 3A_y^2 + 4J_x(V_x - V_p) + 4J_y V_y)(nT)^3$
$5^{th}$	$f_5(nT) \cong \left( \frac{-5}{6\lambda_c r} \right) (J_x A_x + J_y A_y)(nT)^4$
$6^{th}$	$f_6(nT) \cong \left( \frac{-1}{6\lambda_c r} \right) (J_x^2 + J_y^2)(nT)^5$

The time-varying frequency expressions in Table 3.3 can be used to determine the frequency spreading of the target signal for any set of radar and target parameters of interest. The Doppler spreading calculated from the time-varying frequency expressions in Table 3.3 for the  $2^{nd}$ ,  $3^{rd}$ , and  $4^{th}$  order phase components is given in Table 3.4 for one and two-second dwells and for the radar and maximum target parameters in Table 3.2. These maximum target parameters cause the maximum Doppler spread over an extended dwell.

Table 3.4. Maximum Doppler spread for dwell times of one and two seconds.

<i>Phase Component</i>	<i>Time</i>	<i>Frequency Spread</i>
$2^{nd}$	1 s	77.5 Hz
	2 s	155.5 Hz
$3^{rd}$	1 s	17.1 Hz
	2 s	68.8 Hz
$4^{th}$	1 s	0.1 Hz
	2 s	1.2 Hz

The quadratic phase component causes the Doppler frequency to either increase or decrease linearly with time, depending primarily on the direction of radial acceleration. The cubic phase term causes the Doppler frequency to either increase or decrease as a quadratic function of time, depending on the sign of the cubic phase component. The cubic phase term increases or decreases the rate of change in Doppler frequency, depending on the sign of the cubic phase component in relation to the sign of the quadratic phase component. Spreading from the  $5^{th}$  and  $6^{th}$  order phase components is negligible for these dwells. For low radial velocity targets, signal energy can spread into the angle-Doppler space occupied by the mainlobe clutter as shown in Figure 3.9.



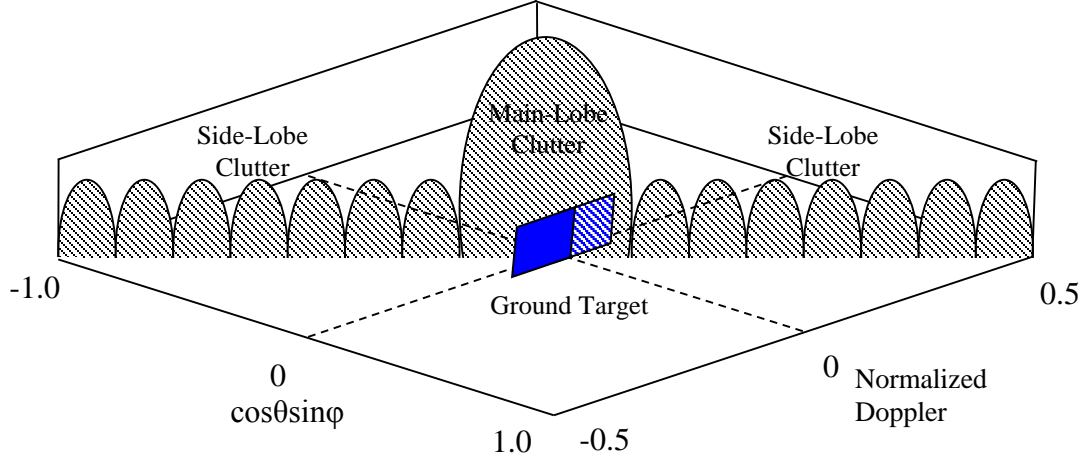


Figure 3.9. Spread of target signal energy into mainlobe clutter region.

The bandwidth of the clutter is approximately  $2V_p\theta_{3\text{dB}}/\lambda_c$  for the side looking case, where  $\theta_{3\text{dB}}$  is the 3 dB beamwidth of the antenna [51]. The antenna beamwidth is approximately equal to  $\lambda_c/L$ , where  $L$  is the length of the ULA. Thus, the approximate clutter bandwidth is given by  $2V_p/L$ .

Targets whose energy lies outside the mainlobe clutter Doppler spread are referred to as exo-clutter targets. Those whose energy lies inside the mainlobe clutter Doppler spread are endo-clutter targets. Because of the spread in Doppler over an extended dwell time, signal energy may lie in both regions. Target detection is limited to exo-targets whose energy is primarily in the Doppler region not occupied by clutter, unless processing methods can compensate for the loss of signal energy that falls in the clutter region for target signals that spread over both exo- and endo-clutter regions.

## CHAPTER 4

### A MULTISTAGE ALGORITHM FOR SINGLE-CHANNEL EXTENDED DWELL TARGET DETECTION

The signal model for a moving target must include multiple order phase terms when dwell time is extended beyond the typical short dwell used in Fourier-based processing. Analysis of the signal's nonlinear phase components forms the basis for an algorithm that generates an accurate multiphase signal model for the extended dwell time target signal. Rather than searching for the optimal detector in a filter bank that includes all combinations of phase components, a more efficient method is presented that estimates the various signal phase components sequentially in a multistage process. Inner products are used to identify the best-matched phase components from small, single-phase-component dictionaries. The signal components are combined to form the signal model used in the filter for target detection. Performance is evaluated for both noise-limited and clutter-limited environments.

Output SINR is the primary performance metric used to characterize the algorithm. Clairvoyant clutter mitigation techniques are used with the full covariance matrix; thus the output SINR is given by the product of optimal SNR and two loss factors,  $L_1$  and  $L_4$ , as defined in chapter 2:

$$SINR_{output} = SINR_{opt} L_1 L_4, \quad (4.1)$$

where  $L_1$  is the clairvoyant loss,  $SINR_{opt} / SINR_{opt}$ , and  $L_4$  is the loss from suboptimal signal modeling,  $SINR_{sub} / SINR_{opt}$ .

Evaluation of initial radial velocity for both accelerating and decelerating targets over an extended dwell time is a more relevant figure of merit than MDV since the radial

velocity of the extended dwell signal often changes over the dwell. Performance at various initial radial velocities for both accelerating and decelerating targets is used in addition to output SINR to characterize algorithm performance in clutter.

#### 4.1 Nonlinear Phase Analysis

The various nonlinear phase components become significant in the target signal at different times during an extended dwell. The time at which a nonlinear phase component equals reaches approximately  $\pm\pi/2$  radians is the suggested dwell time for inclusion in the signal model [41]. If the component is not included in the model, destructive interference reduces output SNR beginning at this point in the dwell. This concept is shown in Figure 4.1 for a signal generated with radar and target parameters from Table 3.2 and modeled first with a linear phase component only and then with linear and quadratic phase components. Performance is compared to optimal processing, the clairvoyant case when the target signal model exactly matches the true signal.

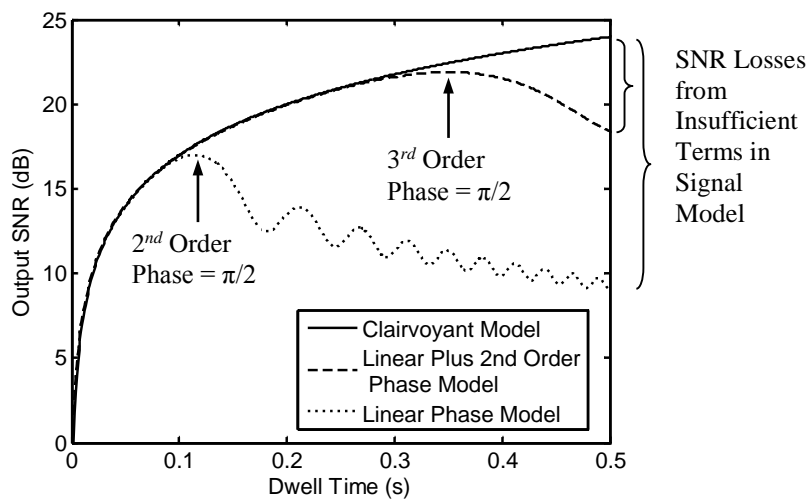


Figure 4.1. Output SNR for linear-phase model, linear-plus-second-order-phase model, and clairvoyant model [41].

The dwell time at which the various nonlinear phase effects appear in the target signal depends on known radar parameters and unknown target parameters.

Recommended dwell times for including the various nonlinear phase components in the signal model are determined by setting the absolute values of the nonlinear phase expressions in Table 3.1 equal to  $\pi/2$ , inserting the radar parameters and target parameters of interest into the expressions, and solving for  $nT$ . Maximum values in any range of potential target parameters cause the nonlinear phase components to appear earlier in the dwell than lesser values. Since target motion is unknown a priori, the maximum values establish the times at which the phase components can be expected to appear in the signal.

Table 4.1 lists typical parameters used throughout the rest of chapter 4 to illustrate concepts and demonstrate algorithm performance. Initial target position is scene center.

Table 4.1. Radar and target parameters for algorithm development.

<i>Parameter</i>	<i>Magnitude</i>
Center frequency, $f_c$	10 GHz
Platform velocity, $V_p$	100 m/s
Platform height, $h$	3 km
Slant range, $r$	20 km
Target radial and tangential velocity, $V_y$ and $V_x$	1.0 – 15.0 m/s
Target radial and tangential acceleration, $A_y$ and $A_x$	0.1 – 1.0 m/s <sup>2</sup>
Target radial and tangential jerk, $J_y$ and $J_x$	0.1 – 0.5 m/s <sup>3</sup>

Inserting the radar parameters and maximum target parameters in Table 4.1 into the expressions in Table 3.1 determines typical dwell times at which the nonlinear phase components become significant. These calculated dwell times are listed in Table 4.2. The decorrelation times shown in Figure 4.1 confirm the calculated dwell times in Table 4.2 for the 2<sup>nd</sup> and 3<sup>rd</sup> order phase terms.

Table 4.2. Typical dwell times at which nonlinear phase effects appear (target parameter dependent).

<i>Phase Order</i>	<i>Dwell Time</i>
$2^{nd}$	100 – 170 ms
$3^{rd}$	360 – 620 ms
$4^{th}$	1.9 – 2.6 s
$5^{th}$	3.9 – 6.8 s
$6^{th}$	4.7 – 8.0 s

## 4.2 Multistage, Dictionary-Based Matching Algorithm

### 4.2.1 Algorithm Development

Instead of using a single, intractably large filter bank that includes all combinations of phase components, a method is presented for estimating the components in multiple stages with smaller filter banks, or dictionaries, comprised of specific phase-order waveforms. The dwell times at which the various nonlinear signal components emerge in the signal form the basis for an algorithm that generates a multiphase signal model in multiple stages.

The linear phase component is dominant in the signal until the quadratic phase effects appear. If the linear phase component is extracted from the signal, the quadratic phase component is dominant until the cubic phase effects appear. In general, if all lower order phase components are removed from the signal, a nonlinear phase component is considered dominant until the next higher order phase effects appear. The dominant dwell intervals for each phase component and corresponding numbers of samples in each interval are listed for the general case in Table 4.3 where  $D_i$  represents the dwell time at which the magnitude of the  $i^{th}$  order phase component equals  $\pi/2$  for radar parameters and maximum target parameters under consideration.

Table 4.3. General case: dominant dwell intervals and corresponding number of samples in each interval.

<i>Phase Order</i>	<i>Dominant Dwell Interval</i>	<i>Number of Samples in Interval</i>
1 <sup>st</sup>	$I_1 = 0 \text{ to } D_2$	$N_1 = (I_1)(\text{PRF})$
2 <sup>nd</sup>	$I_2 = 0 \text{ to } D_3$	$N_2 = (I_2)(\text{PRF})$
3 <sup>rd</sup>	$I_3 = 0 \text{ to } D_4$	$N_3 = (I_3)(\text{PRF})$
4 <sup>th</sup>	$I_4 = 0 \text{ to } D_5$	$N_4 = (I_4)(\text{PRF})$
5 <sup>th</sup>	$I_5 = 0 \text{ to } D_6$	$N_5 = (I_5)(\text{PRF})$
6 <sup>th</sup>	entire dwell	$N_6 = N$

The dwell times in Table 4.2 establish dominant dwell intervals for the typical set of radar and target parameters given in Table 4.1. These parameter-specific intervals and the corresponding number of samples in each interval are summarized in Table 4.4.

Table 4.4. Typical case: dominant dwell intervals and corresponding number of samples in each interval.

<i>Phase Order</i>	<i>Dominant Dwell Interval</i>	<i>Number of Samples in Interval</i>
1 <sup>st</sup>	0 to 100 ms	$N_1 = (0.10 \text{ s})(\text{PRF})$
2 <sup>nd</sup>	0 to 360 ms	$N_2 = (0.36 \text{ s})(\text{PRF})$
3 <sup>rd</sup>	0 to 1.9 s	$N_3 = (1.9 \text{ s})(\text{PRF})$
4 <sup>th</sup>	0 to 3.9 s	$N_4 = (3.9 \text{ s})(\text{PRF})$
5 <sup>th</sup>	0 to 4.7 s	$N_5 = (4.7 \text{ s})(\text{PRF})$
6 <sup>th</sup>	entire dwell	$N_6 = N$

The dominant dwell intervals are used to sequentially determine the various phase components that comprise the extended-dwell signal.

If the desired dwell time for algorithm implementation is between dominant intervals for two different phase components, the ideal signal model includes the higher of the two components in addition to all lower phase terms. The highest phase term used to model the signal is estimated using all  $N$  samples in the CPI.

An initial approach detailed in [41] estimates each signal component individually by finding the waveform in a phase-specific dictionary that maximizes the inner product with the data over the dominant dwell interval of each phase component. After each phase component is determined, it is extracted from the data through a complex phase multiplication that reveals the next higher order phase component. This approach works well for a target with parameters in the mid-range of those listed in Table 4.1 and for dwell times up to 500 ms. A significant extension of this approach is presented herein to improve performance for targets with parameters at the upper end of the ranges listed in Table 4.1, which are the most challenging to model correctly, and for dwell times exceeding 500 ms.

As previously mentioned, over the dominant dwell interval of each phase component, the next higher order phase component contributes a maximum phase of  $\pm \pi/2$  radians to the signal. This extra phase affects which dictionary waveform is the best match to the data. Figure 4.2 shows how the quadratic phase contribution of  $\pi/2$  radians to the received signal for the time interval in which the linear-phase waveform is dominant shifts the perceived Doppler and results in an incorrect linear phase estimate.

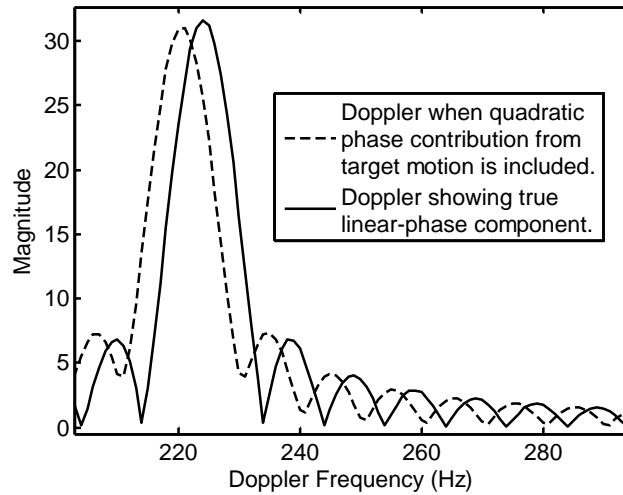


Figure 4.2. Doppler showing true linear phase component of target signal, and Doppler of target signal when quadratic-phase contribution is included over a 100 ms dwell.

Each nonlinear phase component affects the dictionary selection of the next lower order waveform in a similar way. When the signal components are determined individually as in [41], the slight mismatch between the selected dictionary waveform and the true signal phase component can result in small accumulated phase errors and potential SNR loss as dwell time increases. A modification to the approach described in [41], called the multistage algorithm, minimizes the impact of higher order phase terms on dictionary waveform selection by determining combinations of best-matched waveforms from two different dictionaries at each stage of the algorithm.

The multistage algorithm begins by estimating the linear phase component. The waveform from the linear-phase dictionary that maximizes the inner product with the first  $N_1$  samples of the data is the best-matched linear-phase waveform. To account for the potential Doppler shift due to the quadratic phase presence, the best-matched linear-phase waveform and several adjacent waveforms from the linear-phase dictionary are combined with each waveform in the quadratic-phase dictionary on a pulse-by-pulse basis. The best-matched waveform from this combined dictionary maximizes the inner product with the first  $N_2$  samples of the data. The linear phase component from this best combination is removed from the data to reveal the higher order phase terms and is later used in the signal model. The quadratic phase component from this best combination plus several adjacent waveforms from the quadratic-phase dictionary are then combined with each of the waveforms in the cubic-phase dictionary on a pulse-by-pulse basis to determine the optimal combination of quadratic and cubic phase components through inner products. This process of simultaneously determining the best combination of two signal components reduces the effects of the higher order phase terms on the various phase components selected from the



dictionaries. Figure 4.3 is a diagram of the multistage algorithm showing the sequential estimation of phase components. In the diagram, the asterisk on a signal component indicates the particular phase component that is ultimately used in the signal model.

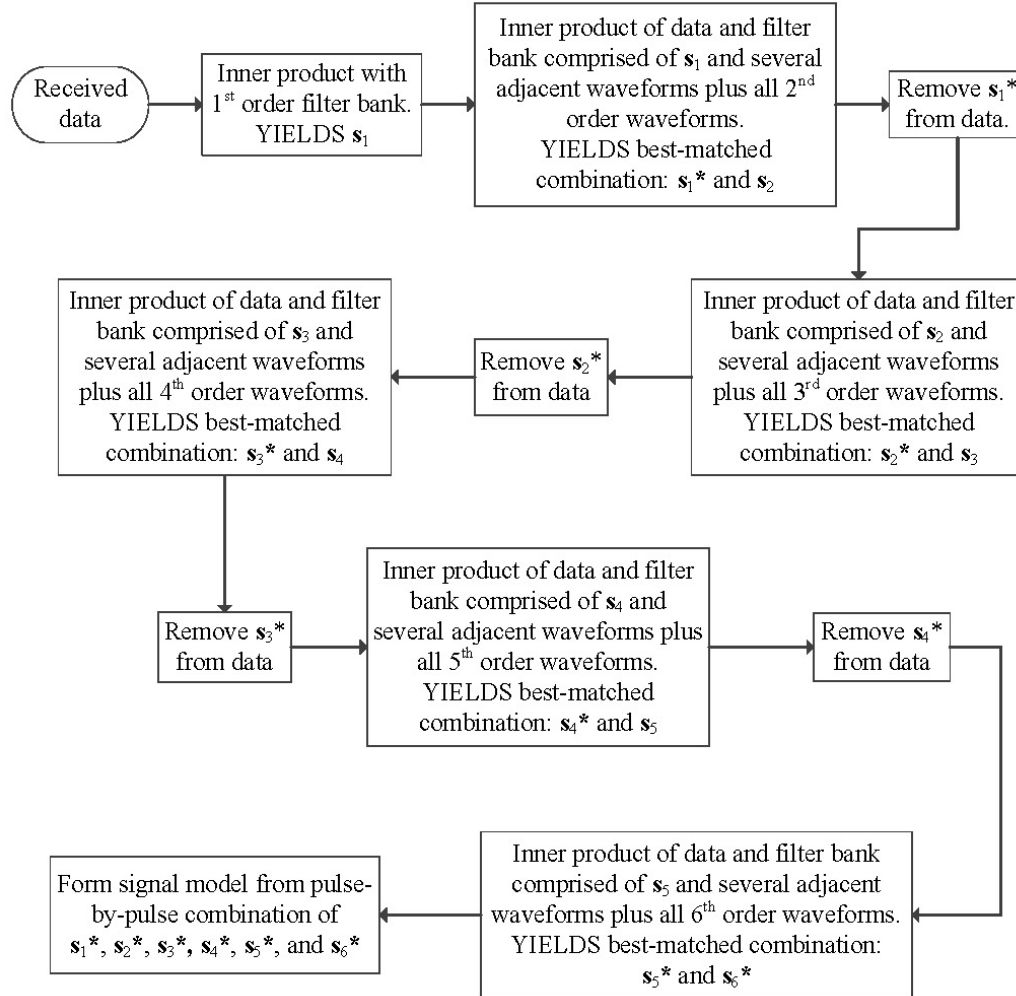


Figure 4.3. Flow diagram of multistage algorithm.

Though the diagram shows the process of estimating six phase components, fewer components are typically needed in the signal model. The process is finished when the final component desired in the signal model is estimated.

Each inner product operation which determines the best-matched combination of

two different phase components is performed over the dominant dwell interval of the higher order phase component. The signal model, formed by multiplying the  $N$ -sample individual phase components together on a pulse-by-pulse basis, is used as the filter for target detection in the noise-limited case.

The number of adjacent waveforms that are combined with the next higher order phase dictionary at each stage of the algorithm depends on the magnitude of the shift caused by the higher order phase component. For an  $i^{th}$  order phase dictionary,

$$\mathbf{D}_i = [\exp(j\pi\varphi_{i,1}(\mathbf{n}T)^i) \quad \exp(j\pi\varphi_{i,2}(\mathbf{n}T)^i) \quad \dots \quad ] \quad (4.2)$$

the maximum contribution of  $\pm \pi/2$  radians from the  $(i + 1)^{th}$  order phase component causes the best-matched value of  $\varphi_i$  to be shifted from its true value by  $\Delta\varphi_i = (\pm \pi / 2) / (\pi(N_iT)^i)$  over  $N_i$  samples. The generic values for  $N_i$  in Table 4.3 can be used to determine  $\Delta\varphi_i$  for any set of radar and target parameters. The typical values for  $N_i$  in Table 4.4 can be used to determine typical maximum shifts from each true signal phase component. These values for  $\Delta\varphi_i$  are given in Table 4.5.

Table 4.5. Typical maximum shift from true signal component due to phase contribution from next higher phase component.

<i>Phase Order</i>	<i>Waveform</i>	$\Delta\varphi_i$
$1^{st}$	$\exp(j\pi\varphi_1(nT))$	$\Delta\varphi_1 \cong \pm 5/s$
$2^{nd}$	$\exp(j\pi\varphi_2(nT)^2)$	$\Delta\varphi_2 \cong \pm 4/s^2$
$3^{rd}$	$\exp(j\pi\varphi_3(nT)^3)$	$\Delta\varphi_3 \cong \pm 0.1/s^3$
$4^{th}$	$\exp(j\pi\varphi_4(nT)^4)$	$\Delta\varphi_4 \cong \pm 0.003/s^4$
$5^{th}$	$\exp(j\pi\varphi_5(nT)^5)$	$\Delta\varphi_5 \cong \pm 0.0003/s^5$

The best-matched waveform from each dictionary plus adjacent waveforms that span the range of possible values for  $\Delta\varphi_i$  are combined with each waveform in the next

higher order phase dictionary on a pulse-by-pulse basis to determine the optimal combination of the two phase components. The actual number of adjacent waveforms is equal to  $\Delta\phi_i$  divided by the dictionary resolution of the  $i^{th}$  phase component.

#### 4.2.2 SNR Limitations

The linear phase component is dominant for the shortest dwell time of the signal components. This means the linear phase component is determined with the fewest number of samples of any component, and its estimate is most negatively affected by high noise levels. For low single-sample SNR targets, the likelihood of selecting the correct waveform from the linear-phase dictionary decreases as single-sample SNR decreases. Table 4.6 gives percentage of correctly chosen linear-phase waveforms for different single-sample SNRs, a PRF of 1000 samples/s, and maximum target parameters listed in Table 4.1.

Table 4.6. Percent of correctly chosen linear-phase waveforms in 1000 trials for various SNRs.

<i>Single-Sample SNR</i>	<i>Percentage Correct</i>
– 9 dB	97.0 %
– 10 dB	92.1 %
– 11 dB	83.3 %
– 12 dB	71.9 %
– 13 dB	59.5 %

#### 4.2.3 Algorithm Limitations in the Presence of Clutter

At a particular range of interest, the clutter signal is comprised of multiple linear phase contributions from the various clutter patches. These linear phase components compete with the target signal in the first stage of the multistage algorithm when the best-matched linear-phase waveform is determined. If clutter is not mitigated, the linear phase

components clustered around the mainlobe clutter Doppler region obscure the target signal, especially for low single-sample SINR, and cause an incorrect waveform to be chosen from the linear-phase dictionary. Clutter mitigation techniques were developed to enable the algorithm to perform well in strong clutter environments.

#### 4.2.4 Clutter Mitigation

The optimal detector in a clutter-limited environment is  $\mathbf{w} = \mathbf{R}_I^{-1}\mathbf{s}$ , where  $\mathbf{R}_I$  is the temporal-only interference covariance matrix and  $\mathbf{s}$  is the target signal. In this simulation, interference is known a priori, and the clairvoyant  $\mathbf{R}_I$  provides an upper bound for algorithm performance in clutter.

In the multistage algorithm, the signal components that comprise  $\mathbf{s}$  are estimated separately. The optimal detector for each phase component,  $\mathbf{w}_i = \mathbf{R}_I^{-1}\mathbf{s}_i$ , is estimated by applying a whitening filter,  $\mathbf{R}_I^{-1/2}$ , to the data and to each phase-specific dictionary. Application of the whitening filter to the slow-time data,  $\mathbf{x}$ , comprised of noise, clutter, and the target signal creates a new signal,  $\tilde{\mathbf{x}} = \mathbf{R}_I^{-1/2}\mathbf{x}$ . The whitened data in the  $i^{th}$  stage of the algorithm when the  $i^{th}$  order phase component is dominant in the signal is  $\tilde{\mathbf{x}}_i = \mathbf{R}_I^{-1/2}\mathbf{x}_i$ . Application of the whitening filter to a dictionary comprised of  $i^{th}$  order phase components creates a whitened dictionary,  $\tilde{\mathbf{D}}_i = \mathbf{R}_I^{-1/2}\mathbf{D}_i$ . The waveform,  $\tilde{\mathbf{s}}_i = \mathbf{R}_I^{-1/2}\mathbf{s}_i$ , in  $\tilde{\mathbf{D}}_i$  that is the best match to  $\tilde{\mathbf{x}}_i$  maximizes the output of  $(\tilde{\mathbf{D}}_i)^H \tilde{\mathbf{x}}_i$ . The output of  $(\tilde{\mathbf{s}}_i)^H \tilde{\mathbf{x}}_i$  is equal to the scalar output that results from applying the optimal detector,  $\mathbf{w}_i$ , to the input data,  $\mathbf{x}_i$ :

$$(\tilde{\mathbf{s}}_i)^H \tilde{\mathbf{x}}_i = (\mathbf{R}_I^{-1/2}\mathbf{s}_i)^H (\mathbf{R}_I^{-1/2}\mathbf{x}_i) = (\mathbf{R}_I^{-1}\mathbf{s}_i)^H \mathbf{x}_i = \mathbf{w}_i^H \mathbf{x}_i. \quad (4.3)$$

Signal components are removed from the whitened data through a phase multiplication that reveals higher order phase components. The waveform,  $\mathbf{s}_i$ , that is used

in the signal model occupies the same position in  $\mathbf{D}_i$  as  $\tilde{\mathbf{s}}_i$  occupies in  $\tilde{\mathbf{D}}_i$ .

### 4.3 Performance Characterization

Unless otherwise indicated, single-sample SNR is  $-10$  dB for algorithm evaluation.

#### 4.3.1 Noise-Limited Environment, 500 ms Dwell Time

The signal model generated with the multistage dictionary-based matching algorithm was evaluated for a target with maximum motion parameters from Table 4.1 in a noise-limited environment over a 500 ms dwell time. Typical output SNR as a function of pulse number for a PRF of 1000 samples/s is shown in Figure 4.4 for the clairvoyant model, the multistage algorithm model, and the linear-phase model. The multistage algorithm model includes 1<sup>st</sup>, 2<sup>nd</sup>, and 3<sup>rd</sup> order phase components for a 500 ms dwell.

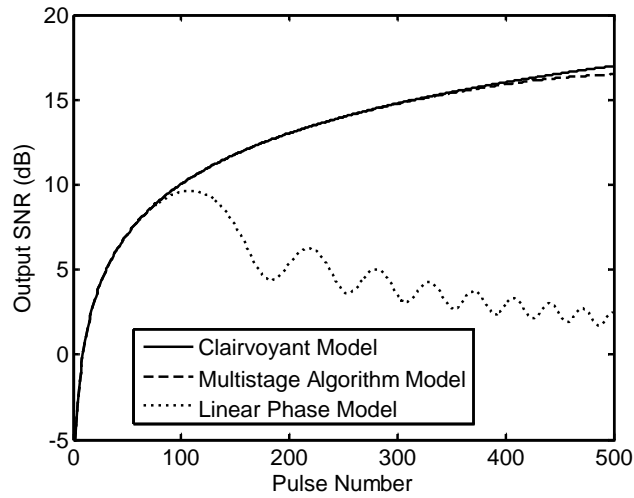


Figure 4.4. Output SNR for the clairvoyant signal model, the multistage algorithm model, and the linear-phase model as a function of pulse number over a 500 ms dwell.

The multistage algorithm generates a near optimal signal model over a 500 ms dwell for all target parameters listed in Table 4.1.

### 4.3.2 Clutter-Limited Environment

Clutter mitigation suppresses signal energy in the frequency region occupied by the clutter signal. The multistage algorithm requires adequate signal energy to estimate a signal model. In the frequency region occupied by the clutter signal, especially for a weak target signal in a strong clutter environment, the algorithm is unable to determine the various signal components for an accurate estimate. The initial radial velocity component of target motion primarily determines where the signal energy is positioned in Doppler. The magnitude and direction of the spread of signal energy over a long dwell is determined by the other target parameters, primarily the radial acceleration. Figure 4.5 shows algorithm performance in terms of loss in output SINR as compared to optimal SNR for target velocities from  $-7.5$  m/s to  $7.5$  m/s for a single-sample SNR of  $-8$  dB, a single-sample SCR of  $-20$  dB, and for dwells of 500 ms and one second. Output SINR was averaged over twenty trials to reduce the random effects of the noise and maximum values were used for all target parameters other than radial velocity. In this illustration, side-looking radar places the clutter signal in the low Doppler region.

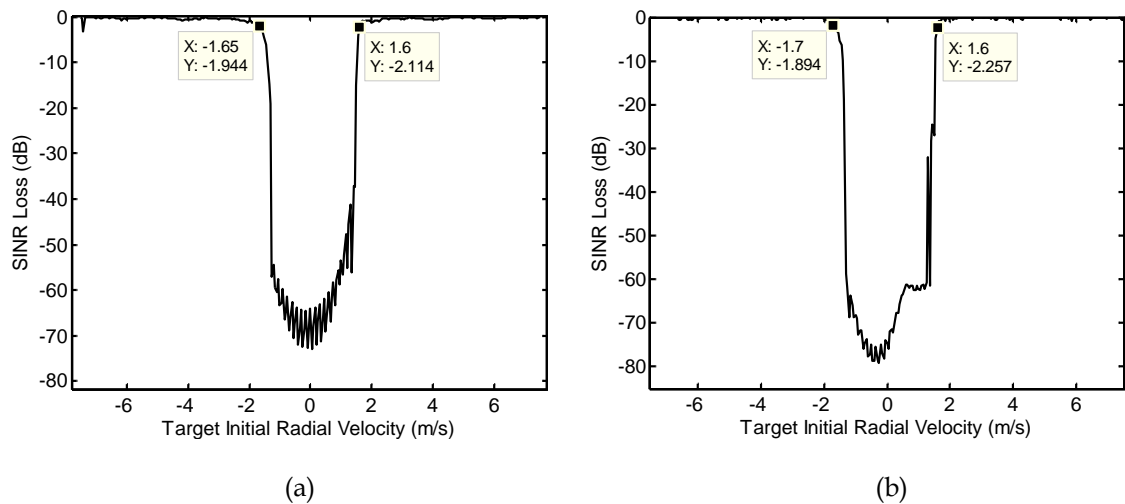


Figure 4.5. Output SINR loss in relation to optimal SNR as a function of initial radial velocity for a single-sample SNR of  $-8$  dB, a single-sample SCR of  $-20$  dB, and dwells of (a) 500 ms and (b) 1.0 s.

The effects of radial acceleration on algorithm performance can be seen in Figures 4.5(a) and (b). In the example shown, a positive component of radial acceleration causes the radial velocity to become more positive, or equivalently, less negative. For a target with an initial negative radial velocity on the edge of the mainlobe clutter Doppler region, a positive radial acceleration component decelerates the target. This deceleration spreads signal energy into the clutter Doppler region and degrades performance. For a target with an initial positive radial velocity, the same positive radial acceleration component accelerates the target, which causes the signal energy to spread away from the null region. A negative radial acceleration component would switch the left and right sides of Figures 4.5(a) and (b). The spread of signal energy into the mainlobe clutter Doppler region for a decelerating target increases at longer dwells. The tangential velocity and radial jerk components of target motion contribute minimally to energy spreading as compared to the radial acceleration component for dwells of one second or less. A summary of algorithm performance for the different target types and dwell times, based on the results shown in Figure 4.5, is given in Table 4.7.

Table 4.7. Minimum detectable initial radial velocity for various target types in strong clutter.

<i>Target Type</i>	<i>Dwell Time</i>	<i>Minimum Detectable Initial Radial Velocity</i>
Accelerating	500 ms	1.60 m/s
	1.0 s	1.60 m/s
Decelerating	500 ms	1.65 m/s
	1.0 s	1.70 m/s

The minimum detectable initial radial velocity is lower for accelerating targets than for decelerating targets. As dwell time increases, the spread of signal energy into the

mainlobe clutter Doppler region becomes increasingly detrimental to detection of decelerating targets with low initial radial velocity.

The multistage algorithm was evaluated for a target with a single-sample SCR of  $-20$  dB whose signal energy is in the exo-clutter region over the entire dwell. Output SINR as a function of pulse number for the clairvoyant signal model, the multistage algorithm model, and the linear-phase model are shown in Figure 4.6 for maximum target parameters from Table 4.1.

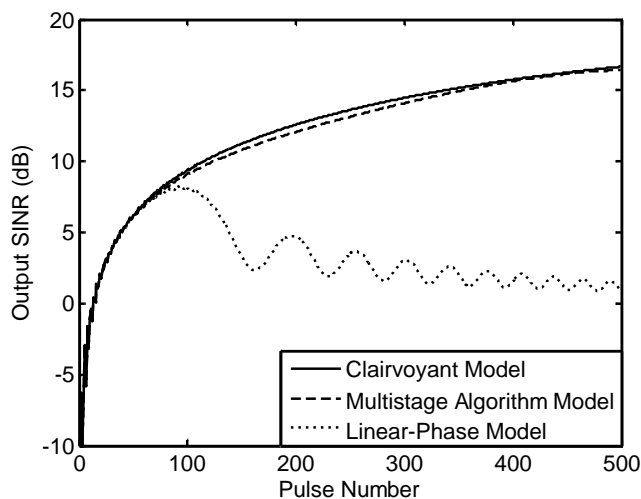


Figure 4.6. Output SINR for the clairvoyant signal model, the multistage algorithm model, and the linear-phase model as a function of pulse number for an exo-clutter target with a single-sample SCR of  $-20$  dB.

Performance of the multistage algorithm approaches optimal processing, the upper bound of performance, for an exo-clutter target with a single-sample SCR of  $-20$  dB and a single-sample SNR of  $-10$  dB. Output SINR levels for the exo-clutter target are comparable to the output SNR levels shown in Figure 4.4 for the noise-limited scenario.



### 4.3.3 Noise-Limited Environment, Dwell Times Exceeding 500 ms

Required detection levels for output SNR are typically achieved with a dwell time of 500 ms; however, higher output SNR may be desirable for applications such as tracking or target identification, or longer dwell times may be required for imaging a ground scene. The multistage algorithm may be applied to data collected over dwell times exceeding 500 ms to provide adequate output SNR for these applications.

Output SNR for the multistage algorithm model is shown for the noise-limited case in Figure 4.7 for dwells ranging from 500 ms to four seconds in 500 ms increments. Fifty measured values of output SNR were averaged for the multistage algorithm model and were compared with the maximum output SNR for the multistage algorithm model and optimal SNR at each dwell time.

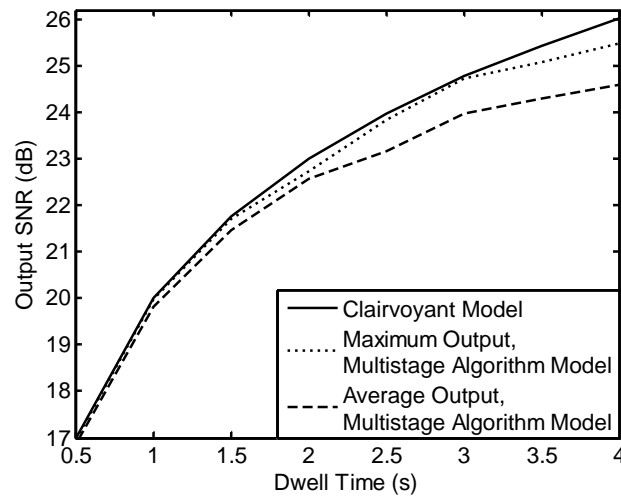


Figure 4.7. Output SNR for dwell times up to four seconds for the multistage algorithm model and the clairvoyant model.

The maximum output SNR for the multistage algorithm model over fifty trials likely represents the best combination of waveforms from each dictionary. Thus, the

differences between the maximum values achieved with the multistage algorithm model and the optimal output SNR achieved with the clairvoyant model are primarily due to modeling the various signal components with finite dictionaries.

The averaged values include some outliers caused by an incorrect dictionary match of at least one of the waveforms used to represent the signal, likely due to the strong noise presence. Thus, as single-sample SNR increases, algorithm performance approaches the maximum output levels.

The assumptions made in modeling the target as a point source may not be accurate in some situations as dwell time is extended up to four seconds. The range to the target, center frequency, and target size affect whether the target can be modeled as a point source or whether the change in RCS over the dwell must be considered [23]. Signal energy is confined to a single range cell for the results shown in Figure 4.7. For at least the upper end of the dwell times included in Figure 4.7, migration of target signal energy through multiple range cells is possible. Practical implementation must include efforts to confine signal energy to a single range cell at dwell times for which target movement exceeds range cell extent.

#### **4.4 Error Analysis and Modeling Losses**

Dictionaries comprised of a finite number of waveforms cannot provide exact representations of the various phase components of the signal. A phase error is introduced into the model when a signal component is not an exact match to the closest waveform in the dictionary. Assuming the error from approximating the range expression in (3.16) with a polynomial is minimal, and the true target signal can be nearly optimally represented by a combination of multiple phase waveforms, output SNR loss is compared to optimal

processing, in the noise-limited case, to determine the effects of dictionary resolution on performance.

Analysis of the phase error and corresponding reduction in SNR begins with the expression for output SNR [4]:

$$SNR = \frac{\sigma_s^2 |\mathbf{w}^H \mathbf{s}|^2}{N \sigma_n^2}, \quad (4.4)$$

where  $\sigma_s^2$  is the single-pulse target signal power,  $\sigma_n^2$  is the noise power,  $\mathbf{w}$  is the weight vector applied to the data, and  $\mathbf{s}$  is the true target signal phase. Optimal SNR,

$$SNR_{opt} = \frac{N \sigma_s^2}{\sigma_n^2}, \quad (4.5)$$

is achieved when  $\mathbf{w}$  is exactly matched to the target signal phase,  $\mathbf{s} = \exp(j\boldsymbol{\varphi})$ . When  $\mathbf{w}$  is mismatched to  $\mathbf{s}$  due to a phase error,  $\boldsymbol{\varepsilon}$ , the suboptimal weight vector is  $\mathbf{w} = \exp(j(\boldsymbol{\varphi} + \boldsymbol{\varepsilon}))$ , and the corresponding suboptimal output SNR is

$$SNR_{sub} = \frac{\sigma_s^2 |\exp(j(\boldsymbol{\varphi} + \boldsymbol{\varepsilon}))^H \exp(j\boldsymbol{\varphi})|^2}{N \sigma_n^2}. \quad (4.6)$$

SNR loss, the ratio of suboptimal SNR to optimal SNR, is

$$SNR_{LOSS} = \frac{SNR_{sub}}{SNR_{opt}} = \frac{|\exp(j(\boldsymbol{\varphi} + \boldsymbol{\varepsilon}))^H \exp(j\boldsymbol{\varphi})|^2}{N^2} = \frac{\left| \sum_{n=0}^{N-1} \exp(-j\varepsilon_n) \right|^2}{N^2} \leq 1, \quad (4.7)$$

where  $\boldsymbol{\varepsilon}$  represents the phase error in vector form and  $\varepsilon_n$  represents the phase error as a function of pulse number. Eqn. (4.7) is equivalent to the loss factor,  $L_4$ , described in chapter 2 for the noise-limited case.

The true signal phase,  $\mathbf{s}$ , is represented by a combination of multiple phase waveforms. For the example of dwell times ranging from 500 ms to four seconds presented

in this paper, the signal can be represented by up to five phase orders depending on the dwell time:

$$\mathbf{s} = \exp(j2\pi f_D \mathbf{n}T) \odot \exp(j\pi\varphi_2(\mathbf{n}T)^2) \odot \dots \odot \exp(j\pi\varphi_5(\mathbf{n}T)^5). \quad (4.8)$$

The weight vector or signal model,  $\mathbf{w}$ , determined by the multistage algorithm is ideally a composite of the best-matched waveforms from the various dictionaries, each of which includes a possible dictionary resolution error. For the four-second dwell time example,

$$\begin{aligned} \mathbf{w} &= \mathbf{s}_{1,final} \odot \mathbf{s}_{2,final} \odot \mathbf{s}_{3,final} \odot \mathbf{s}_{4,final} \odot \mathbf{s}_5 \\ &= \exp(j2\pi(f_D + \Delta f_D)\mathbf{n}T) \odot \exp(j\pi(\varphi_2 + \Delta\varphi_2)(\mathbf{n}T)^2) \odot \dots \odot \exp(j\pi(\varphi_5 + \Delta\varphi_5)(\mathbf{n}T)^5). \end{aligned} \quad (4.9)$$

The maximum dictionary resolution error occurs when the true signal component is halfway between the closest two waveforms in the dictionary. The corresponding phase error is equal to the maximum resolution error multiplied by  $2\pi nT$  for the linear phase term,  $\pi(nT)^2$  for the quadratic phase term,  $\pi(nT)^3$  for the cubic phase term,  $\pi(nT)^4$  for the 4<sup>th</sup> order phase term, and  $\pi(nT)^5$  for the 5<sup>th</sup> order phase term.

The SNR loss calculated from (4.7) for even minimal resolution errors is significant over a dwell of four seconds. This expression gives an upper bound on loss that is considerably greater than the actual loss for two reasons: the early stage phase errors are partially corrected in later algorithm stages through the selection of waveforms that provide the best match to data that contains residual phase errors; in addition, the phase difference between the true target signal and the closest dictionary waveform changes slightly over the dwell. The latter effect is because the exact range expression is not a polynomial; the polynomial that best approximates the signal phase changes over the dwell depending on the time,  $nT$ , at which the square root expression in (3.16) is expanded. The actual signal

phase may be halfway between two different dictionary waveforms for a portion of the dwell, but not over the whole dwell; thus the upper bound on error is considerably higher than is realistic.

The results shown in Figs. 4.4, 4.6, and 4.7 were achieved with dictionary limits and resolutions given in Table 4.8. Upper and lower limits for the various dictionaries were determined from the radar parameters and maximum target parameters from Table 4.1 and the phase expressions from Table 3.1.

Table 4.8. Dictionary limits and resolutions.

<i>1<sup>st</sup> – 5<sup>th</sup> Order Waveforms</i>	<i>Upper and Lower Limits</i>	<i>Resolution for 500 ms Dwell</i>	<i>Resolution: Dwells Up to 4 s</i>
$\exp(j2\pi f_D(nT))$	$f_D = \pm \text{PRF}/2 \text{ Hz}$	1.0 Hz	1.0 Hz
$\exp(j\pi\varphi_2(nT)^2)$	$\varphi_2 = \pm 80/\text{s}^2$	$1.0/\text{s}^2$	$0.5/\text{s}^2$
$\exp(j\pi\varphi_3(nT)^3)$	$\varphi_3 = \pm 12/\text{s}^3$	$1.0/\text{s}^3$	$0.02/\text{s}^3$
$\exp(j\pi\varphi_4(nT)^4)$	$\varphi_4 = \pm 0.1/\text{s}^4$	–	$0.001/\text{s}^4$
$\exp(j\pi\varphi_5(nT)^5)$	$\varphi_5 = \pm 0.001/\text{s}^5$	–	$0.0001/\text{s}^5$

## 4.5 Summary

The signal model for a moving target must include multiple order phase terms when dwell time is extended beyond the typical short dwell used in Fourier-based processing. Rather than determine these various terms with a filter bank that includes all combinations of phase components, a more efficient method was developed to determine the components of the signal via a multistage process. The individual phase components were determined by isolating the components and finding the best-matched waveforms in phase-specific dictionaries through inner products. The signal components were combined to form the filter for target detection. The multiphase signal model generated by the multistage

algorithm performs significantly better than the conventional linear-phase signal model in maximizing output SINR for targets with unknown motion parameters over an extended dwell time. Performance in the clutter-limited case for an exo-clutter target approaches optimal processing, the case when the target motion is known a priori. Typical improvement in output SINR for a 500 ms dwell is 12–13 dB over conventional processing.

Algorithm performance only deteriorates slightly as compared to optimal processing over a four-second dwell time. Dwell times exceeding 500 ms may not be required for target detection, but these longer dwells may be desirable in other radar applications such as tracking, identification, and imaging.

The dominant time intervals in Table 4.3 used to determine the various signal phase components are based on the radar parameters and ranges of target parameters listed in Table 4.1. The expressions in Table 3.1 are not specific to a particular set of parameters and can be used to determine dominant time intervals for a completely different set of radar and target parameters. Algorithm concepts remain the same, though performance may be negatively affected for target motion parameters that exceed the limits given in Table 4.1.

This single-channel algorithm may be better suited for detection of fast-moving airborne targets than for slow-moving ground targets that ideally require multichannel clutter mitigation techniques for accurate detection. The algorithm may have application as a final temporal processing algorithm following signal processing methods that collapse a multichannel signal down to a single-channel temporal signal.

## CHAPTER 5

### MULTICHANNEL ALGORITHM FOR EXTENDED-DWELL TARGET DETECTION

Multiple factors must be considered when investigating a multichannel solution over an extended dwell time: the effect of the change in angle over the dwell on coherent integration of spatial samples from a particular AOA, practical clutter mitigation methods for a long CPI and multichannel data, and processing techniques for an extended-dwell temporal signal that includes multiple unknown phase terms. Each of these factors is addressed in the development of algorithms presented herein that mitigate clutter and coherently integrate spatial and temporal data collected over an extended dwell time.

The multichannel solution is based on a modification of element-space pre-Doppler STAP [4], a reduced dimension STAP technique [4, 52–55] that cancels clutter on a sub-CPI basis and significantly reduces computational complexity over traditional full covariance methods. Element-space pre-Doppler STAP retains full spatial dimensionality but combines only a few temporal samples at a time. Data are processed in two stages.

The pre-Doppler stage cancels clutter and coherently integrates spatial data from a particular AOA while passing temporal information that maximally covers the frequency spectrum to the subsequent temporal processing stage. The output of the first stage is a single-channel, slow-time signal that retains all the temporal information of the original signal.

Over an extended dwell time, the temporal signal output of the pre-Doppler stage includes multiple unknown phase components. Because of the complexity of the extended-dwell temporal signal, the isolation of the temporal processing stage from the other signal

processing steps provided through pre-Doppler STAP is essential. In addition, the pre-Doppler spatial signal integration and clutter mitigation stage provides a beneficial increase in single-sample SINR prior to the final temporal processing stage.

The pre-Doppler temporal signal output is processed in the final stage by subdividing the signal into multiple smaller sub-CPIs for Fourier-based processing. Receiver operating characteristic (ROC) curves characterize algorithm performance for targets with single-sample SNRs from  $-12$  dB to  $-6$  dB and initial radial velocities between  $0.0$  m/s and  $2.4$  m/s in a strong clutter environment with single-sample CNR equal to  $20$  dB.

Efforts are made to maximize output SINR to improve the accuracy of the detection decision. The multichannel solution uses reduced complexity clutter mitigation techniques with a reduced covariance matrix; thus, the suboptimal output SINR is given by the product of optimal SNR and three loss factors as defined in chapter 2:

$$SINR_{sub} = SINR_{opt} L_1 L_3 L_4, \quad (5.1)$$

where  $L_1$  is the clairvoyant loss,  $SINR_{opt} / SINR_{opt}$ ;  $L_3$  is the reduced complexity SINR loss,  $SINR_{rd} / SINR_{opt}$ ; and  $L_4$  is the signal modeling loss,  $SINR_{sub} / SINR_{rd}$ .

## 5.1 Pre-Doppler Stage

### 5.1.1 Clutter Mitigation and Spatial Integration

In the pre-Doppler stage, the CPI with  $N$  slow-time samples is divided into smaller sub-CPIs, each with  $K$  slow-time samples. Each temporal data set for pre-Doppler processing overlaps the prior set by  $K-1$  temporal samples. This overlap from one sub-CPI to the next ensures that the output of the initial stage retains the slow-time coherent



information necessary for the final temporal processing stage. Pre-Doppler processing applies a weight vector,  $\mathbf{w} = \mathbf{R}_I^{-1}\mathbf{s}$ , to each space-time data snapshot of  $M$  spatial samples and  $K$  temporal samples, where  $\mathbf{R}_I$  is the  $MK \times MK$  interference covariance matrix and  $\mathbf{s}$  is a vector of length  $MK$  equal to the Kronecker product of a  $K$ -sample temporal weight vector,  $\mathbf{w}_t$ , and an  $M$ -sample spatial weight vector,  $\mathbf{s}_s$ :

$$\mathbf{s} = \mathbf{w}_t \otimes \mathbf{s}_s, \quad (5.2)$$

chosen to coherently integrate signal energy arriving from a particular angle and to pass broadband temporal information for subsequent processing. Each application of the weight vector to a data snapshot produces a single output sample. A total of  $N-(K-1)$  sub-CPIs produce a temporal output signal,  $y[n]$ , of length  $N-(K-1)$ . Figure 5.1 shows a diagram of the pre-Doppler STAP concept with  $K$  temporal samples in each sub-CPI.

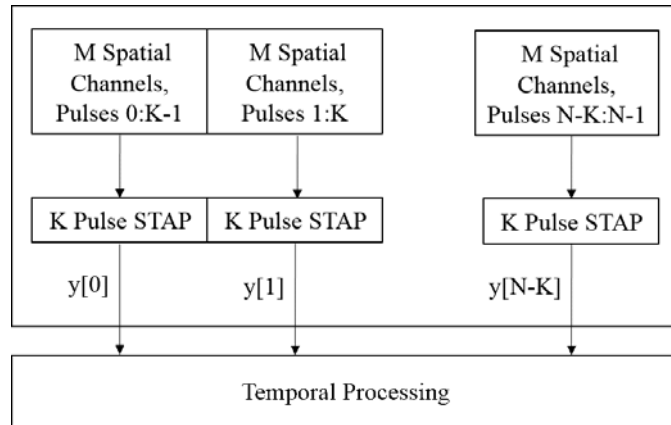


Figure 5.1. Pre-Doppler STAP concept.

The interference covariance matrix is not recreated with each sub-CPI, but rather is generated once and used for all sub-CPIs over the dwell. The  $N-(K-1)$  length temporal output,  $y[n]$ , is the input to the subsequent temporal processing stage.

### 5.1.2 Evaluation of Temporal Weighting Options

Conventional pre-Doppler STAP methods typically use temporal weights based on binomial coefficients to provide broad passband temporal weighting in the pre-Doppler stage [4]. The temporal information is unknown in the first stage, so a broad passband filter that passes maximum target information on to the subsequent temporal processing stage is desirable. An alternative temporal weighting option based on linear prediction coefficients [56–58] is evaluated herein and compared to binomial weighting to determine which method more effectively passes target temporal information to the final processing stage.

Linear prediction is a minimum mean squared error (MMSE) estimation technique used, in this case, to approximate one temporal sample with a weighted combination of the other samples. In a strong clutter environment, the received data is dominated by the clutter signal. The temporal weights can effectively pass target signal information that has different characteristics than the clutter signal by subtracting an estimate of the clutter-dominated data from the actual data. For a temporal weight vector of length  $K$ , the first data sample is estimated with a linear combination of the other  $K-1$  samples. The temporal weight vector applies a weight of one to the first data sample and appropriately weights the other  $K-1$  samples to subtract the estimate of the first temporal sample from the actual sample. Temporal weighting is not intended to cancel clutter; the clutter signal is suppressed through application of the  $\mathbf{R}_1^{-1}$  term in the weight vector. The temporal weights based on linear prediction coefficients exploit the strength of the clutter signal and the

narrowness of the Doppler region occupied by the clutter to pass maximum frequency coverage of the target signal onto the subsequent temporal processing stage. The more similar the target signal is to the strong clutter signal, the more likely it is to be subtracted out with the clutter estimation. Linear prediction weight calculation is included in Appendix A.

Radar and target parameters used for algorithm development and evaluation are given in Table 5.1. These are the same as those used for evaluation of the single-channel algorithm presented in chapter 4.

Table 5.1. Radar and target parameters for multichannel algorithm.

<i>Parameter</i>	<i>Magnitude</i>
Center frequency, $f_c$	10 GHz
Platform velocity, $V_p$	100 m/s
Platform height, $h$	3 km
Slant range, $r$	20 km
Pulse Repetition Frequency, PRF	1000 samples/s
Target radial and tangential velocity, $V_y$ and $V_x$	1.0 – 15.0 m/s
Target radial and tangential acceleration, $A_y$ and $A_x$	0.1 – 1.0 m/s <sup>2</sup>
Target radial and tangential jerk, $J_y$ and $J_x$	0.1 – 0.5 m/s <sup>3</sup>

Three spatial channels and a dwell time of one second were used for algorithm development and evaluation. A one-second dwell is well within the requirements for spatial correlation given by (3.35) for the parameters in Table 5.1. The multichannel algorithm concepts can be applied to dwells other than one second and for parameters other than those listed in Table 5.1. However, limits in dwell time imposed by spatial correlation constraints must be considered for any set of parameters. The pre-processing target signal, clutter, and

noise power in the three channels used to evaluate the different temporal weighting scenarios are shown in Figure 5.2.

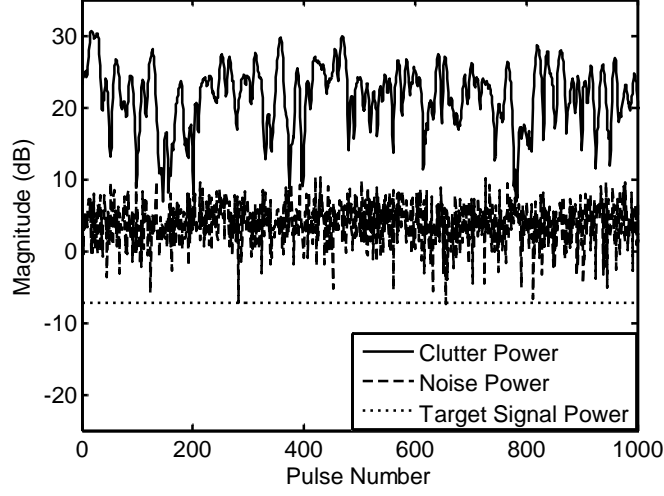


Figure 5.2. Three combined channels of clutter, noise, and signal power input to pre-Doppler processing.

Temporal weights based on binomial coefficients, where the  $k^{th}$  binomial coefficient for a filter of length  $K$  is given by

$$k = (-1)^k \frac{(K-1)!}{(K-1-k)!k!} \quad k = 0, \dots, K-1, \quad (5.3)$$

were compared to linear prediction weights to determine which weighting method more effectively passes maximum target magnitude and frequency coverage to the final temporal processing stage. Comparisons were based on frequency responses and single-sample pre-Doppler output SINRs for the different weighting options. Frequency responses of the binomial filter are shown in Figure 5.3 for lengths of 3, 5, 7, and 9, all normalized to a gain of one.

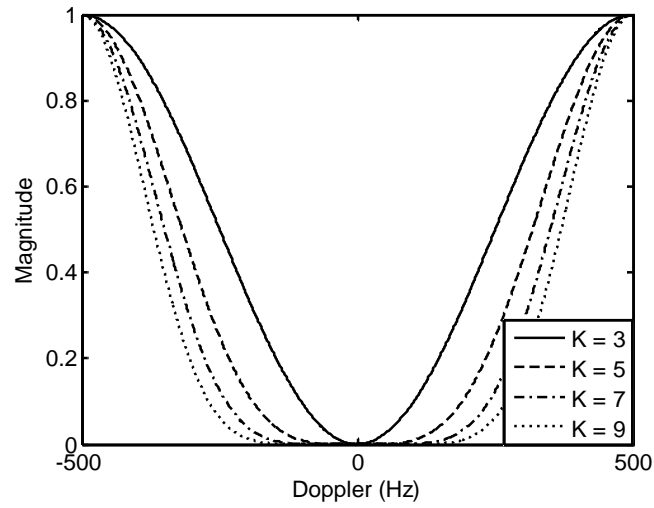


Figure 5.3. Frequency responses of normalized binomial weights for lengths of 3, 5, 7, and 9.

Figure 5.3 shows that a binomial filter of length three best supports the goal of passing maximum target signal magnitude and frequency coverage to the final temporal processing stage. Frequency responses of the three-sample binomial filter and twenty averaged trials of the three-sample linear prediction weight vector are shown in Figure 5.4.

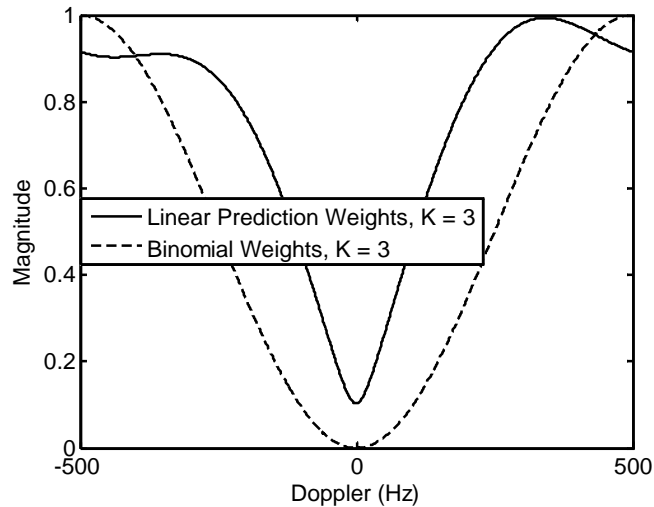


Figure 5.4. Frequency responses of three-sample linear prediction weight vector and three-sample binomial weight vector.

Figure 5.4 shows that the linear prediction weight vector has a sharper notch that allows more low-Doppler target information to pass to the final temporal processing stage.

A comparison of output SINRs from the first stage of pre-Doppler processing as a function of pulse number is shown for twenty averaged trials in Figure 5.5 for binomial and linear prediction temporal weights. Target radial velocity is 1.5 m/s, sub-CPI length is three samples, and total CPI length is one second.

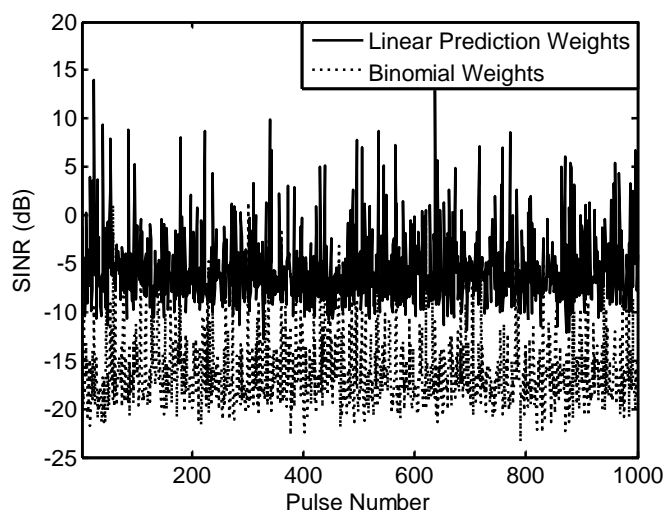


Figure 5.5. Twenty averaged pre-Doppler SINR outputs for binomial and linear prediction temporal weights of length three and a target radial velocity of 1.5 m/s.

The higher single-sample output SINR shown in Figure 5.5 for the linear prediction weights confirms that linear prediction weights are superior to binomial weights for passing weak, low-Doppler target signal energy to the final temporal processing stage.

The temporal weight vector determined through linear prediction is calculated with a reduced covariance matrix as detailed in Appendix A. This reduced covariance matrix is frequently singular for a temporal weight vector of length three. Matrix singularity is rare for linear prediction temporal weight vector lengths greater than three. In fifty trials, linear

prediction weights with four, five, and six temporal samples showed similar output SINR levels. Thus, the temporal weight vector length,  $K$ , was chosen to be equal to four samples to minimize both matrix singularities and computational complexity. The linear prediction weights are determined with the first four slow-time data samples and are used to process all  $N-(K-1)$  sub-CPIs.

## 5.2 Temporal Processing Stage

### 5.2.1 Temporal Signal Analysis

The final temporal processing algorithm is based on a frequency domain analysis of the extended dwell time temporal signal. The multichannel algorithm concepts can be applied for any dwell time; however, some algorithm specifics are based on frequency domain analysis for a particular dwell time. The analysis presented herein assumes the temporal signal is one second in duration.

Table 3.4 lists the changes in instantaneous frequency over different dwell times attributable to the various nonlinear phase components for a target with parameters equal to the maximum values given in Table 5.1. Over a one-second dwell, the combined maximum Doppler spread, or change in instantaneous frequency, from all of the nonlinear phase components is slightly less than 100 Hz. The maximum combined spread from the cubic and higher phase components is primarily from the cubic phase component over a one-second dwell. The spread from the cubic phase component is approximately 17 Hz for a one-second dwell. These target parameter and dwell time dependent values of  $\sim 100$  Hz for the combined spread and  $\sim 17$  Hz for the cubic phase spread are used in the extended-dwell temporal processing algorithm. The expressions in Table 3.3 can be used to

determine the maximum expected frequency spread for a different set of radar and target parameters and over different dwell times.

Because the energy of the extended dwell time signal spreads across multiple Doppler bins, conventional Fourier-based temporal processing methods such as Doppler processing are not effective at coherently integrating signal energy. The frequency spectrum of the temporal signal using the maximum parameters from Table 5.1 is shown in Figure 5.6 over a one-second dwell. The maximum change in Doppler shown over a one-second dwell is consistent with the estimate for the combined components given in Table 3.4.

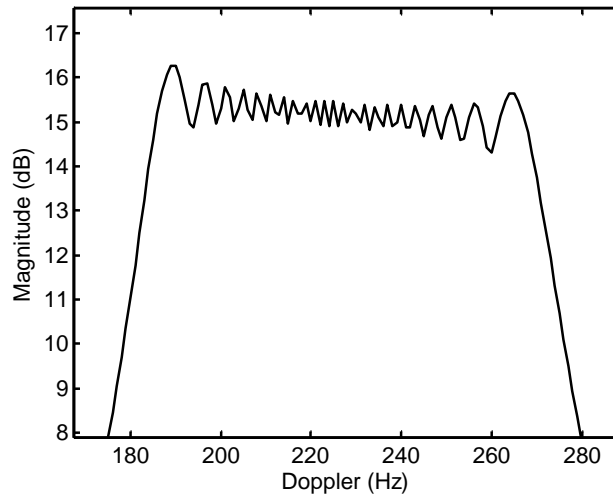


Figure 5.6. Doppler spread of target signal with maximum target parameters over a one-second dwell.

Though Doppler processing cannot be used effectively over the entire signal duration, the temporal signal can be divided into smaller sub-CPIs that can effectively be processed with Fourier transforms. The dwell time over which the target signal can be approximated as a linear-phase signal and for which a discrete Fourier transform (DFT)



coherently integrates signal energy depends on when the higher-order phase effects appear in the signal. As dwell time increases, the effects of the quadratic phase component begin to emerge, followed by the cubic phase component and higher order terms. Since the quadratic phase component appears before the higher order components, the time over which the signal can be modeled with a linear phase depends on when these effects appear in the signal. The expression for the quadratic phase component given in Table 3.1 is dominated by the radial acceleration term,  $(-2\pi A_y y_0 / \lambda_0 r)(nT)^2$ . Higher values of radial acceleration cause the quadratic phase effects to appear earlier in the signal than lower values.

A DFT of the signal shows the magnitude of the energy at each frequency with resolution equal to the PRF divided by the number of frequency bins. For a signal modeled with a linear plus quadratic phase component,

$$s(nT) = \exp(j(2\pi f_D nT + \pi \alpha (nT)^2)), \quad (5.4)$$

signal energy accumulates in the bin corresponding to  $f_D$  at the beginning of the dwell. The quadratic phase component shifts a portion of signal energy to adjacent Dopplers beginning early in the dwell and continuing until the quadratic phase reaches a magnitude of  $\pi/2$  radians. After this point, no more energy is added to the original Doppler bin. The dwell time at which the quadratic phase reaches  $\pi/2$  radians depends on radar and target parameters. For the parameters given in Table 5.1, this dwell time is determined by setting the absolute value of the quadratic phase expression from Table 3.1 equal to  $\pi/2$ , inserting the radar parameters and target parameters from Table 5.1 into the expression, and solving for  $nT$ . Maximum target parameters from Table 5.1 are used to establish the duration over which the temporal signal is approximately a linear-phase signal and for which DFT

processing accumulates signal energy in the same Doppler bin. This dwell time of approximately 100 ms is used as the sub-CPI duration in the extended-dwell temporal processing algorithm. Complete decorrelation with the linear-phase model occurs sooner than 100 ms for target parameters exceeding those listed in Table 5.1 or for operation at a higher frequency. In this situation, a dwell of 100 ms can still be used as the sub-CPI length in the extended-dwell temporal processing algorithm; however, a higher single-sample SNR is required for equivalent results to those achieved for radar and target parameters listed in Table 5.1.

The target signal whose frequency spectrum is shown in Figure 5.6 was subdivided into 100 ms sub-CPIs. The frequency spectrum of each sub-CPI, overlaid to show the progression of the change in Doppler over the dwell, is shown in Figure 5.7.

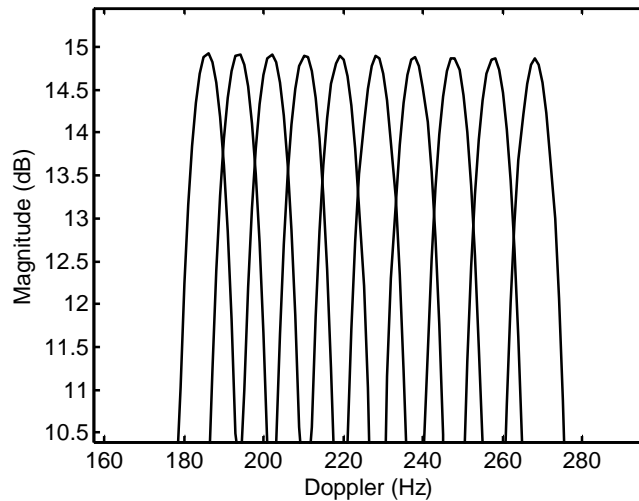


Figure 5.7. Overlaid frequency spectra of the ten 100 ms sub-CPIs for maximum target parameters.

The quadratic phase component causes a linear shift in Doppler from one sub-CPI to the next. The cubic phase term causes a quadratic shift in Doppler from one sub-CPI to the next; the rate of change in Doppler from one sub-CPI to the next depends on the

magnitude of the cubic phase term and the sign of the term relative to the quadratic phase term. The effects of the cubic phase component become more acute as dwell time increases.

### 5.2.2 Extended-Dwell Temporal Processing Algorithm

Beginning with the idea of dividing the temporal signal into smaller sub-CPIs that can be approximated as linear-phase signals and processed with DFTs for coherent integration of signal energy, we strive to maximize  $P_D$  for a given  $P_{FA}$ . Two methods for utilizing the signal energy in the sub-CPIs to make the detection decision were evaluated to determine which method is more effective at detecting weak targets. The temporal processing algorithm is the same for each method; however, the detection decisions are based on different observations.

For both methods, processing of the temporal signal,  $y[n]$ , begins by dividing the signal into sub-CPIs of length 100 ms and processing each sub-CPI with a DFT. The dominant frequency component in each sub-CPI is sorted into one of  $(PRF/50)$  frequency bands 50 Hz wide ranging from  $-PRF/2$  to  $PRF/2$  Hz. Because the maximum Doppler spread over a one-second dwell for the parameters in Table 5.1 is slightly less than 100 Hz, the two consecutive 50 Hz bands that contain the most dominant frequencies are assumed to contain target signal energy; this span of 100 Hz is designated the target frequency range.

In some sub-CPIs, the dominant frequency corresponds to a spike in noise. These noise spikes most often occur outside the assumed target frequency range, but occasionally occur within this range. Noise spikes occurring within the designated target range are more common for targets with lower single-sample SNRs.

Because the quadratic phase component is the dominant nonlinear signal component over a one-second dwell, the difference in target Dopplers between two

adjacent sub-CPIs is primarily due to the quadratic phase term. An estimate of this shift,  $\Delta f_{D2}$ , can be determined by dividing the difference between the first two dominant frequencies in the target frequency range by the difference in their corresponding sub-CPI numbers. The Doppler shift between sub-CPIs due to the cubic and higher order phase components is not easily estimated from the data. Spreading from these phase components is primarily attributable to the cubic phase component over one second. For parameters in Table 5.1, the maximum spread from the cubic phase component over a one-second dwell is given in Table 3.4 as approximately 17 Hz. This means the cubic phase component causes an approximate maximum shift in Doppler of  $(17)(.1*\Delta\text{sub-CPI})^2$  Hz between two sub-CPIs separated in time by  $(.1*\Delta\text{sub-CPI})$  seconds. If we define  $\Delta\text{index}$  as the difference in sub-CPI numbers between a sub-CPI whose dominant frequency is from a noise spike and the closest sub-CPI whose dominant frequency is in the target range, the temporal processing algorithm can estimate missing target Doppler information by searching for a local maximum in the frequency neighborhood defined by: closest target Doppler +  $\text{round}(\Delta f_{D2}*\Delta\text{index}) \pm \text{round}((17 \text{ Hz})(.1*\Delta\text{index})^2)$ .

An example of the original dominant frequencies in each sub-CPI and the correctly located target Dopplers as determined by the algorithm is given in Table 5.2 for a one-second dwell. The algorithm differentiates between frequencies 1 Hz apart; for a PRF of 1000, a 1000-point DFT of each sub-CPI provides 1 Hz resolution.

Table 5.2. Original dominant frequencies and algorithm-corrected target Dopplers.

<i>Sub-CPI</i>	<i>Original Dominant Frequency (Hz)</i>	<i>Algorithm Results: Target Dopplers (Hz)</i>
1	-243	-123
2	-255	-130
3	-252	-135
4	-339	-141
5	-146*	-146
6	-153*	-153
7	-158*	-158
8	-306	-165
9	-172*	-172
10	-178*	-178

\*Correspond to correct target Dopplers; used to locate other target Dopplers.

By filling in the missing Doppler information, the temporal processing algorithm provides information on target initial radial velocity and the approximate change in radial velocity over the dwell.

#### 5.2.2.1 Detection Decision

The detection decision between the two hypotheses,  $H_0$  and  $H_1$ , is ideally based on decision regions  $\mathcal{R}_0$  and  $\mathcal{R}_1$  that are as far apart as possible. The pdfs for an observation  $x$ ,  $p_{x|H_0}(x|H_0)$  and  $p_{x|H_1}(x|H_1)$ , have minimal overlap to maximize  $P_D$  for a given  $P_{FA}$ .

For the first decision basis, we define the observation,  $x$ , as the noncoherent sum of target signal magnitudes from each sub-CPI. An estimate of the pdfs for the observed data  $x$ : (1)  $p_{x|H_0}(x|H_0)$ , the pdf of  $x$  given that  $H_0$  is true, and (2)  $p_{x|H_1}(x|H_1)$ , the pdf of  $x$  given that  $H_1$  is true for an exo-clutter target with a single-sample SNR of -6 dB, are shown in Figure 5.8. The pdfs were estimated with 200 Monte Carlo trials in each case.

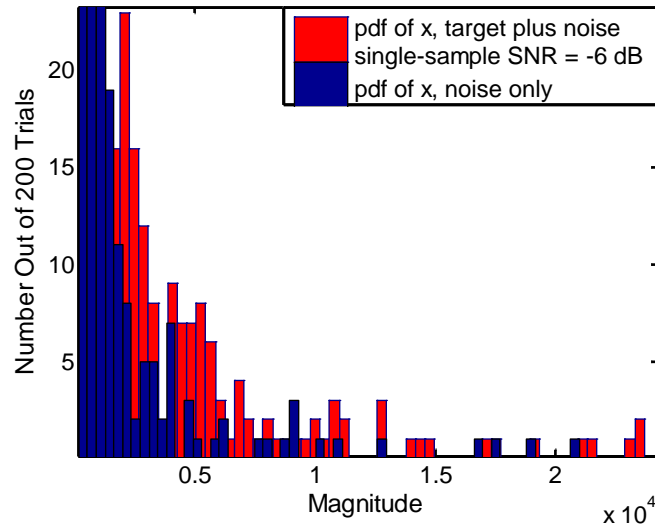


Figure 5.8. Pdfs for  $p_{x|H_0}(x|H_0)$  and  $p_{x|H_1}(x|H_1)$  for detection decision based on noncoherent integration of target signal magnitudes for a pre-processing single-sample SNR of -6 dB.

The overlap of pdfs shown in Figure 5.8 prohibits an accurate detection decision in most cases for a single-sample SNR less than or equal to -6 dB. The pdfs overlap more as single-sample SNR decreases. The overlap of pdfs results at least partially from combining signal energy that corresponds to maximum magnitude frequency components in each sub-CPI and from searching for local maximums to locate target signal energy. For low SNR targets, the sum of magnitudes in each sub-CPI in the  $H_1$  scenario is often equivalent to or less than the sum of magnitudes in the noise-only scenario.

The second criteria for the detection decision is based on the pattern of dominant frequencies in the sub-CPIs. The algorithm does not locate all the correct target Dopplers before making the detection decision. Over a one-second dwell, the target Doppler is an approximate linear function of sub-CPI, because the spread in Doppler is primarily from the quadratic phase component, which causes a linear shift in Doppler between sub-CPIs. In comparison, the frequency components of the noise signal are completely random

between sub-CPIs. This difference between the pattern of target Dopplers and the pattern of noise from one sub-CPI to the next can be exploited to improve the detection decision.

The frequency versus sub-CPI line between the first and last dominant frequencies that were originally sorted into the designated target frequency range can be used to model the target signal and provide a basis for the decision between the  $H_0$  and  $H_1$  hypotheses. Each frequency in the assumed target frequency range is tested for proximity to this line. Dominant frequencies corresponding to target Dopplers are generally within close proximity to the line. In the  $H_0$  scenario, the dominant frequencies are random and are generally much farther from the line. An example is shown in Figure 5.9 to demonstrate the decision criteria.

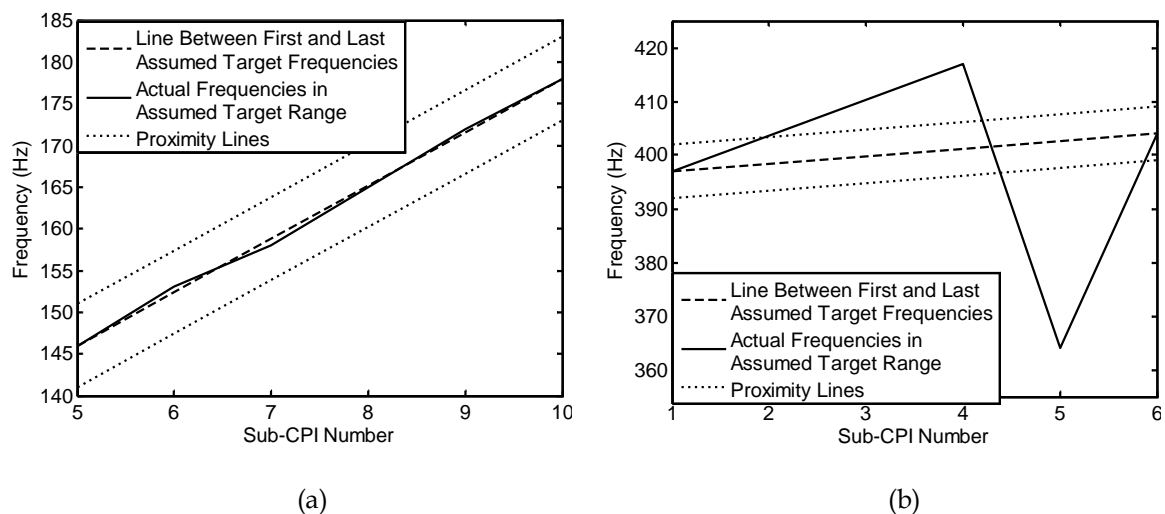


Figure 5.9. Examples with line proximity for detection decision for (a)  $H_1$  and (b)  $H_0$  hypotheses.

Line proximity for the examples in Figure 5.9 is 5 Hz. In Figure 5.9(a), the first and last dominant frequencies in the assumed target frequency range are in sub-CPIs five and ten; a frequency versus sub-CPI line is created between sub-CPIs five and ten and their corresponding dominant frequencies. Other dominant frequencies that were also originally

sorted into the designated target frequency range are tested for proximity to this line. Each of the other dominant frequencies is within 5 Hz from the line; thus, the  $H_1$  hypothesis is chosen. In Figure 5.9(b), a line is created between sub-CPIs one and six and their corresponding dominant frequencies. The dominant frequencies in the fourth and fifth sub-CPIs were sorted into this same target frequency range. The dominant frequencies in sub-CPIs four and five are farther than 5 Hz from the line; thus, the  $H_0$  hypothesis is chosen.

For the second decision basis, we define the observation,  $x$ , as the distance in hertz of the dominant frequency in the designated target frequency range that is the greatest distance from the frequency versus sub-CPI line. The  $H_1$  decision requires  $x$  to be within a certain proximity of the line. The pdfs for the observed data  $x$ : (1)  $p_{x|H_0}(x|H_0)$ , the pdf of  $x$  given that  $H_0$  is true, and (2)  $p_{x|H_1}(x|H_1)$ , the pdf of  $x$  given that  $H_1$  is true for an exocutter target with single-sample SNRs of  $-6$  dB and  $-12$  dB, are shown in Figure 5.10. The pdfs were estimated with 400 Monte Carlo trials in each case.

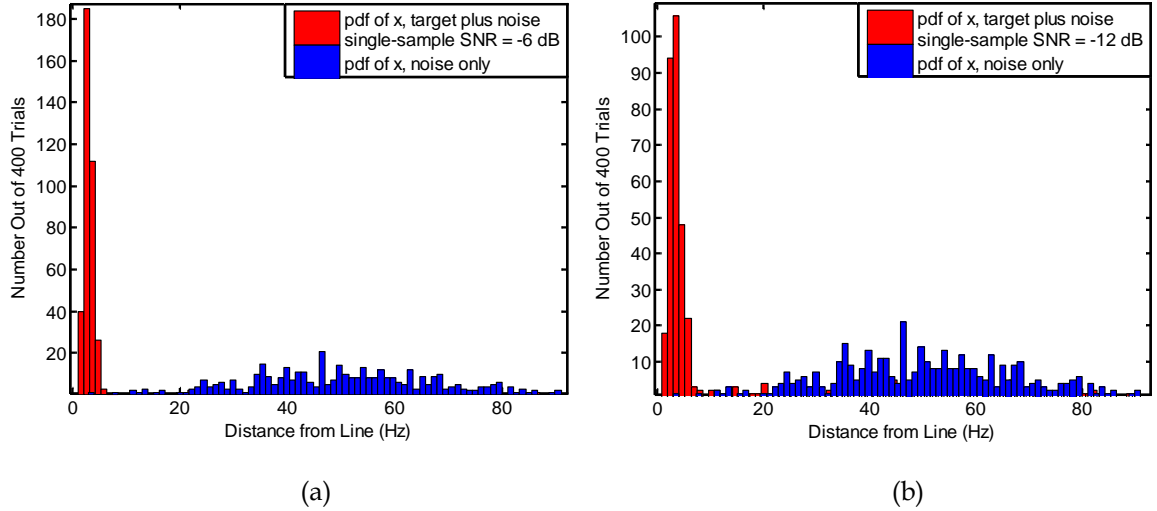


Figure 5.10. Pdfs for  $p_{x|H_0}(x|H_0)$  and  $p_{x|H_1}(x|H_1)$  for detection decision based on line proximity for pre-processing single-sample SNRs of (a)  $-6$  dB and (b)  $-12$  dB.



The pdfs for the observation based on the second decision criteria, line proximity, are much further apart than the pdfs for the first decision criteria, noncoherently combined magnitudes, shown in Figure 5.8. The greater separation of pdfs yields a higher  $P_D$  for a particular  $P_{FA}$ . Thus, the decision criteria based on line proximity was chosen for the temporal processing algorithm. The pdf for observation  $x$ ,  $p_{x|H_1}(x|H_1)$  for a single-sample SNR of  $-12$  dB is slightly more spread out than for a single-sample SNR of  $-6$  dB. This increased variance corresponds to a decline in algorithm performance for lower SNR because higher relative noise levels cause more dominant frequencies from noise spikes.

The value chosen for line proximity affects both  $P_D$  and  $P_{FA}$ . Requiring all tested frequencies to be within a very narrow margin of the line decreases both  $P_D$  and  $P_{FA}$ , while allowing the frequencies to be a greater distance from the line increases both  $P_D$  and  $P_{FA}$ .

For dwells greater than one second, the change in target Doppler increasingly becomes a linear-plus-quadratic function of dwell time. Dominant frequencies fall on a slightly bowed line between the first and last dominant frequencies in the target frequency range as dwell increases. For dwells greater than one second, the detection decision can still be based on line proximity since the frequency characteristics of the noise and target are still very different. Line proximity used to decide between the  $H_0$  and  $H_1$  hypotheses may increase slightly to allow for the small quadratic change in Doppler as dwell increases.

This algorithm with the detection decision based on line proximity will be referred to as the extended-dwell temporal processing (EDTP) algorithm.

#### 5.2.2.2 Flow Diagram

A flow diagram of the EDTP algorithm is shown in Figure 5.11.

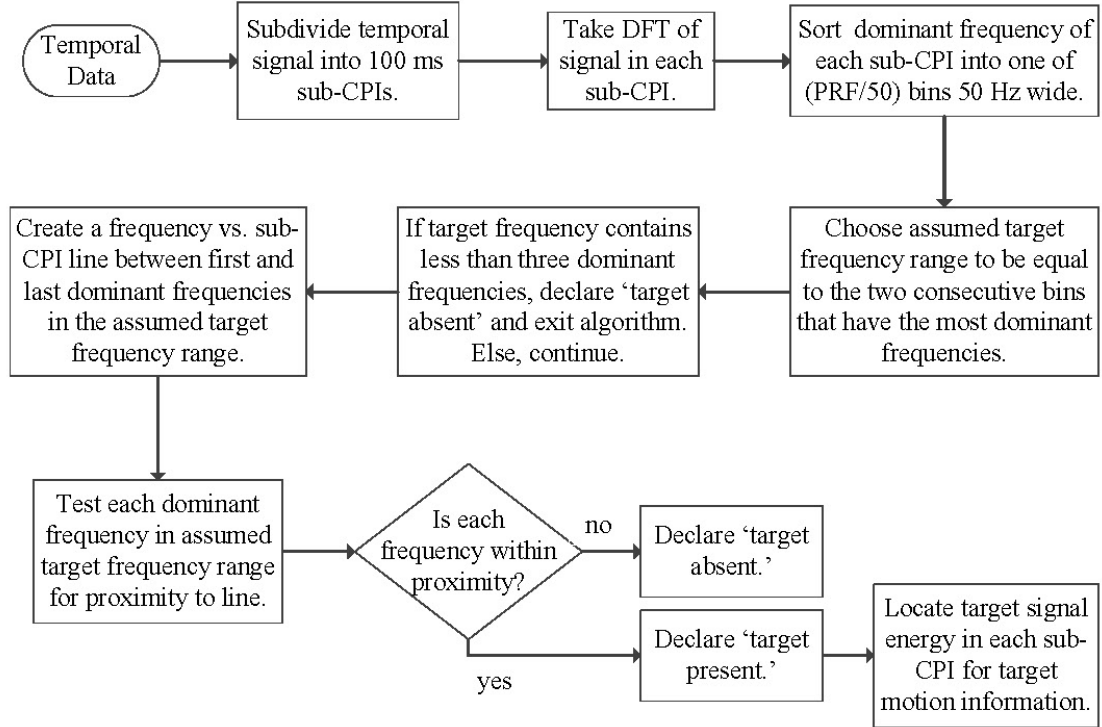


Figure 5.11. EDTP algorithm flow diagram.

### 5.3 Performance Characterization

The performance of the EDTP algorithm depends on the SINR of the output signal from the pre-Doppler stage. This output SINR depends on both the input single-sample SINR to the pre-Doppler stage and the effectiveness of the pre-Doppler processing method in passing target signal energy to the final algorithm. The EDTP algorithm relies on sufficient signal energy for the correct target frequency range to be determined. Insufficient signal energy is most common for low radial velocity targets that have a portion of their energy in the clutter frequency region. The EDTP algorithm often fails to detect targets that have most of their signal energy in the clutter region. A less common detection failure is caused by a noise spike appearing in the target frequency range. Both of these failures lower the  $P_D$ . Spatial weights are assumed to coherently integrate spatial samples.

Evaluation at various initial radial velocities for the accelerating target and final radial velocities for the decelerating target over an extended dwell time are more relevant figures of merit than minimum detectable velocity (MDV) since the radial velocity of the extended dwell target signal often changes over the dwell.

### 5.3.1 EDTP Algorithm, Endo-Clutter Targets

For this evaluation, a target is declared present if each frequency in the designated target frequency range is within 5 Hz from the frequency versus sub-CPI line determined by the first and last dominant frequencies in the target frequency range. In 1000 algorithm trials with no target present, a CNR of 20 dB, and a line proximity of 5 Hz, the incorrect ‘target present’ decision was made once, which corresponds to an estimated  $P_{FA}$  of 0.001.

The  $P_D$  was determined for accelerating targets with initial radial velocities ranging from 0.6 m/s to 2.4 m/s for various single-sample SNRs and for a single-sample CNR of 20 dB. A radial acceleration of  $1.0 \text{ m/s}^2$  causes target radial velocity to increase by approximately 1.0 m/s over a one-second dwell; an accelerating target with initial radial velocity of 0.6 m/s will reach a maximum radial velocity of approximately 1.6 m/s after one second. A target with initial radial velocity of 1.6 m/s, decelerating at  $1.0 \text{ m/s}^2$  will slow to a radial velocity of approximately 0.6 m/s after one second. These two types of targets occupy the same Doppler frequencies over a one-second dwell; thus, algorithm performance is very similar. Performance results are only shown for the accelerating target.

ROC curves in Figure 5.12 illustrate EDTP algorithm performance for various initial radial velocities and pre-processing single-sample SNRs. Other target parameters are equal to the maximum values in Table 5.1.

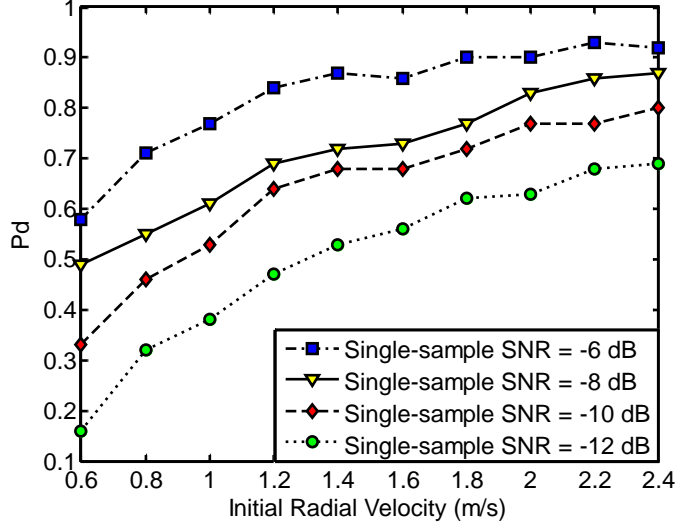


Figure 5.12. ROC curves for the EDTP algorithm showing  $P_D$  as a function of initial radial velocity for an accelerating target with various single-sample SNRs.

For the EDTP algorithm, performance is better for an accelerating target with low initial radial velocity than for either a target with a constant low radial velocity or a decelerating target with low initial radial velocity. The signal energy of the accelerating target spreads to regions outside of the mainlobe clutter Doppler region, which improves detection. For all of the SNRs, the  $P_D$  for a target with a constant radial velocity of 0.6 m/s drops to approximately 40% of the  $P_D$  achieved for an accelerating target with an initial radial velocity of 0.6 m/s over a one-second dwell time. The  $P_D$  for the constant radial velocity target gradually approaches the  $P_D$  for the accelerating target as radial velocity increases. Equivalent performance is achieved for an accelerating target with 1.6 m/s initial radial velocity and a target with a constant radial velocity of 1.6 m/s.

The more similar the target signal is to the clutter signal, the more likely it is to be suppressed during the pre-Doppler stage along with the dominant clutter signal. In order to improve performance for targets in the low Doppler region, a modification was made to the EDTP algorithm to search for low radial velocity targets only.

### 5.3.2 Extended-Dwell Limited Search (EDLS) Algorithm, Endo-Clutter Targets

The EDTP algorithm was modified to search only for low velocity targets by removing from consideration the Doppler bins that correspond to target radial velocities with magnitude greater than 3.0 m/s. This modification of the EDTP algorithm, called the extended-dwell limited search (EDLS) algorithm, limits detection to decelerating targets whose maximum initial radial velocity is 3.0 m/s and accelerating targets whose maximum final radial velocity is 3.0 m/s. Figure 5.13 shows the  $P_D$  for accelerating targets with initial radial velocities ranging from 0.0 m/s to 1.8 m/s for various single-sample SNRs. Results are representative of both accelerating targets with initial radial velocities from 0.0 m/s to 1.8 m/s and decelerating targets with initial radial velocities from approximately 1.0 m/s to 2.8 m/s. The estimated  $P_{FA}$  for the results shown in Figure 5.13 is 0.001.

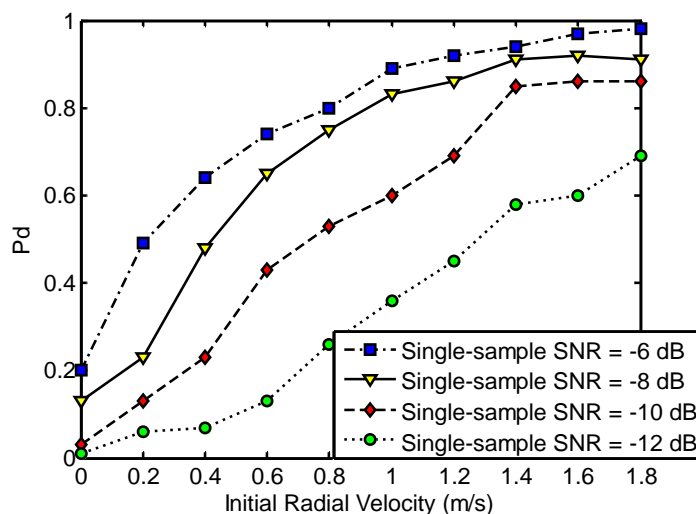


Figure 5.13. ROC curves for the EDLS algorithm showing  $P_D$  as a function of initial radial velocity for an accelerating target with various pre-processing single-sample SNRs.

By constraining the target model, the EDLS algorithm detects a higher percentage of low radial velocity targets than the EDTP algorithm that searches over the whole Doppler spectrum.

### 5.3.3 Comparison of EDTP and EDLS Algorithms, Endo-Clutter Targets

A comparison of the EDTP and EDLS algorithms is shown in Figure 5.14 for accelerating targets with initial radial velocities from 0.6 m/s to 1.8 m/s for single-sample input SNRs of  $-6$  dB and  $-8$  dB.

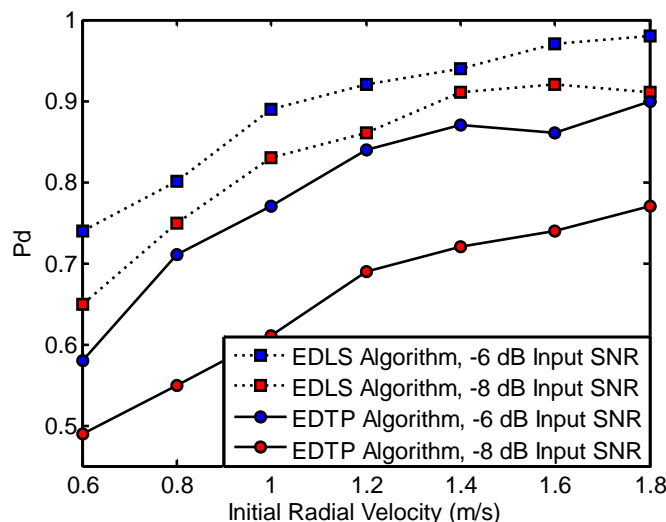


Figure 5.14. ROC curves for EDLS and EDTP algorithms showing  $P_D$  as a function of initial radial velocity for an accelerating target with single-sample SNRs of  $-6$  dB and  $-8$  dB.

Figure 5.14 confirms the previous conclusion that detection of low radial velocity targets is improved by limiting the frequency spectrum over which the algorithm searches.

### 5.3.4 EDTP Algorithm, Exo-Clutter Targets

One thousand Monte Carlo trials were used to establish line proximity thresholds for  $P_{FAS}$  of 0.001 and 0.01 for the EDTP algorithm. The pdf of  $p_{x|H_0}(x|H_0)$  that was used to establish the thresholds is shown in Figure 5.15.

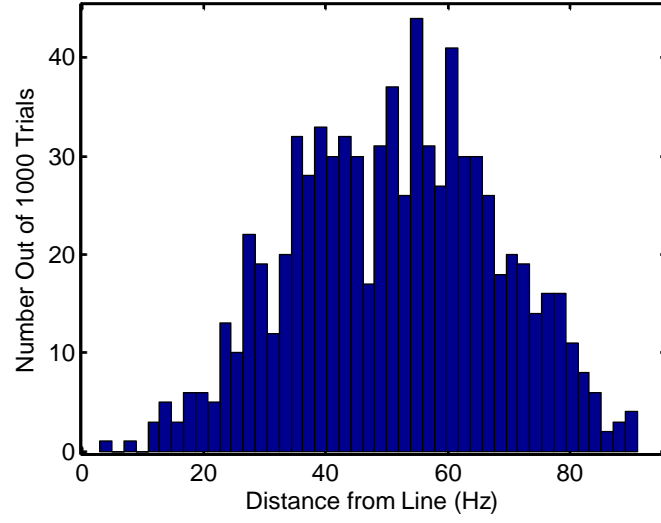


Figure 5.15. Pdf of  $p_{x|H_0}(x|H_0)$  used to establish line proximity for  $P_{FAS}$  of 0.001 and 0.01.

Out of 1000 Monte Carlo trials for the  $H_0$  scenario, Figure 5.15 shows the smallest single data point for line proximity at 5 Hz; thus, requiring each dominant frequency in the designated target frequency range to be within 5 Hz from the frequency versus sub-CPI line for ‘target present’ to be declared corresponds to a  $P_{FA}$  of approximately 0.001. Out of the same 1000 trials, the ten closest line proximities were less than or equal to 15 Hz. Thus, a line proximity of 15 Hz corresponds to a  $P_{FA}$  of approximately 0.01. ROC curves showing extended-dwell algorithm performance for an exo-clutter target are shown in Figure 5.16.  $P_D$  versus SNR for  $P_{FAS}$  of 0.001 and 0.01 are shown for an accelerating target with an initial radial velocity of 2.4 m/s. The  $P_D$  was determined with 100 Monte Carlo trials.

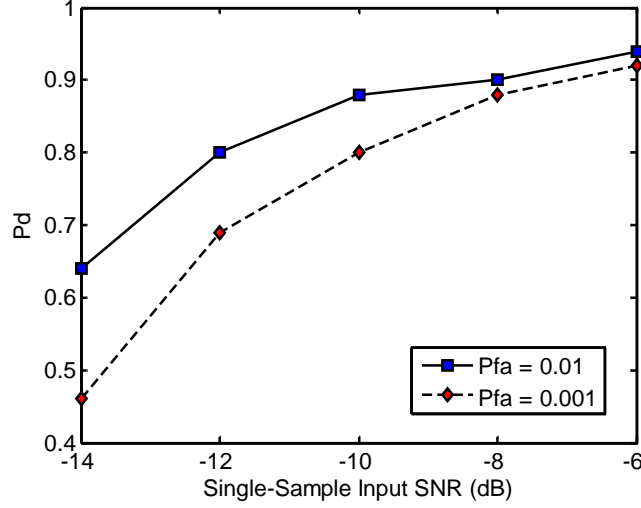


Figure 5.16. ROC curves for the EDTP algorithm for an exo-clutter target showing  $P_D$  as a function of single-sample input SNR for  $P_{FA}$ s of 0.001 and 0.01.

The  $P_D$  for a  $P_{FA}$  of 0.01 is only slightly better than the  $P_D$  for a  $P_{FA}$  of 0.001 for the higher input SNRs. This is because for the  $H_1$  hypothesis, the observation,  $x$ , is very concentrated around the 0 to 5 Hz range, as illustrated in Figure 5.10(a) for an input single-sample SNR of  $-6$  dB, and rarely occurs between 5 and 15 Hz. For lower single-sample SNRs the likelihood of  $x$  occurring between 5 and 15 Hz increases. The pdf,  $p_{x|H_1}(x|H_1)$ , for lower single-sample SNRs is more spread out as shown in Figure 5.10(b) and overlaps  $p_{x|H_0}(x|H_0)$  more than for higher single-sample SNRs; thus, a wider gap in performance between  $P_{FA}$ s of 0.001 and 0.01 occurs for lower single-sample SNRs. The  $P_{FA}$  of 0.01 allows an observation,  $x$ , between 5 and 15 Hz to be classified as a target even if it is due to a noise spike; this improves detection of lower single-sample SNR targets for a  $P_{FA}$  of 0.01 as compared to detection for a  $P_{FA}$  of 0.001.

No signal energy spreads into the mainlobe clutter Doppler region for exo-clutter targets; thus, algorithm performance for this evaluation does not depend on target motion parameters.



## 5.4 Doppler Processing Comparison

Conventional Pre-Doppler STAP utilizes Doppler processing in the final stage to determine target temporal information. Doppler processing uses DFTs to coherently integrate signal energy and is only effective for a dwell time of approximately 100 ms for typical radar and target parameters such as those listed in Table 5.1. The SNR must be sufficiently high such that Doppler processing over this short dwell consistently yields accurate target information.

To directly compare performance of the EDTP algorithm to Doppler processing of the temporal output signal from the pre-Doppler stage, a threshold for Doppler processing was established through a Monte Carlo approach to achieve a  $P_{FA}$  of 0.001. Out of 100 trials, zero Doppler processing outputs exceeded the threshold for an exo-clutter target with single-sample SNRs between  $-12$  dB and  $-6$  dB. Only a few of the Doppler processing outputs exceeded the threshold established for a  $P_{FA}$  of 0.01 for single-sample SNRs between  $-12$  dB and  $-6$  dB.

Pre-Doppler temporal weights based on linear prediction coefficients subtract an estimate of the signal from the actual signal. As single-sample input SNR increases, linear prediction weights estimate and subtract off a larger portion of target signal energy in addition to the clutter signal energy. In a comparison of the EDTP algorithm and Doppler processing for higher single-sample SNRs, temporal weights based on binomial coefficients provide a better representation of Doppler processing performance than linear prediction weights.

For typical GMTI radar parameters and a target with an initial radial velocity of 1.6 m/s, a single-sample SNR of approximately 5 dB is required for Doppler processing with

binomial weights to achieve the same  $P_D$  as the EDTP algorithm achieves with linear prediction weights for a single-sample SNR of  $-6$  dB in 500 trials with a  $P_{FA}$  of 0.001. From the radar range equation [59], SNR is an inverse function of range to the fourth power; thus, a decrease of 11 dB in required single-sample SNR for equivalent detection almost doubles the detection range.

The difference in the required single-sample SNR that yields equivalent  $P_D$  for the EDTP algorithm and Doppler processing increases as initial radial velocity decreases. Conversely, the difference in the required single-sample SNR that yields equivalent  $P_D$  for the two methods decreases as initial radial velocity increases.

## 5.5 Summary

STAP methods typically used for detection of slow-moving ground targets assume a linear-phase slow-time signal model and a fixed angle between the platform and the target; these assumptions are only accurate over a dwell time whose duration does not provide adequate temporal integration for detection of weak targets.

Multichannel solutions based on pre-Doppler STAP were developed to mitigate clutter and coherently integrate spatial and temporal samples in a two-stage process. A comparison of temporal weighting methods in the pre-Doppler stage showed linear prediction coefficients superior to the traditional binomial coefficients for passing maximum target information to the final temporal processing stage. A temporal processing algorithm for the extended dwell time signal sub-divides the temporal signal into smaller sub-CPIs and coherently integrates the signal energy in each sub-CPI with a DFT. Two different detection decision methods were examined; the decision criteria that provides better detection is based on differences in patterns of signal energy between the target

signal and the noise from one sub-CPI to the next.

The EDTP algorithm has a significantly higher detection rate of low single-sample SNR targets, especially at low radial velocities, than Doppler processing of the pre-Doppler temporal output signal.

## **CHAPTER 6**

### **CONCLUSIONS AND FUTURE WORK**

#### **6.1 Conclusions**

The algorithms developed and presented in this dissertation improve detection of weak targets from a small radar platform as compared to current state-of-the-art detection methods. Detection improvement is achieved through the coherent integration of target signal energy collected over an extended dwell time. Two approaches to integrate signal energy for a weak target with unknown motion parameters were thoroughly investigated and successfully implemented: (1) a single-channel solution, the multistage algorithm, that determines the linear and nonlinear phase components of the target signal in a multistage process and (2) a multichannel solution that combines pre-Doppler STAP concepts to mitigate clutter with an extended-dwell temporal processing algorithm that subdivides the temporal signal into smaller sub-CPIs for Fourier-based processing. The single-channel solution is based on time-domain analysis of the temporal signal, while the multichannel solution is based on frequency-domain analysis of the temporal signal.

The primary contribution of the single-channel algorithm to improved detection of weak targets is the accurate estimation of the linear and nonlinear phase components of the extended dwell signal in multiple stages with small phase-specific dictionaries rather than through an exhaustive search of a filter bank containing all combinations of phase components. Analysis of the dwell times at which the various nonlinear phase components begin to show a strong presence in the target signal forms the basis of the single-channel, multistage algorithm that successively estimates the various signal components.

Performance was evaluated for a dwell time of 500 ms in a clutter-limited environment and for dwells up to four seconds in a noise-limited environment. In comparison, conventional radar processing methods are limited to a coherent integration time of approximately 100 ms for typical radar and target parameters. The multistage algorithm generates a near optimal signal model and contributes additional output SNR up to approximately forty times that of conventional processing methods for a dwell time of four seconds. The single-channel, multistage algorithm can compensate for small phase errors in the signal due to inaccurate platform motion estimation because the algorithm selects dictionary waveforms that provide the best match to the data regardless of whether the data includes phase errors or not. The multistage algorithm relies on the majority of target signal energy to be outside of the clutter region over the dwell time for accurate signal phase components to be estimated from each phase-specific dictionary. This is especially true for the linear phase component, which is determined with the fewest number of samples. The initial radial velocity of the target must correspond to a Doppler frequency that is outside the mainlobe clutter Doppler region for accurate results.

At dwell times greater than 500 ms, the single-channel, multistage algorithm provides output SINR levels that exceed the 12–13 dB necessary for typical target detection. Other radar applications may benefit from the high output SINR provided by the multistage algorithm.

The two primary contributions of the multichannel solution to improving detection of weak targets are: (1) use of linear prediction coefficients for the temporal weights in pre-Doppler STAP to maximize the input SINR to the temporal processing algorithm and (2) a temporal processing algorithm that detects targets with significantly lower single-sample

SNR than traditional methods. The multichannel solution provides essential target AOA information and a more practical clutter mitigation method than the full covariance solution used with the single-channel algorithm. Element-space pre-Doppler STAP with adaptive temporal weighting based on linear prediction coefficients passes significantly more signal energy to the subsequent temporal processing stage than conventional weights based on binomial coefficients. The final temporal processing algorithm divides the signal into 100 ms sub-CPIs that are processed with Fourier transforms. The detection decision is based on the differences between the frequency characteristics of the target-plus-noise signal and the frequency characteristics of the noise-only signal. For low single-sample SNR targets, the dominant frequency component in each sub-CPI can result from a noise spike. In this scenario, the EDTP algorithm fills in the missing target Dopplers to provide information on the initial radial velocity of the target and the change in velocity over the dwell. In contrast to the single-channel solution, this algorithm does not require the majority of target signal energy to be outside of the clutter region for accurate results. Adequate signal energy in several of the sub-CPIs can be used to make an accurate detection decision and to piece together the target characteristics over the dwell. The EDTP algorithm detects targets with very low initial radial velocities that are well within the mainlobe clutter Doppler region. These targets that have a portion of their energy in the mainlobe clutter Doppler region often have radial velocities below the minimum detectable velocity of traditional STAP methods and above the maximum radial velocity for SAR imaging methods to correctly position the target in a ground scene.

A comparison of methods used to process the pre-Doppler temporal output signal shows the EDTP algorithm significantly outperforms Doppler processing in detecting low

velocity, low single-sample SNR targets. For a target with an initial radial velocity of 1.6 m/s, a single-sample SNR of approximately 5 dB is required for Doppler processing with pre-Doppler temporal weights based on binomial coefficients to achieve the same  $P_D$  as the EDTP achieves with pre-Doppler temporal weights based on linear prediction for a single-sample SNR of  $-6$  dB in 500 trials with a  $P_{FA}$  of 0.001. This decrease of 11 dB in required single-sample SNR for equivalent detection almost doubles the detection range, which lowers the risk of electronic attack and enables a stealthier system operation.

The MATLAB run time for the single-channel, multistage algorithm in a clutter-limited environment is approximately 55 seconds for a one-second data collection time on an HP Pavilion dm4 with a 2.4 GHz, Intel Core i5 (2nd Gen) 2430M microprocessor; this solution includes full covariance matrix processing. The MATLAB run time for the multichannel algorithm that includes  $K$ -STAP pre-Doppler with linear prediction weights and temporal processing of the extended dwell time signal in a clutter-limited environment is 0.1 seconds for a one-second dwell using the same microprocessor. The multichannel algorithm includes reduced-dimension covariance processing methods. The longer processing time for the single-channel solution results primarily from several steps in the algorithm that require multiplication by the full covariance matrix.

## 6.2 Future Work

Future work in long dwell processing includes extension of the signal processing concepts to other radar applications, investigation of algorithm performance for the multiple-target scenario, investigation of methods to mitigate range migration, and further characterization of both the single-channel and multichannel algorithms.

Other radar applications may benefit from the single-channel, multistage algorithm and the multichannel, extended-dwell algorithm concepts. The target motion characteristics provided with the multichannel solution may be useful for target tracking purposes. SAR imaging requires a longer data collection time than typical GMTI dwells. The single-channel, multistage algorithm that generates an accurate signal model for dwells up four seconds provides enough processing gain to detect a weak moving target in a SAR image. Application of the algorithm to a particular range of interest may bring into focus a moving target signal whose energy is buried under the noise and the stationary objects in the ground scene. Current techniques for focusing a moving target in a SAR image [11, 12, 60] require higher SNR levels than are required for the single-channel, multistage algorithm.

The work presented in this dissertation assumes a single target in each range bin. Future work might include evaluation of the effectiveness of the single-channel, multistage algorithm for the multiple-target scenario. In the case of two targets with different single-sample SNRs, the multistage algorithm would generate the signal model for the target with higher single-sample SNR first. In this scenario, after all the phase components of the initial signal model are estimated and removed from the data, the signal model for the weaker target would be generated. Similar single-sample SNRs may be required to estimate phase components for two targets in the same range bin so the combination of noise energy and residual errors from estimating the phase components of the slightly stronger signal do not negatively affect the estimation of phase components for the weaker signal. The multichannel, extended-dwell temporal processing algorithm concepts are likely not directly applicable to the multiple-target scenario.



Over an extended dwell, target signal energy can spread into multiple range bins. Future work in extended dwell radar may require the development of techniques to mitigate range migration for low single-sample SNR targets.

Future work related to target detection over an extended dwell time includes evaluation of the single-channel and multichannel algorithms on measured data collected from an airborne platform to further verify performance. In addition, a more complete characterization of the multichannel algorithm for various initial radial velocities and input SNRs may be performed for 1000 or 10,000 trials.

In summary, future work could extend the algorithm concepts presented in this dissertation to other radar applications and to the multiple-target scenario. In addition, a full characterization of the algorithms on measured data and over many more Monte Carlo trials would provide further validation and a more complete understanding of algorithm limitations.

## APPENDIX A

### CALCULATION OF LINEAR PREDICTION WEIGHTS

A sample,  $x_j$ , of the slow-time signal,  $x_k$ , for  $k = 0:K-1$  can be estimated from a linear combination of the other samples:

$$\hat{x}_j = \sum_{k=0, k \neq j}^{K-1} w_k x_k, \quad (\text{A.1})$$

where  $w_k$  are the weights that minimize the mean squared error:

$$E \left[ \left| x_j - \hat{x}_j \right|^2 \right]. \quad (\text{A.2})$$

The partial derivative of the error expression with respect to  $w_k$  is equal to zero for the weights that minimize

$$\left| x_j - \hat{x}_j \right|^2 = (x_j - \hat{x}_j)(x_j - \hat{x}_j)^*. \quad (\text{A.3})$$

Finding  $w_k$  requires solving for the weights such that

$$\frac{\partial}{\partial w_k} [(x_j - \hat{x}_j)(x_j - \hat{x}_j)^*] = 0. \quad (\text{A.4})$$

Simplifying the left side of (A.4) yields:

$$\begin{aligned} \frac{\partial}{\partial w_k} [(x_j - \hat{x}_j)(x_j - \hat{x}_j)^*] &= \frac{\partial}{\partial w_k} [x_j x_j^* - x_j \hat{x}_j^* - \hat{x}_j x_j^* + \hat{x}_j \hat{x}_j^*] \\ &= \frac{\partial}{\partial w_k} [-\hat{x}_j x_j^* + \hat{x}_j \hat{x}_j^*] \end{aligned} \quad (\text{A.5})$$

We set the final expression in (A.5) to zero and solve the following equation:

$$\frac{\partial}{\partial w_k} (\hat{x}_j x_j^*) = \frac{\partial}{\partial w_k} (\hat{x}_j \hat{x}_j^*). \quad (\text{A.6})$$

$x_j^*$  and  $\hat{x}_j^*$  are constants when taking the partial derivative with respect to  $w_k$ , which means

$$x_j^* \frac{\partial}{\partial w_k}(\hat{x}_j) = \hat{x}_j^* \frac{\partial}{\partial w_k}(\hat{x}_j) . \quad (\text{A.7})$$

Substituting (A.1) into (A.7) we get

$$x_j^* \frac{\partial}{\partial w_k} \left( \sum_{k=0, k \neq j}^{K-1} w_k x_k \right) = \hat{x}_j^* \frac{\partial}{\partial w_k} \left( \sum_{k=0, k \neq j}^{K-1} w_k x_k \right) . \quad (\text{A.8})$$

We can write the summations in (A.8) as inner products:

$$\begin{aligned} & x_j^* \frac{\partial}{\partial w_k} \{ [w_0 \ w_1 \dots w_{j-1} \ w_{j+1} \dots w_{K-1}] [x_0 \ x_1 \dots x_{j-1} \ x_{j+1} \dots x_{K-1}]' \} \\ &= \hat{x}_j^* \frac{\partial}{\partial w_k} \{ [w_0 \ w_1 \dots w_{j-1} \ w_{j+1} \dots w_{K-1}] [x_0 \ x_1 \dots x_{j-1} \ x_{j+1} \dots x_{K-1}]' \} . \end{aligned} \quad (\text{A.9})$$

Solving (A.9) gives:

$$x_j^* [x_0 \ x_1 \dots x_{j-1} \ x_{j+1} \dots x_{K-1}]' = \hat{x}_j^* [x_0 \ x_1 \dots x_{j-1} \ x_{j+1} \dots x_{K-1}]' . \quad (\text{A.10})$$

Rewriting the conjugate version of (A.1),  $\hat{x}_j^* = \sum_{k=0, k \neq j}^{K-1} w_k^* x_k^*$ , as an inner product,

$$\hat{x}_j^* = [w_0^* \ w_1^* \dots w_{j-1}^* \ w_{j+1}^* \dots w_{K-1}^*] [x_0^* \ x_1^* \dots x_{j-1}^* \ x_{j+1}^* \dots x_{K-1}^*]' , \quad (\text{A.11})$$

and reordering terms, (A.10) becomes:

$$\begin{aligned} & x_j^* [x_0 \ x_1 \dots x_{j-1} \ x_{j+1} \dots x_{K-1}]' \\ &= [x_0 \ x_1 \dots x_{j-1} \ x_{j+1} \dots x_{K-1}]' [x_0^* \ x_1^* \dots x_{j-1}^* \ x_{j+1}^* \dots x_{K-1}^*] [w_0^* \ w_1^* \dots w_{j-1}^* \ w_{j+1}^* \dots w_{K-1}^*]' . \end{aligned} \quad (\text{A.12})$$

Defining  $\mathbf{w}_k = [w_0 \ w_1 \dots w_{j-1} \ w_{j+1} \dots w_{K-1}]'$ ,  $\mathbf{s}_j = [x_j^* x_0 \ x_j^* x_1 \ \dots \ x_j^* x_{j-1} \ x_j^* x_{j+1} \ \dots \ x_j^* x_{K-1}]'$ , and

$\mathbf{R}_r$ , the reduced covariance matrix, as

$$\mathbf{R}_r = \begin{bmatrix} x_0 \\ x_1 \\ \vdots \\ x_{j-1} \\ x_{j+1} \\ \vdots \\ x_{K-1} \end{bmatrix} \begin{bmatrix} x_0^* & x_1^* & \dots & x_{j-1}^* & x_{j+1}^* & \dots & x_{K-1}^* \end{bmatrix}, \quad (\text{A.13})$$

the optimum linear prediction weights,  $\mathbf{w}_k = [w_0 \ w_1 \ \dots \ w_{j-1} \ w_{j+1} \ \dots \ w_{K-1}]'$ , are

$$\mathbf{w}_k = (\mathbf{R}_r^{-1} \mathbf{s}_j)^*. \quad (\text{A.14})$$

For the specific linear prediction weights in this application, we estimate  $x_0$  with the combination of three other samples. The estimate of  $x_0$  is subtracted from  $x_0$  to cancel the low-Doppler signal. The pre-Doppler temporal weighting with linear prediction weights:

$$\mathbf{w}_{lp} = [1 \quad -w_1 \quad -w_2 \quad -w_3]', \quad (\text{A.15})$$

weights the sample  $x_0$  with a one and subtracts the estimated value  $\hat{x}_0$  from  $x_0$ .

## REFERENCES

- [1] Entzminger, J. N., Fowler, C. A., and Kenneally, W. J., “JointSTARS and GMTI: past, present, and future,” *IEEE Trans. on Aerosp. and Electron. Syst.*, vol. 35, no. 2, pp. 748–761, April 1999.
- [2] Hersey, R. K., Melvin, W. L., and Culpepper, E., “Dismount modeling and detection from small aperture moving radar platforms,” *Proc. of the 2008 IEEE Radar Conf.*, Rome, Italy, 2008, pp. 1–6.
- [3] Melvin, W. L., “A STAP overview,” *IEEE Aerosp. Electron. Syst. Mag., Special Tutorials Issue*, vol. 19, pp. 19–35, Jan. 2004.
- [4] Ward, J., “Space-Time Adaptive Processing for Airborne Radar,” *Lincoln Laboratory Tech. Rept. ESC-TR-94-109*, Dec. 1994.
- [5] Klemm, R., “Introduction to space-time adaptive processing,” *Electronics and Communication Engineering Journal*, vol. 11, issue 1, 1999, pp. 5–12.
- [6] Guerci, J. R., “Space-Time Adaptive Processing,” in Space-Time Adaptive Processing for Radar, Boston: Artech House, 2003, ch. 3, pp. 51–74.
- [7] Farina, A. and Lombardo, P., “Space-Time Techniques for SAR,” in Applications of Space-Time Adaptive Processing, London, UK: IET, 2004, ch. 3, pp. 73–122.
- [8] Barbarossa, S. and Farina, A., “Detection and Imaging of Moving Objects with Synthetic Aperture Radar, Part 2: Joint Time-Frequency Analysis by Wigner-Ville Distribution,” *IEE Proc. F, Radar and Signal Proc.*, vol. 139, No. 1, pp. 89–97, Feb. 1992.
- [9] Zhou, F., Wu, R., Xing, M., and Bao, Z., “Approach for Single Channel SAR Ground Moving Target Imaging and Motion Parameter Estimation,” *IET Radar Sonar Navig.*, vol. 1, pp. 59–66, Feb. 2007.
- [10] Xia, X., “Discrete Chirp-Fourier Transform and Its Application to Chirp Rate Estimation,” *IEEE Trans. on Sig. Proc.*, vol. 48, no. 11, pp. 3122–3133, Nov. 2000.

- [11] Fienup, J. R., "Detecting moving objects in SAR imagery by focusing," *IEEE Trans. on Aerosp. and Electron. Syst.*, Vol. 37, No. 3, July 2001, pp. 794–809.
- [12] Perry, R. P., Dipietro, R. C., and Fante, R., "SAR Imaging of Moving Targets," *IEEE Trans. on Aerosp. and Electron. Syst.*, Jan. 1999, Vol. 35, No. 1, pp. 188–200.
- [13] Rioul, O. and Flandrin, P., "Time-scale energy distributions: a general class extending wavelet transform," *IEEE Trans. on Sig. Proc.*, Vol. 40, No. 7, July 1992, pp. 1746–1757.
- [14] Chen, V. C. and Qian, S., "Joint time-frequency transform for radar range-Doppler imaging," *IEEE Trans. on Aerosp. and Electron. Syst.*, Apr. 1998, Vol. 34, No. 2, pp. 486–499.
- [15] Almeida, L. B., "The fractional Fourier transform and time-frequency representations," *IEEE Trans. on Sig. Proc.*, Vol. 42, No. 11, Nov. 1994, pp. 3084–3091.
- [16] Djuric, P. M. and Kay, S. M., "Parameter estimation of chirp signals," *IEEE Trans. on Acoust., Speech, and Sig. Proc.*, Vol. 38, No. 12, Dec. 1990, pp. 2118–2126.
- [17] Bergin, J. S., Teixeira, C. M., and Techau, P. M., "Multi-resolution signal processing techniques for airborne radar," *Proc. of the 2004 IEEE Radar Conf.*, Philadelphia, PA, Apr. 2004, pp. 277–282.
- [18] Bergin, J. S. and Techau, P. M., "Multiresolution signal processing techniques for ground moving target detection using airborne radar," *EURASIP Journal on Applied Sig. Proc.* 2006, pp. 1–16.
- [19] Jao, J. K. et al., "Unified Synthetic Aperture Space Time Adaptive Radar (USASTAR) Concept," *Lincoln Lab. Project Rept. ESC-TR-2003-085*, May 2004.
- [20] Shrader, W. W., "MTI Radar," in Radar Handbook, New York: McGraw-Hill, 1970, ch. 17.
- [21] Richards, M. A., "Doppler Processing," in Fundamentals of Radar Signal Processing, New York: McGraw-Hill, 2005, ch. 5, pp. 225–294.

- [22] Richards, M. A., “Introduction to Radar Systems,” in Fundamentals of Radar Signal Processing, New York: McGraw-Hill, 2005, ch. 1, pp. 1–52.
- [23] Doerry, A. W., “Performance Limits for Exo-Clutter Ground Moving Target Indication (GMTI) Radar,” *Sandia National Laboratories Rept. SAND2010-5844*, Sept. 2010.
- [24] Scheer, J. A. and Holm, W. A., “Introduction and Radar Overview,” in Principles of Modern Radar: Basic Principles, Edison, NJ: SciTech, 2010, ch. 1, pp. 3–57.
- [25] Blair, D. W., Richards, M. A., and Long, D. G., “Radar Measurements,” in Principles of Modern Radar: Basic Principles, Edison, NJ: SciTech, 2010, ch. 18, pp. 677–712.
- [26] Richards, M. A., “Introduction to Beamforming and Space-Time Adaptive Processing,” in Fundamentals of Radar Signal Processing, New York: McGraw-Hill, 2005, ch. 9, pp. 461–503.
- [27] Richards, M. A., “Digital Signal Processing Fundamentals for Radar,” in Principles of Modern Radar: Basic Principles, Edison, NJ: SciTech, 2010, ch. 14, pp. 495–546.
- [28] Richards, M. A., “Detection Fundamentals,” in Fundamentals of Radar Signal Processing, New York: McGraw-Hill, 2005, ch. 6, pp. 295–345.
- [29] Scheer, J. A., “Radar Search and Overview of Detection in Interference,” in Principles of Modern Radar: Basic Principles, Edison, NJ: SciTech, 2010, ch. 3, pp. 87–113.
- [30] DiFranco, J. V. and Rubin, W. L., “The A Posteriori Theory of Reception,” in Radar Detection, Raleigh, NC: SciTech, 2004, ch. 7, pp. 202 – 251.
- [31] Haykin, S., “Estimation Theory,” in Adaptive Filter Theory, Upper Saddle River, NJ: Prentice-Hall, 1996, appendix D, pp. 899 – 904.
- [32] Johnson, D. H. and Dudgeon, D. E., “Detection Theory,” in Array Signal Processing, Upper Saddle River, NJ: Prentice-Hall, 1993, ch. 5, pp. 199 – 265.

- [33] DiFranco, J. V. and Rubin, W. L., “Statistical Decision Theory,” in Radar Detection, Raleigh, NC: SciTech, 2004, ch. 8, pp. 252 – 286.
- [34] The Mathworks, Inc., Receiver Operating Characteristic (ROC) Curves, <http://www.mathworks.com/help/phased/ug/receiver-operating-characteristic-roc-curves.html>
- [35] Skolnik, M. I., “An introduction and overview of radar,” in Radar Handbook, 3rd ed., New York: McGraw-Hill, 2008, ch. 1.
- [36] Ross, S. M., “Random Variables”, in Introduction to Probability Models, Burlington, MA: Academic Press, 2007, ch. 2, pp. 23–96.
- [37] Schaeffer, J. F., “Target Reflectivity,” in Principles of Modern Radar: Basic Principles, Edison, NJ: SciTech, 2010, ch. 6, pp. 211–245.
- [38] Blake, L. V., “Prediction of Radar Range,” in Radar Handbook, New York: McGraw-Hill, 1970, ch. 2.
- [39] Melvin, W. L. “Surface Moving Target Indication,” in Principles of Modern Radar: Radar Applications, Edison, NJ: SciTech, 2014, ch. 9, pp. 383 – 429.
- [40] Soliday, S. M., “Lane Position Maintenance by Automobile Drivers on Two Types of Highways,” *Ergonomics*, Vol. 18, No. 2, 1975, pp. 175 – 183.
- [41] Paulus, A. S., Melvin, W. L., and Williams, D. B., “Multistage Algorithms for Single-Channel Extended Dwell Target Detection,” *Proc. of the 2014 IEEE Radar Conference*, Cincinnati, May 2014, pp. 1–5.
- [42] Long, G., “Acceleration Characteristics of Starting Vehicles,” *Transportation Research Board 79<sup>th</sup> Annual Meeting*, Washington, DC, January 9 – 13, 2000.
- [43] Federation of American Scientists (FAS), Military Analysis Network, High Mobility Multipurpose Wheeled Vehicle (HMMWV), <http://www.fas.org/man/dod-101/sys/land/m998.htm>
- [44] Richards, M. A., “Radar Waveforms,” in Fundamentals of Radar Signal Processing, New York: McGraw-Hill, 2005, ch. 4, pp. 159–224.



- [45] Bailey, C. D., “Radar Antennas,” in Principles of Modern Radar: Basic Principles, Edison, NJ: SciTech, 2010, ch. 9, pp. 309 – 346.
- [46] Johnson, D. H. and Dudgeon, D. E., “Matrix Theory,” in Array Signal Processing, Upper Saddle River, NJ: Prentice-Hall, 1993, appendix B, pp. 485–498.
- [47] Paulus, A. S., Melvin, W. L., and Williams, D. B., “Performance Bounds for Long-Dwell, Multichannel Radar,” *Proc. of the 2013 IEEE Radar Conference*, Ottawa, May 2013, pp. 1–5.
- [48] Melvin, W. L. “Clutter Suppression Using Space-Time Adaptive Processing,” in Principles of Modern Radar: Advanced Techniques, Edison, NJ: SciTech, 2013, ch. 10, pp. 453 – 497.
- [49] Barton, D. K., “Land clutter models for radar design and analysis,” *Proc. of the IEEE*, vol. 73, no. 2, Feb. 1985, pp. 198-204.
- [50] Currie, N. C., “Characteristics of Clutter,” in Principles of Modern Radar: Basic Principles, Raleigh, NC: SciTech Publishing, 2010, ch. 5, pp. 165–210.
- [51] Richards, M. A., “Sampling and quantization of pulsed radar signals,” in Fundamentals of Radar Signal Processing, New York: McGraw-Hill, 2005, ch. 3, pp. 115–157.
- [52] DiPietro, R. C., “Extended factored space-time processing for airborne radar,” *Proc. of the 32nd Asilomar Conference*, Pacific Grove, CA, Oct. 1992, pp. 425–430.
- [53] Wang, H. and Cai, L., “On adaptive spatial-temporal processing for airborne surveillance radar systems,” *IEEE Trans. on Aerosp. and Electron. Syst.*, vol. 30, no. 3, pp. 660–670, July 1994.
- [54] Blum, R., Melvin, W., and Wicks, M., “An analysis of adaptive DPCA,” *Proc. of the 1996 IEEE Radar Conference*, Ann Arbor, MI, May 1996, pp. 303–308.
- [55] Battisti, N., “Reduced dimension principal components for STAP,” *Proc. of the 2013 IEEE Radar Conference*, Ottawa, 2013, pp. 1–5.

- [56] Haykin, S., "Linear prediction," in Adaptive Filter Theory, Upper Saddle River, NJ: Prentice-Hall, 1996, ch. 6, pp. 241–301.
- [57] Johnson, D. H. and Dudgeon, D. E., "Estimation theory," in Array Signal Processing, Englewood Cliffs, NJ: Prentice-Hall, 1993, ch. 6, pp. 266–348.
- [58] Farina, A. and Protopapa, A., "New Results on Linear Prediction for Clutter Cancellation," *IEEE Trans. on Aerosp. and Electron. Syst.*, vol. 24, no. 3, pp. 275–286, May 1988.
- [59] Scheer, J. A., "The Radar Range Equation," in Principles of Modern Radar: Basic Principles, Edison, NJ: SciTech, 2010, ch. 2, pp. 59 – 86.
- [60] Carrera, W. G., Goodman, R. S., and Majewski, R. M., "Autofocus Techniques," in Spotlight Synthetic Aperture Radar, Boston: Artech House, 1995, ch. 6. pp. 245–287.

## **VITA**

### **AUDREY SANDRA VAN BLOMMESTEYN PAULUS**

Audrey van Blommesteyn Paulus was born in Glen Cove, New York, on January 4, 1966. She received a B.S. in Electrical Engineering from Auburn University, Auburn, Alabama, in 1989 and worked for Hewlett Packard in Colorado Springs, Colorado from 1989–1991. Ms. Paulus attended the Georgia Institute of Technology, Atlanta, Georgia, as a Presidential Fellow from 1991–1993 and received an M.S. in Electrical Engineering from Tech in 1993. After taking time off from school to raise a family, Ms. Paulus returned to Georgia Tech in 2010 to pursue a doctorate in Electrical Engineering with a focus in Digital Signal Processing and a minor in Mathematics. Since 2011, she has been a Graduate Research Assistant at the Georgia Tech Research Institute (GTRI) Sensing and Electromagnetics Laboratory (SEAL).

When she is not working on her research, Ms. Paulus enjoys reading nonfiction books and spending time with her husband, Rick, and her five children, Caroline, Rebecca, John, Anna, and David.